

2018-05-22

Evaluation of Measurement Techniques for the Adsorption of Asphaltenes onto Metal Oxide Nanoparticles

Ezeonyeka, Nkiru Lucia

Ezeonyeka, N. L. (2018). Evaluation of Measurement Techniques for the Adsorption of Asphaltenes onto Metal Oxide Nanoparticles (Master's thesis, University of Calgary, Calgary, Canada). Retrieved from <https://prism.ucalgary.ca>. doi:10.11575/PRISM/31961
<http://hdl.handle.net/1880/106716>

Downloaded from PRISM Repository, University of Calgary

UNIVERSITY OF CALGARY

Evaluation of Measurement Techniques for the Adsorption of Asphaltenes onto Metal Oxide
Nanoparticles

by

Nkiru Lucia Ezeonyeka

A THESIS

SUBMITTED TO THE FACULTY OF GRADUATE STUDIES
IN PARTIAL FULFILMENT OF THE REQUIREMENTS FOR THE
DEGREE OF MASTER OF SCIENCE

GRADUATE PROGRAM IN CHEMICAL ENGINEERING

CALGARY, ALBERTA

May, 2018

© Nkiru Ezeonyeka 2018

Abstract

The adsorption of asphaltenes onto nanoparticles (NPs) has received a lot of attention in the recent years owing to its important application in areas such as heavy oil recovery. The effect of the measurement technique on the adsorption isotherms has never been addressed, however. In this work, the adsorption of *n*-heptane-precipitated asphaltenes, C7-asphaltenes, from toluene model solutions onto three metal oxide NPs; namely Fe₂O₃, Fe₃O₄, and Al₂O₃, was studied. Most results on asphaltenes adsorption employed UV-Vis spectroscopy, especially when using conventional adsorbents. More recently, and with advent of NPs, thermogravimetric analysis (TGA) has also been used. In this investigation, asphaltenes uptake calculated from UV-Vis spectroscopy at three different wavelengths were compared with thermogravimetric analysis (TGA) results. Although the adsorption trends followed Langmuir isotherms, instrument as well as wavelength-dependent adsorption coefficients were obtained. TGA results are believed to be more reliable, provided complete oxidation and account of mass loss due to NPs is attained. UV-Vis measurements, on the other hand, may be impacted by the chemical structure of the asphaltenes sub fractions as well as their state of association. Al₂O₃ showed the highest adsorption capacity of 385 ± 5 mg/g, followed by Fe₃O₄ and Fe₂O₃. However, based on mg/m², Fe₂O₃ displayed the highest adsorption capacity. TGA analysis revealed that the NPs promoted the oxidation of adsorbed asphaltenes in a reverse order to their adsorption capacity, q_{max} (mg/g) (Al₂O₃ > Fe₂O₃ \approx Fe₃O₄). This trend is in line with a previous observation of mass-dependent thermo-oxidative profile and surface exposure role, rather than a catalyst role, of the NPs.

Acknowledgements

I am thankful to God for everything. I would like to express my deepest gratitude to my supervisor, Dr Maen Husein, without whom this research work would not have been possible. I am eternally grateful for his insight, unending encouragement, patience and support. I am also grateful to my committee members, Dr. Josephine Hill and Dr. Harvey Yarranton.

I want to thank Abdolhossein Hemmati-Sarapardeh for all his support and advice. My gratitude also goes to Afrooz Eshraghian for always been there for me, and all my colleagues and friends in the Nano-Technology for Energy and Environment (NTEE) research group. Thanks also to Gerardo Vitale Rojas and Ola Jabar for their help with the XRD and TEM experiments and Arsalan Fardi for his help in the early days of my research. I wish to thank all the staff of Chemical Engineering department for their support.

Special thanks to my entire family for their patience and all the sacrifices they had to make the entire duration of my studies.

Dedication

To my family

Table of Contents

Chapter 1: Introduction.....	1
1.1 Background	1
1.2 Research Objectives.....	6
1.3 Thesis Structure	7
Chapter 2: Literature Review	9
2.1 Crude Oil and Its Fractions	9
2.2 SARA Fraction.....	10
2.3 Properties of Asphaltenes.....	11
2.3.1 Asphaltene Composition	11
2.3.2 Asphaltenes Molecular Weight	12
2.3.3 Asphaltene structure	13
2.3.4 Asphaltene Self-Association.....	14
2.4 Asphaltene - Surface Interaction.....	15
2.4.1 Adsorption on Mineral Surface.....	16
2.4.2 Adsorption on Metal Surface	17
2.4.3 Adsorption onto NPs	18
2.5 Adsorption Isotherm.....	19
2.6 The use of UV-Vis for Adsorption Studies	20
2.7 Characterization Techniques.....	23
2.7.1 Thermogravimetric analysis (TGA) technique.....	23
2.7.2 FTIR.....	24
2.7.3 Dynamic light scattering	25

2.7.4 XRD	26
2.7.5 Transmission electron microscopy	27
Chapter 3: Experiment Methods.....	29
3.1 Materials and Methods.....	29
3.1.1 Materials.....	29
3.1.2 Methods	29
3.1.2.1 Characterization of the extracted C7-asphaltenes.....	29
3.1.2.2 Characterization of the NPs and the adsorbed asphaltenes.....	30
3.1.2.3 Preparation of the heavy oil model solutions.....	30
3.1.2.4 Adsorption experiments	31
Chapter 4: Results and Discussion.....	35
4.1 Asphaltenes Characterization.....	35
4.2 Characterization of Asphaltenes in Model Solution.....	44
4.3 NP characterization	45
4.4 Adsorption Isotherms	48
4.4.1 Characterization of the adsorbed asphaltenes.....	57
4.4.2 Oxidation of adsorbed asphaltenes	59
Chapter 5: Conclusions, Contributions and Recommendations.....	63
5.1 Conclusions.....	63
5.2 Contributions.....	64
5.3 Recommendations for Future Work	64
Appendix A: Supplementary Material (Elsevier License)	90

List of Tables

Table 2.1: Elemental composition of various asphaltenes (Teh Fu Yen & Chilingarian, 1994).	12
Table 3.1: Slopes and coefficient of determination for the different UV-Vis calibration curve ..	32
Table 4.1: Aromaticity and crystalline parameters of C ₇ -asphaltene nanoclusters extracted in this work based on XRD fingerprint in comparison with the literature	40
Table 4.2: FTIR band assignment of virgin C ₇ -asphaltene extracted in this study	43
Table 4.3: TriStar pore volume and surface area estimates and average NP size obtained from XRD and TEM and the corresponding surface area.	46
Table 4.4: Langmuir and Freundlich parameters and the corresponding R^2 values obtained by fitting the models to UV-Vis and TGA-calculated uptake.	48
Table 4.5: Langmuir parameters and the corresponding R^2 values obtained by fitting the models to UV-Vis and STA results, with q_e in mg/m ² and mg/g for the low concentrations < 1,000 ppm.....	57

List of Figures and Illustrations

Figure 1.1: A chart that shows worldwide distribution of heavy oil resources (Riazi, 2013).	1
Figure 1.2: Rising production of heavy oil (Riazi, 2013)	2
Figure 2.1: Boiling point ranges of crude oil fractions	9
Figure 2.2: Schematic representation of SARA classification of crude oil	10
Figure 2.3: Asphaltene molecules structural representation for (a) Archipelago type-model (b) Continental type-model	13
Figure 2.5: Schematic of a double beam UV-Visible Spectrophotometer	22
Figure 2.4: Possible electron transitions	22
Figure 2.6: DRIFTS analyzer	25
Figure 2.7: A basic schematic representation of a light scattering measurement	25
Figure 2.8: Representation of the XRD process (Bhattacharya et al., 2008)	27
Figure 2.9: Schematic Diagram showing TEM	28
Figure 3.1: Calibration curves for asphaltenes in toluene. The error bars are too small to be seen	32
Figure 3.2: Asphaltenes uptake, q , for different concentrations of asphaltenes solution versus time at (a) 410 nm (b) 550 nm (c) 700 nm.	33
Figure 4.1: XRD pattern for virgin C7-asphaltenes extracted in this study	35
Figure 4.2: A schematic representation of a cross section of asphaltenes nanoclusters.	42
Figure 4.3: FTIR spectrum of virgin C7-asphaltenes extracted in this study.	43
Figure 4.4: DLS mean diameter of asphaltenes nanoaggregates in the toluene model solutions as a function of concentration.	44
Figure 4.5: Refractive index measure of asphaltenes nanoaggregates in the toluene model solution	45
Figure 4.6: XRD and TEM images of the as received (a) Al_2O_3 (b) Fe_2O_3 (c) Fe_3O_4 following washing with toluene.	47

- Figure 4.7: Adsorption isotherms of asphaltenes onto (a) Al_2O_3 (b) Fe_2O_3 (c) Fe_3O_4 . Points: experimental; Lines: Langmuir model fitted to UV-Vis measurements at 3 different wavelengths and TGA results. 50
- Figure 4.8: Adsorption isotherm of asphaltenes onto (a) Al_2O_3 (b) Fe_2O_3 (c) Fe_3O_4 showing the Freundlich model with q_e in mg/m^2 . The symbols are UV-Vis experimental data and TGA result in mg/m^2 51
- Figure 4.9: Adsorption isotherm of asphaltenes onto (a) Al_2O_3 (b) Fe_2O_3 (c) Fe_3O_4 showing the Langmuir model (E2.1), with q_e in mg/g . The symbols are UV-Vis experimental data and TGA result in mg/g ., the solid lines are the best fit of the Langmuir model. 52
- Figure 4.10: Adsorption isotherm of asphaltenes onto (a) Al_2O_3 (b) Fe_2O_3 (c) Fe_3O_4 showing the Freundlich model (E2.2), with q_e in mg/g . The symbols are UV-Vis experimental data and TGA result in mg/g 53
- Figure 4.11: Adsorption isotherm of asphaltenes onto (a) Al_2O_3 (b) Fe_2O_3 (c) Fe_3O_4 showing the Langmuir model (E2.1), with q_e in mg/m^2 for the low concentrations $< 1,000$ ppm. 55
- Figure 4.12: Adsorption isotherm of asphaltenes onto (a) Al_2O_3 (b) Fe_2O_3 (c) Fe_3O_4 showing the Langmuir model (E2.1), with q_e in mg/g for the low concentrations $< 1,000$ ppm. 56
- Figure 4.13: FTIR spectra of virgin and adsorbed asphaltenes onto (a) Al_2O_3 ; (b) Fe_2O_3 ; (c) Fe_3O_4 NPs. FTIR spectra for the NPs are provided for comparison. 58
- Figure 4.14: Fractional conversion, α , versus temperature for adsorbed asphaltenes onto (a) Al_2O_3 ; (b) Fe_2O_3 ; (c) Fe_3O_4 NPs 60
- Figure 4.15: % Mass loss vs. temperature curves of asphaltene solutions onto (a) Al_2O_3 (b) Fe_2O_3 (c) Fe_3O_4 62

List of Symbols, Abbreviations and Nomenclature

Symbol	Definition
CNAC	Critical nanoaggregate concentration
$^{\circ}\text{C} / \text{min}$	Degree Celsius per minute
DRIFTS	Diffuse Reflectance
DLS	Dynamic light scattering
EoS	Equation of State
C_e	Equilibrium concentration in mg/m^2
FTIR	Fourier Transform infrared spectroscopy
C_o	Initial concentration in mg/m^2
kV	Kilovolt
ma	Milliampere
mg/m^2	Milligrams per meter squared
min	Minute
nm	Nanometer
NP	Nanoparticle
NMR	Nuclear magnetic resonance
ppm	Parts per million
QCM-D	Quartz crystal microbalance with dissipation monitoring
RI	Refractive Index
SANS	Small-angle neutron scattering

SAXS	Small-angle x-ray scattering
TGA	Thermogravimetric analysis
TRFD	Time resolved fluorescence detection
TEM	Transmission Electron Microscopy
UV-Vis	Ultraviolet-visible
XRD	X-ray diffraction

Chapter 1: Introduction

1.1 Background

Some regions around the world are experiencing high population growth coupled with increased economic development. These two factors, in turn, lead to an increased demand for affordable fuel to power the economy and provide the necessary accommodation and transportation for the growing population. Despite concerns that the world's hydrocarbon reserves are depleting, its continued exploitation is necessary for the economic sustenance of the nations. Heavy oils and bitumen constitute a larger portion of the remaining hydrocarbon resources compared to their lighter, conventional and more easy produced counterpart (Mullins, 2007). Figure 1.1 shows the worldwide distribution of the heavy oil resources.

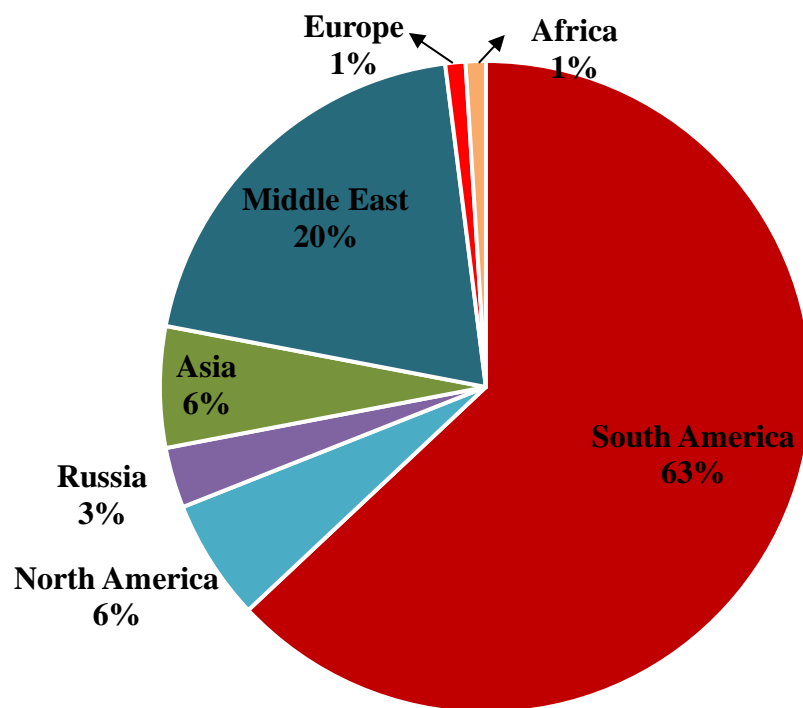


Figure 1.1: A chart that shows worldwide distribution of heavy oil resources (Riazi, 2013).

Diversifying of the world's energy supply source to include renewable energy sources and unconventional oil and gas (despite the technological and environmental challenges involved), is necessary, in order to meet the increasing energy demand (Canadian Association of Petroleum

Producers, 2018). Hence, there is a need for the petroleum industry to produce and refine heavy crude oils (Wilt, Welch, & Rankin, 1998a), as shown in Figure 1.2. Heavy oil has a high proportion of high molecular weight components, is rich in asphaltene, and has high viscosity (Meyer, 2003). An overview of crude oil focused on the asphaltenes fraction is given below.

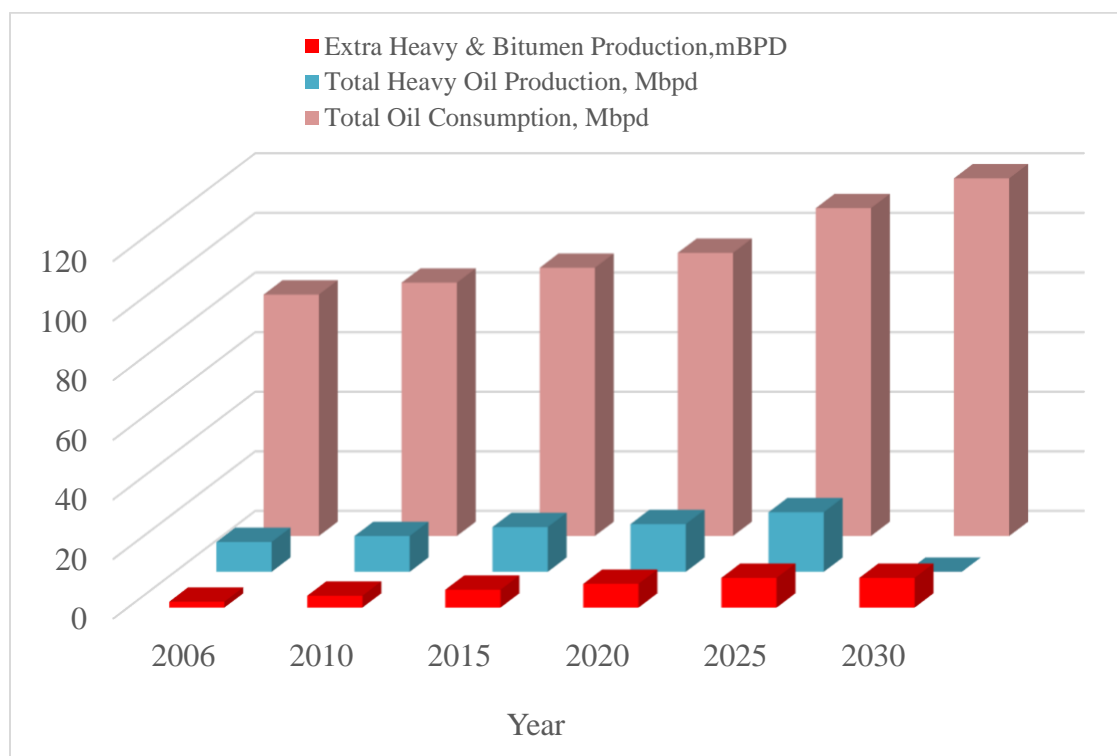


Figure 1.2: Rising production of heavy oil (Riazi, 2013)

Crude oil is a liquid with a complex composition of different molecules and colloidal aggregates of different sizes dispersed in a mixture of other hydrocarbons (Carnahan, 2000; Douda, Llanos, Alvarez, & Bolaños, 2004; Murgich, Rodríguez, & Aray, 1996). Asphaltenes are the heaviest and most polar constituent of crude oil (Speight, 2004a; Young & Stacey, 1978). Their presence has been shown experimentally to be one of the major reasons behind the undesirable high viscosity of heavy oil (Luo & Gu, 2007). In addition, changes in temperature, pressure and/or composition during production significantly affect the stability of the crude oil colloidal system, leading to asphaltenes precipitation and subsequent major production problems (Kamari, Safiri, & Mohammadi, 2015; Olga León et al., 2002; Mohammadi & Richon, 2007). A practical definition

of asphaltenes is based on solubility class. They are the fraction of crude oil that is insoluble in straight-chain paraffins such as pentane and heptane, but soluble in aromatics such as toluene (Yarranton, Hussein Alboudwarej, Jakher, Yarranton, & Alboudwarej, 2000; Hemmati-Sarapardeh et al., 2013; Rudyk & Spirov, 2014). In fact, asphaltenes are a family of compounds with very complex poly-aromatic structure that contains functional groups such as amines, ketones, esters carboxylic acids, etc., with some heteroatoms such as nitrogen, oxygen, sulphur and metals (Al Jabari, Nassar, & Husien, 2007; Nalwaya, Tantayakom, Piumsomboon, & Fogler, 1999).

Different studies using techniques such as plasma desorption mass spectroscopy (Larsen & Li, 1995) and vapor pressure osmometry (Andersen, Keul, & Stenby, 1997; Boduszynski, 1988; Yarranton et al., 2000; Yarranton & Masliyah, 1996) suggested a molecular weight range for asphaltenes of 500 to 3,000 Da with an average monomer value of 750 Da (Spiecker, Gawrys, Trail & Kilpatrick, 2003). The two most widely accepted structural models for asphaltene monomer are the island or continental model and the archipelago model (Borton, Pinkston, Hurt, Tan, & Azyat, 2010). In the island, or Yen-Mullins model, the asphaltene molecules contain a single poly-aromatic hydrocarbon (PAH) core with pendant aliphatic chains, whereas the archipelago model consists of several smaller poly-aromatic moieties that are interconnected via aliphatic chains (Dutta Majumdar, Gerken, Mikula, & Hazendonk, 2013; Sabbah, Morrow, Pomerantz, & Zare, 2011). The PAH is polarizable, thus making it a favorite site for intermolecular attraction, while the surrounding aliphatic chains provide steric hindrance preventing close proximity of the PAH cores (Mullins, 2010).

The self-association property of asphaltenes even at low concentrations, impacts the structure and size distribution of asphaltene nanoaggregates. Conventionally, asphaltene nanoaggregate is seen as a colloid, which is a stack of continent-like asphaltene monomers held together by π - π bonds. Alternatively, the nanoaggregates can be viewed as an oligomer or supramolecule and can be compared to a polymer held by intermolecular forces such as hydrogen bonding acid-base interactions, π - π bonding, instead of covalent bonds. This oligomer model agrees with the archipelago structure (Yarranton et al., 2013). In order to accurately predict asphaltene

precipitation conditions, and develop effective control strategies, it is important to understand the relationship between the mechanism of asphaltene precipitation and its self-association. The first precipitation mechanism generally views asphaltenes as a colloidal dispersion with resins as stabilizing agents and its precipitation is due to the aggregation of the colloid. Another mechanism describes asphaltenes as been in solution with the oil, and its precipitation is solid or liquid phase separation (Yarranton et al., 2013; Gray, Tykwinski, Stryker, & Tan, 2011). The colloidal mechanism is more suitable for the description and analysis of the interactions between asphaltene aggregates and surfaces (Gray et al., 2011).

There is a fine balance of attractive and repulsive forces between asphaltenes molecules which gives them their unique property of being soluble in toluene and insoluble in *n*-heptane (Hortal, Hurtado, Martnez-haya, Mullins, & Marti, 2007; Mullins, 2010). However, going by the colloidal model, the addition of *n*-alkane to asphaltene has the following effects on the mixture. A change in the net interactive forces between the aggregates from repulsive to attractive, a change in the solvation strength of the hydrocarbon part which leads to changes in the population of aggregates, and subsequent precipitation of the low solubility species such as vanadyl porphyrins. Aggregates that pre-existed in the solution probably act as nucleation sites for this precipitation (Gray et al., 2011).

Asphaltenes adsorb onto surfaces by virtue of their surface activity (Nassar, Hassan, & Pereira-Almao, 2011b). For example, the presence of carboxylic and phenolic weak acid groups in asphaltene give them the ability to adsorb on surfaces as individual molecules or as nanoaggregates of varying sizes (Nassar, 2010). Accordingly, asphaltenes can be removed via adsorption onto desired adsorbents (Abu Tarboush & Husein, 2012a). Many researchers have successfully used metallic oxides such as oxides of iron, aluminum, nickel (Abu Tarboush & Husein, 2012a, 2015; Nassar, Hassan, & Pereira-almao, 2011), clays, silica (Bantignies, Cartier Dit Moulin, & Dexpert, 1998; Timea Pernyeszi & Dékány, 2001) as adsorbents for asphaltenes removal. Metallic oxide NPs favorably adsorb asphaltenes by virtue of their huge surface area and active sites that could also be useful in the selective upgrading of the adsorbed asphaltenes (Giraldo, Erto, & Moreno-Piraján, 2013). For example, Shayan and Mirzayi (Shayan & Mirzayi, 2015b) studied the use of

in-house synthesized maghemite ($\gamma\text{-Fe}_2\text{O}_3$) and hematite ($\alpha\text{-Fe}_2\text{O}_3$) NPs for the adsorption and removal of asphaltenes from toluene model solutions. They suggested that the higher adsorption capacity/g of $\gamma\text{-Fe}_2\text{O}_3$ resulted from smaller size, acidity and the orientation of the functional groups in the asphaltenes (Shayan & Mirzayi, 2015b). Husein and coworkers reported very high asphaltene uptake from heavy oil by *in situ* prepared NiO (Abu Tarboush & Husein, 2012a), Fe_2O_3 (Abu Tarboush & Husein, 2015) and Al_2O_3 (Husein & Alkhaldi, 2014) and attributed the high uptake to the intimate dispersion of the *in situ* NPs compared with the commercial ones.

Various studies on the adsorption of asphaltenes onto different solid surfaces reported Langmuir type adsorption isotherm (Abu Tarboush & Husein, 2012a), which suggests monolayer adsorption of asphaltenes molecules or nanoaggregates (Hosseinpour, Khodadadi, Bahramian, & Mortazavi, 2013). Other studies, nevertheless, reported adsorption of multilayers and aggregates (Castro, de la Cruz, Buenrostro-Gonzalez, López-Ramírez, & Gil-Villegas, 2009; Maher et al., 2007). NP adsorption of asphaltenes also has the advantage of preventing damage in oil wells as a result of their smaller sizes and rapid transport in porous media (Adams, 2014). Most asphaltene adsorption studies have been performed using initial asphaltene concentrations of $\leq 4,000$ ppm, which corresponded to equilibrium concentration $\leq 1,000$. Moreover, most of the asphaltenes uptake values reported in literature were based on UV-Vis spectroscopy, often obtained at the prominent absorbance sorbet peak of 410 nm, which corresponds to the presence of metal porphyrins in the asphaltenes (Banda-Cruz et al., 2017; Evdokimov, Fesan, & Losev, 2017; Semple et al., 1990). Other investigations used different wavelengths such as 370, 400, 500, 524, 600 (Sócrates Acevedo, Ranaudo, Escobar, Gutiérrez, & Ortega, 1995; Akhlaq, Götze, Kessel, & Dornow, 1997; Gaboriau & Saada, 2001; Marlow, Sresty, Hughes, & Mahajan, 1987; Timea Pernyeszi & Dékány, 2001; Tímea Pernyeszi, Patzkó, Berkesi, & Dékány, 1998), without adequate justification. Different wavelengths, on the other hand, may be sensitive to different asphaltenes sub fractions (Evdokimov & Losev, 2007). Therefore, it is necessary to explore the role of the complex structure of asphaltenes and their self-association on their adsorption using a wider range of asphaltenes concentration of 200 ppm to 10,000 ppm.

1.2 Research Objectives

This study, in part, is aimed at exploring the role of the complex structure of asphaltenes and their self-association on their adsorption. Hence, a wide range of asphaltenes concentration, 200 ppm to 10,000 ppm, is considered. Most of the literature studies only investigated asphaltene adsorption at initial concentrations $< 4,000$ ppm, which corresponded to equilibrium concentration $< 1,000$ ppm (Hosseinpour et al., 2013; Nassar, 2010; Shayan & Mirzayi, 2015a). Moreover, most of the asphaltenes uptake values reported in the literature were based on UV-Vis spectroscopy, often obtained at the prominent absorbance peak of 410 nm, which corresponds to the presence of metal porphyrins in the asphaltenes (Banda-Cruz et al., 2017; Evdokimov et al., 2017; Semple et al., 1990). Other investigations used different wavelengths such as 370, 400, 500, 524, 600 (Sócrates Acevedo et al., 1995; Akhlaq et al., 1997; Gaboriau & Saada, 2001; Marlow et al., 1987; Timea Pernyeszi & Dékány, 2001; Tímea Pernyeszi et al., 1998), without adequate justification. Different wavelengths, on the other hand, may be sensitive to different asphaltenes sub fractions (Evdokimov & Losev, 2007).

Accordingly, adsorption isotherms at three different UV-Vis wavelengths; namely 410 nm, 550 nm and 700 nm, were compared in this study. In addition, this study compares the UV-Vis isotherms with those obtained from thermogravimetry analysis (TGA). Relatively few literature contributions based uptake on thermogravimetry (TGA) data (Abu Tarboush & Husein, 2015; Nassar, Hassan, & Pereira-Almao, 2011a; Nassar, Hassan, & Pereira-Almao, 2011b), without providing a comparison with the most commonly used UV-Vis spectroscopy technique (Ezeonyeka, Hemmati-Sarapardeh, & Husein, 2018). In addition to providing comparison with UV-Vis spectroscopy, the thermo-oxidative TGA profiles of adsorbed asphaltenes provided further insight on Abu Tarboush and Husein's (Abu Tarboush & Husein, 2012b, 2015) conclusion, which attributed the enhanced oxidation of adsorbed asphaltenes onto NPs to a surface exposure rather than a catalytic effect. Lastly, the structure of the C7-asphaltenes extracted in this work was characterized in detail using elemental analysis, diffuse reflectance Fourier transform infrared spectroscopy (DRIFTS), and XRD.

The objectives of this study were to:

1. Run batch experiments for asphaltenes adsorption onto NPs from model toluene solutions at constant temperature of 25 °C.
2. Collect measurements of asphaltene concentration before and after adsorption to enable calculation of asphaltenes uptake by NPs using UV-Vis spectroscopy at three different wavelengths; viz 410 nm, 550 nm and 700 nm.
3. Calculate uptake by measuring mass of asphaltenes taken up by the NPs from TGA following asphaltenes oxidation. The NPs together with the adsorbed asphaltenes were exposed to high temperatures, up to 1,000°C, under air flow.
4. Use the thermo-oxidative profile of asphaltenes to deduce conclusions on the role of the NPs.
5. Employ different types of metal oxide NPs; viz Al_2O_3 , Fe_2O_3 and Fe_3O_4 in order to provide generality for the results and enable comparison between the different particles.

1.3 Thesis Structure

This thesis is organized in chapters as outlined below:

Chapter 1 is a general introduction, thesis objective and outline.

Chapter 2 is a review of the literature on topics covered in this thesis. The topics include crude oil and its fractions, properties of asphaltenes, asphaltenes-surface interactions, the use of UV-Vis technique for adsorption studies, and overview of the characterization techniques employed in this work.

Chapter 3 presents the experimental methods used to evaluate asphaltenes adsorption and characterize the asphaltenes, the NPs and the adsorbed asphaltenes. Details on control samples, replications, preliminary experiments to determine equilibrium time are given.

Chapter 4 shows the results and discusses the trends obtained. Detailed comparisons with the literature findings are provided. Flaws and lack of justification existing in some literature are

highlighted, especially given the control samples employed in this study and the level of replication used. New hypotheses more suited to explain current and literature results, are also provided.

Chapter 5 lists the conclusions, contributions and recommendations for future work.

Chapter 2: Literature Review

This chapter provides a brief review of heavy crude oil and its classification and of asphaltenes and their chemistry.

2.1 Crude Oil and Its Fractions

Crude oil is a mixture of hydrocarbons and heteroatomic compounds (Simanzhenkov & Idem, 2003). The components have different fractions and can be fractionated by distillation. At atmospheric pressure and boiling point up to 350 °C, the lighter constituents of crude oil separate into the following fractions: gasoline, heavy naphtha, kerosene and diesel. The fraction of crude remaining at this stage is referred to as the atmospheric residue, which typically distils at a boiling point of over 350 °C. The atmospheric residue can be further distilled at a low pressure (vacuum) to give vacuum gas oil and vacuum residue (Simanzhenkov & Idem, 2003). The widely accepted boiling point ranges of the different fractions are given in Figure 2.1 below (Simanzhenkov & Idem, 2003).

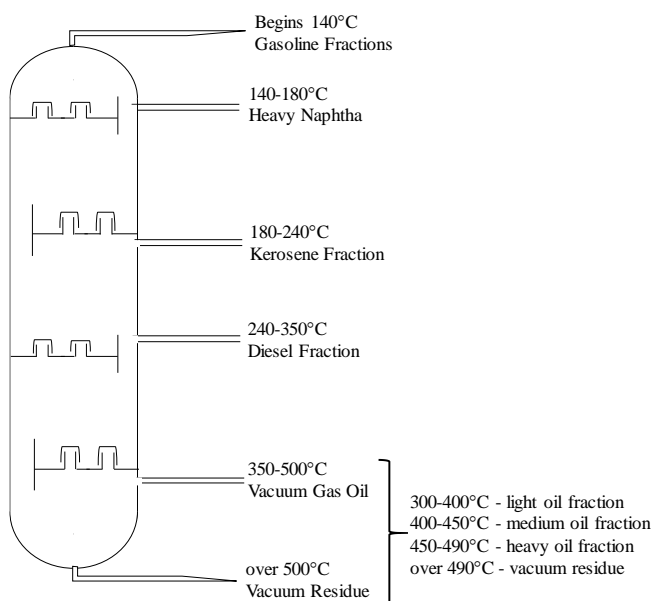


Figure 2.1: Boiling point ranges of crude oil fractions

All the fractions obtained from atmospheric residue are referred to as the “heavy fractions”. Another parameter used to classify crude oil is its density or API gravity. Heavy oils are typically considered as crude oil with a gravity of less than 20° API. Compared to the conventional crude, heavy oil has a much higher viscosity (and lower API Gravity) (James G. Speight, 2014). For this reason, heavy oil does not flow easily under original reservoir condition (Zou, 2017). Its recovery from the subsurface reservoir is more difficult compared to the lighter oil.

2.2 SARA Fraction

Crude oil is a complex mixture of numerous components (Wauquier, 1995). No complete chemical analysis of crude oil exists. For practical purposes, the liquid phase of crude oil is commonly grouped into four different solubility classes, which are: saturates, aromatics, resins and asphaltenes, popularly referred to as SARA (Gudmundsson, 2017). Figure 2.2 below shows a schematic representation of the SARA classification of crude oil. The saturates, aromatics and resins are collectively known as the maltene phase.

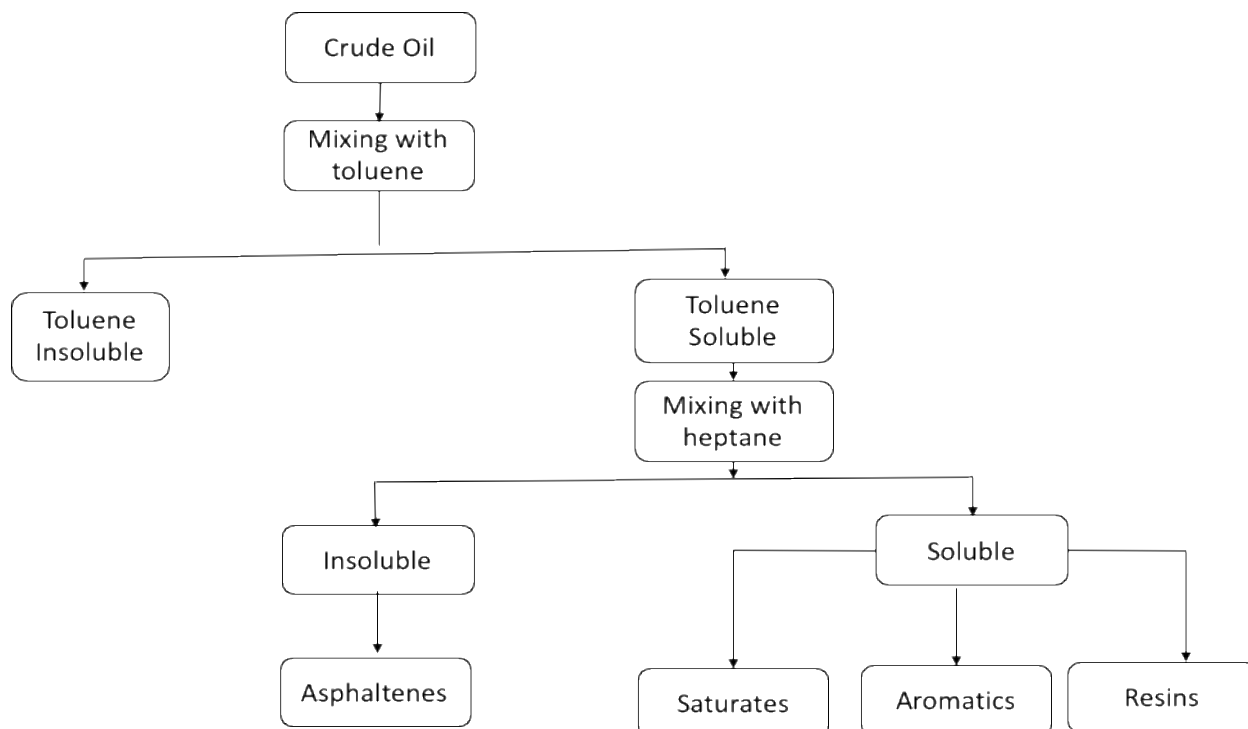


Figure 2.2: Schematic representation of SARA classification of crude oil

The saturates fraction of crude oil consists of (i) *Paraffins*, which are made up of straight or branched chain saturated hydrocarbons and (ii) *cycloparaffins, also known as naphthenes*, which are saturated cyclic hydrocarbons that may have one or more paraffin side-chains. The aromatic species contain one or more aromatic ring connected to a naphthalene ring or a paraffinic chain (Speight, 2014). Resins are made up of large polar molecules and often contain heteroatoms such as sulphur, nitrogen and oxygen. Resins are similar in structure to asphaltenes; however, they have lower molecular weights, are less polar and contain more alkane groups. Their presence in crude oil has been reported to play a vital role in the stability of asphaltenes (Gudmundsson, 2017). Asphaltenes are the most aromatic, most polar and heaviest component of crude oil. They are defined as a class of polyaromatic hydrocarbons that are soluble in toluene and insoluble in n-heptane (Orbulescu, Mullins, & Leblanc, 2010). Asphaltenes are commonly defined by their solubility class, rather than a molecular property, because it is a convenient method used to isolate asphaltenes from crude oil (Groenzin & Mullins, 1999). The in-depth study of asphaltenes has become necessary due to the significant impact they have on oil and gas recovery and processes.

2.3 Properties of Asphaltenes

Since asphaltenes, consisting of hundreds of thousands of molecules, is a solubility class, their physical and chemical characterization is generally challenging. The crude oil source from which the asphaltenes were isolated, as well as the isolation method used to separate the asphaltenes are some of the factors that determine their composition (Ramirez-Corredores, 2017a). While properties such as the types of functional groups, elemental composition and density of asphaltenes from different sources are similar and well established, some other properties such as structure and molecular weight are still debatable (Yarranton, 2005). Some of the different properties of asphaltene are discussed below.

2.3.1 Asphaltene Composition

Asphaltenes consist of carbon, hydrogen, oxygen, nitrogen, sulphur and trace amounts of other heteroatoms. Asphaltenes extracted from different sources have shown constant chemical composition, however, the range of this composition differ (Speight, 2004b). Typically, the

hydrogen to carbon ratio of asphaltenes varies depending on which precipitating agent is used. The use of n-pentane as the precipitating agent yields asphaltenes with a higher H/C ratio compared to the H/C ratio of asphaltenes obtained using n-heptane as shown in Table 2.1. However, the n-heptane precipitate shows higher nitrogen - to -carbon, oxygen – to - carbon, and sulphur-to-carbon ratio, which is an indication of the presence of higher heteroatoms compared to the degree of aromaticity.

Table 2.1: Elemental composition of various asphaltenes (Yen & Chilingarian, 1994)

Source	Precipitating medium	Composition (wt. %)					Atomic ratios			
		C	H	N	O	S	H/C	N/C	O/C	S/C
Canada	n-heptane	78.4	7.6	1.4	4.6	8.0	1.16	0.015	0.044	0.038
	n-pentane	79.5	8.0	1.2	3.8	7.5	1.21	0.013	0.036	0.035
Kuwait	n-heptane	82.0	7.3	1.0	1.9	7.8	1.07	0.010	0.017	0.036
	n-pentane	82.4	7.9	0.9	1.4	7.4	1.14	0.009	0.014	0.034
Iraq	n-heptane	80.7	7.1	0.9	1.5	9.8	1.06	0.010	0.014	0.016
	n-pentane	81.7	7.9	0.8	1.1	8.5	1.16	0.008	0.010	0.039
Iran	n-heptane	84.2	7.0	1.6	1.4	5.8	1.00	0.016	0.012	0.026
	n-pentane	83.8	7.5	1.4	2.3	5.0	1.07	0.014	0.021	0.022

2.3.2 Asphaltenes Molecular Weight

Different range of values generated from various measurement techniques have been reported for the molecular weight of asphaltenes (Speight et al., 1985; Speight, 1994; Yen, 1974). Adsorbed resins, precipitated asphaltenes and the low solubility of asphaltenes in the solvents used for its molecular weight determination are some of the factors that contribute to the varying ranges of molecular weights. Constituents of asphaltenes also have the ability to form aggregates in solutions thereby further complicating its molecular weight determination (Speight, 2014).

Some of the techniques commonly used for asphaltene molecular weight studies include vapor pressure osmometry (VPO), gel permeation chromatography (GPC), size exclusion chromatography (SEC), mass spectroscopy and microscopic techniques such as X-ray and neutron scattering studies. The values reported for these techniques range from 400 Da to 10,000 Da (Groenzin & Mullins, 2000). These apparent inconsistencies in asphaltenes molecular weight values greatly emphasize its intermolecular association property (Carbognani, Espidel, &

Izquierdo, 2000). With recent advances in measuring techniques such as time-resolved fluorescence depolarization (TRFD), Fourier transform ion cyclotron resonance mass spectroscopy (FTICR-MS) (Schneider, Andrews, Mitra-Kirtley, & Mullins, 2007), the molecular weight values of asphaltene monomers could be as low as 400 g/mol, and as high as 1000 g/mol, depending on the origin of the crude oil. An asphaltene monomer has an average value of about 750 g/mol (He, Lin, Li, Sui, & Xu, 2015).

2.3.3 Asphaltene structure

The asphaltene structure is commonly described by two different molecular models in literature. The first model as shown in Figure 2.3a is the “archipelago structure” which is characterized by smaller aromatic groups and the presence of branches and aliphatic bridges (Sheremata, Gray, Dettman, & McCaffrey, 2004). The other model, shown in Figure 2.3b, is known as the “island model”, the “continental model” or the “pericondensed structure” (Ramirez-Corredores, 2017b). This model is characterized by a core aromatic group that contains a large number of fused rings (usually seven or more) with pendant aliphatic groups (Sheremata et al., 2004).

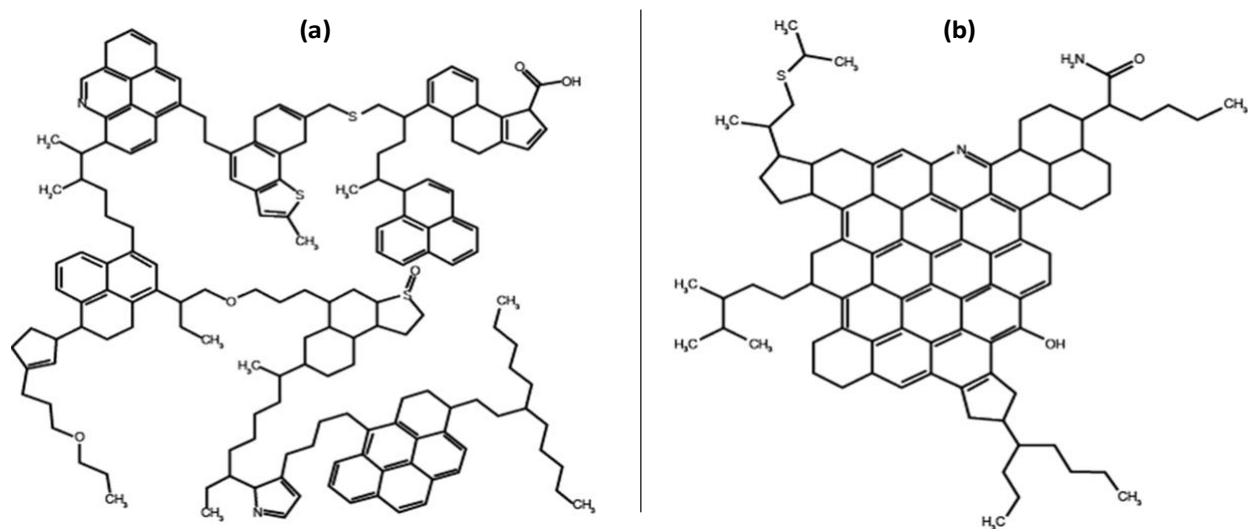


Figure 2.3: Asphaltene molecules structural representation for (a) Archipelago type-model (b) Continental type-model

A combination of different techniques such as X-ray diffraction, ^1H NMR spectroscopy and fluorescence emission spectroscopy confirm that all the aromatic C in the pericondensed asphaltene model is contained in a single aromatic cluster made up of about ten rings with peripheral substitution by alkyl rings (Groenzin & Mullins, 2000; Sheremata et al., 2004). On the other hand, experimental data from pyrolysis, thermal degradation and small angle neutron scattering technique support the archipelago model (Strausz, Mojelsky, & Lown, 1992; Strausz, Mojelsky, Lown, Kowalewski, & Behar, 1999).

2.3.4 Asphaltene Self-Association

One remarkable property of asphaltenes is their strong ability to self-associate in organic solvents (Sheu, 1996). The structural characteristics of asphaltenes play a role in their self-association (León, Rogel, Espidel, & Torres, 2000). Many investigations have studied the mechanism by which asphaltenes associate in crude oil and in solution. The motivation for asphaltenes self-association studies is because of the wide range of values obtained for the molecular weight of asphaltenes from different studies using a variety of techniques. Different ranges of driving forces that go from the very strong to the very weak, contribute to the intermolecular association between molecules of asphaltenes. However, these intermolecular forces are expected to be dominated by the dispersion, electrostatic and repulsive forces, depending on the average composition of the asphaltenes fraction (Merino-Garcia, Murgich, & Andersen, 2004).

Asphaltenes are believed to exist as monomers at concentrations below 50 mg/L, however, they start forming nanoaggregates (self-associate) as concentrations reach the critical nanoaggregate concentration (CNAC) of about 100 mg/L (± 50 mg) (Svalova, Parker, Povey, & Abbott, 2017). These CNAC values were determined using different methods such as fluorescence spectroscopy (Goncalves, Castillo, Fernández, & Hung, 2004), High-Q ultrasonics (Andreatta, Bostrom, & Mullins, 2005). This asphaltene aggregation progressive behaviour is characteristic of surfactants in organic solvents, typically beginning with the formation of dimers, followed by trimers and multimers. (Langevin & Argillier, 2016). As the concentration of asphaltenes gets higher (several g/L), it forms larger aggregates that contains about 20 solvated nanoaggregates referred to as clusters (Langevin & Argillier, 2016).

The exact mechanism of asphaltene self-association has not been established. However, the molecular modelling of aromatic core molecules and data obtained from techniques such as X-ray crystallography show that solid asphaltenes, just like graphite, have localized stacked aromatic sheets. These large aromatic cores of asphaltenes are likely to form colloidal stacks that are held together by π - π bonds. These colloidal aggregates are assumed to be dispersed in solution by resins that are surrounding the colloids or adsorbed on it (Yarranton, 2005). Another approach to self-association is the macromolecular approach where self-association likely appears as polymer structures of small and dispersed asphaltene aromatic clusters. The asphaltene aggregates formed here are likely to be held together by bonds such as π - π , acid-base and hydrogen bonds. The macromolecules may be dispersed by resins or disperse freely in solution (Yarranton, 2005). Due to the surface activity of asphaltenes, they are also known to form reverse micelles. This micellization behavior has been attributed to the non-identical monomer structures of asphaltenes (Sheu, 1996). In view of these different self-association mechanisms, one can assume that asphaltene from different sources could have varying structures and therefore self-associate through different mechanisms (Yarranton, 2005).

2.4 Asphaltene - Surface Interaction

Surfactants are generally surface active components, because of the interactions of their hydrophobic and hydrophilic portions with oil and water phases. Asphaltenes are insoluble in water due to the hydrophobic nature of its aromatic core. The attraction that exists between its heteroaromatic portion and water leads to its surface activity. The stronger this attraction is in comparison to the attraction between the hydrocarbon portion and polyaromatic skeleton, the stronger the adsorption of an asphaltene molecule to an interface, and the more effective it becomes as a surfactant. These asphaltene molecules become less surface active when the attraction between their hydrocarbon phase and the asphaltene skeleton increases as a result of an increase in the toluene content of the hydrocarbon phase. Asphaltenes consists of components with varying surface activities, therefore, some asphaltenes stay strongly surface active, while others become weak surfactants and lose their surface activity (Yarranton, Hussein, & Masliyah, 2000).

Asphaltenes adsorption is usually an undesirable phenomenon in reservoirs, pipelines and production systems, but can be very useful in the selective removal of asphaltenes in oil upgrading processes (Adams, 2014). Before asphaltenes are adsorbed on a surface, a series of processes lead to its precipitation and/or deposition. It is worth noting that asphaltenes precipitation may not necessarily lead to its deposition, though they have been used interchangeably in literature (Karan, Hammami, Flannery, & Artur Stankiewicz, 2003). Thermodynamic variables such as composition, pressure and temperature influence precipitation, but not deposition (Rastgoo & Kharrat, 2017). Karan et al. used precipitation as a term to define the formation of a new phase of solid or liquid from a bulk solution that typically involves the following steps: nucleation, growth and aggregation. While deposition was described as the formation of solid layers on a surface that already exists (Karan et al., 2003). Asphaltene deposition goes through these steps: precipitation, flocculation, migration of the flocculated asphaltene to the surface, adhesion of the asphaltenes to the surface, cohesion of the precipitated/flocculated asphaltenes with the already adsorbed ones onto the surface (Abu Tarboush & Husein, 2015).

Adsorption occurs as a result of differences in chemical potential which leads to the preferential partitioning of a solute at the interface between the bulk solvent and the solid adsorbent (Abu Tarboush, 2014). The chemical and structural characteristics of asphaltenes, as well as the chemical and physical properties of the adsorbent are very important factors in the adsorption of asphaltenes. Asphaltene adsorption can take place at different interfaces, depending on the kind of adsorbent used. Adsorbents can be mineral based such as clay, calcite, silica, dolomite (Socrates Acevedo et al., 2000; Marczewski & Szymula, 2002; Mendoza de la Cruz et al., 2009; Pernyeszi et al., 1998) or metal surfaces such as silica and alumina, glass, metal oxides and metal oxide NPs.

2.4.1 Adsorption on Mineral Surface

There are a number of chemical species as well as molecular forces present on a mineral surface, which enable favorable interactions (adsorption) with asphaltene molecules. These forces include electrostatic interactions, charge transfer interactions, van der Waals interactions, repulsion or steric interactions and hydrogen bonding (Cruz et al., 2009). Various mineral surfaces such as kaolinite (Wang, Liu, Tan, Xu, & Gray, 2016), quartz sand (Gonzalez & Taylor, 2016), clay

(Dudášová, Simon, Hemmingsen, & Sjöblom, 2008) have been used by different researchers to study asphaltene adsorption. The wettability of reservoir rock surface can be affected by asphaltene adsorption thus reducing the production of oil (Gonzalez & Taylor, 2016; Pernyeszi et al., 1998; Wang et al., 2016). Asphaltenes adsorption on minerals follow the Langmuir adsorption isotherm (González & Middea, 1987; Kokal, Tang, Schramm, & Sayegh, 1995; Tímea Pernyeszi et al., 1998), which is an indication of monolayer adsorption of asphaltenes. Some researchers have also reported multilayer adsorption (Sócrates Acevedo et al., 1995; Tímea Pernyeszi et al., 1998) shown to be as a result of aggregation and precipitation of asphaltenes (Castillo, Fernández, Ranaudo, & Acevedo, 2001). The reversibility of asphaltenes adsorption has also been examined. Wang et al., Dudasova et al., and other researchers using X-ray photoelectron spectroscopy, Quartz Microbalance techniques reported the irreversibility of asphaltene adsorption (Dudášová, Silset, & Sjöblom, 2008; Ekholm et al., 2002; Wang et al., 2016)

2.4.2 Adsorption on Metal Surface

The adsorption of asphaltenes onto metal surfaces is not as commonly studied as the adsorption on mineral surface. Some researchers have done studies using metal surfaces such as gold, stainless steel, aluminium, iron and copper (Alboudwarej, Pole, Svrcek, & Yarranton, 2005; Ekholm et al., 2002; Majid Mohammadi, Sedighi, Hashemi Kiasari, & Hosseini, 2015a; Rudrake, Karan, & Horton, 2009). Ekholm et al (Ekholm et al., 2002), using quartz crystal microbalance with dissipation measurements (QCM-D) studied the adsorption of asphaltenes onto a hydrophilic gold surface. They worked with concentrations in the range of 50 – 10,000 ppm and reported an adsorbed amount of up to 8 - 9 mg/m² at 10,000 ppm. Alboudwarej et al (Alboudwarej et al., 2005) noted that the value reported is double that of asphaltenes adsorption on minerals and suggested it may be as a result of electrodeposition effects. Alboudwarej et al (Alboudwarej et al., 2005) studied asphaltene adsorption using stainless steel, aluminum and iron powders. They found that stainless steel had the most adsorption, while aluminum has the least and attributed this to stainless steel having a better electrostatic bonding with asphaltene because of the presence of elements such as chromium, carbon, silicon, nickel, phosphorus and sulphur in its structure. However, they reported

that the maximum amount of asphaltenes adsorbed on the metal surfaces were similar to the corresponding reported values for minerals, 1- 4 mg/m².

2.4.3 Adsorption onto NPs

The use of metal oxide NPs is recently on the increase because of their unique properties (Maher & Husien, 2007; Nassar, Hassan, & Vitale, 2014). They have considerable potential for the selective upgrade of adsorbed asphaltenes, as a result of their catalytic ability (Adams, 2014). NPs have shown high adsorption capacity and fast adsorption kinetics, which has been attributed to its high surface area (Abu Tarboush & Husein, 2012a). They are also highly effective and environmentally sustainable (Setoodeh, Darvishi, & Lashanizadegan, 2017). Several investigations have been carried out using both commercial and in-situ prepared NPs such as NiO, Fe₂O₃, Fe₃O₄, Al₂O₃ (Abu Tarboush & Husein, 2015; Ezeonyeka et al., 2018; Farahmandjou & Soflaee, 2015; Hosseinpour, Mortazavi, Bahramian, Khodatars, & Khodadadi, 2014; Husein & Alkhaldi, 2014; Nassar; Hassan; Pereira-Almao, 2011; Nassar, Hassan, & Pereira-Almao, 2011b; Shayan & Mirzayi, 2015b; Shen et al., 2009).

From the various adsorption experiments that have been carried out by different researchers, the following factors have been shown to play a role in the amount of asphaltenes adsorbed (Clementz, 1976; Czarnecka & Gillott, 1980; Dudášová, Simon, et al., 2008; Hlady, Lyklema, & Fleer, 1982; Lian, Lin, & Yen, 1994; Simon, Jestin, Palermo, & Barre, 2009).

- The source of the asphaltenes, which is dependent on the chemistry of the crude oil as well as its origin.
- Molecular weight which determines the amount of asphaltene adsorbed, as species with higher molecular weight adsorb preferentially adsorbed onto a surface.
- The resin content of the asphaltene sample which depends on the type of isolation method used, the precipitating agent, as well as the contact time.
- The surface chemistry of the adsorbent
- The polarity of the solvent used for the asphaltene dissolution.

2.5 Adsorption Isotherm

An asphaltene adsorption isotherm is a measure of the amount of adsorption versus the concentration of the adsorbing species (Foo & Hameed, 2010). The adsorption capacity and adsorption affinity of asphaltene-adsorbent systems are obtained from the adsorption isotherm (Adams, 2014). Adsorption equilibrium is reached when the phase containing the adsorbate has been in contact with the adsorbent for a sufficient amount of time, thereby creating a balance between the adsorbate concentration in the bulk solution and the interface concentration (Foo & Hameed, 2010). Generally, the isotherms reported for asphaltene adsorption experiments are either the Langmuir (Dudášová, Simon, et al., 2008; Hosseinpour et al., 2013; Nassar, Hassan, & Pereira-Almao, 2011b; Nassar et al., 2014; Setoodeh et al., 2017), or Freundlich type (Marczewski & Szymula, 2002). The Langmuir adsorption isotherm is a two-parameter isotherm that was first developed to describe gas-solid-phase adsorption onto activated carbon. This model assumes a monolayer adsorption (one molecule thickness of the adsorbed layer). It also assumes that adsorption can only occur at a fixed number of definite localized sites, which are identical and equivalent, with no lateral interactions nor steric hindrance between the molecules (Foo & Hameed, 2010). The Langmuir isotherm also describes adsorption as homogeneous, where all adsorbent sites have equal affinity for the adsorbate. It is shown graphically by a plateau, which is an indication of an equilibrium saturation point where further adsorption cannot take place as soon as one molecule occupies a site. This model is represented mathematically as shown below:

$$q_e = q_m \frac{K_L C_e}{1 + K_L C_e} \quad (E2.1)$$

where q_e is the equilibrium adsorbate uptake per surface area of the adsorbent (mg/m^2), C_e is the equilibrium concentration of the adsorbate (mg/L), K_L is the Langmuir equilibrium constant which relates to the affinity of the binding sites (kg/mg), q_m is the maximum equilibrium uptake by the adsorbent (mg/m^2). A plot of q_e versus C_e gives the adsorption isotherm.

The Freundlich isotherm model is applied to multilayer adsorption where the distribution of adsorption affinity over a heterogeneous surface is non-uniform (Foo & Hameed, 2010). It was

first developed for the adsorption of animal charcoal where it showed that the ratio of the adsorbate onto a given mass of adsorbent to the solute was not a constant at different solution concentration (Foo & Hameed, 2010). Therefore, the amount of adsorbate adsorbed is the summation of adsorption on all sites where the stronger binding sites are occupied first (Foo & Hameed, 2010). A mathematical representation of this model is as shown in E2.2:

$$q_e = K_F C_e^{1/n} \quad (\text{E2.2})$$

K_F and $1/n$ are Freundlich constants which denote adsorption capacity and adsorption intensity respectively (Desta, 2013).

In a review on asphaltene adsorption by Adams (Adams, 2014), he noted some factors that may have significant effects on asphaltene adsorption isotherms. Some of these factors include sorbent type, adsorption experiment duration, and strength of solvent used for asphaltene dissolution, the amount of resins present, asphaltene source, sample preparation, reaction conditions and particle size. For instance, using mineral based sorbents such as kaolinite or quartz gave an adsorption isotherm that was a good fit to the Langmuir I type, whereas adsorption onto dolomite showed a multilayer behavior that was fit to a modified Langmuir isotherm (Adams, 2014). Dudasova et al (2008) reported that data obtained using QMC gave a multilayer formation compared to using other methods for the same sorbent. Nassar et al. (Nassar, Hassan, & Pereira-Almao, 2011a) showed that nano-alumina fitted a monolayer Langmuir isotherm, while micro-alumina was a good fit to the Freundlich. Goual et al. (Goual, Horváth-Szabó, Masliyah, & Xu, 2005) observed that gold gives monolayer Langmuir isotherm initially, but changes to multilayer adsorption after a long period.

2.6 The use of UV-Vis for Adsorption Studies

Ultraviolet-visible (UV-Vis) spectroscopy has been widely used to study the adsorption of asphaltene on different surfaces. UV-Vis spectroscopy is a simple, versatile, accurate and cost effective physical technique that uses light in the visible, ultraviolet and infrared range to determine the concentration of the absorbing species (Shah, Shah, Pawar, & Gayakar, 2015). Every

chemical compound has the ability to absorb, transmit, or reflect light (electromagnetic radiation) over a certain range. A measurement of how much light a chemical substance absorbs or transmits is called spectroscopy (Sanda, Victor, Monica, & Alina, 2012). According to Beer-Lambert's law as shown in E2.3, a linear relationship exists between a sample's concentration and its absorbance; i.e., the absorbance is directly proportional to the concentration of the absorbing species in the solution and the path length (Shah et al., 2015).

$$A = \log \left(\frac{I_0}{I} \right) = abc_1 = \epsilon bc_2 \quad (\text{E2.3})$$

where I_0 = intensity of the incidence light beam, I = intensity of the transmitted beam, A = absorbance, a = the absorptivity constant, b = the path of light in centimeters, c_1 = concentration of the absorbing specie in g/L, ϵ is the molar absorptivity constant, and c_2 is the concentration of the absorbing species in mol/L (Dulski, 1996).

Therefore, UV-Vis spectroscopy can be used to determine the asphaltene concentration in a solution. Depending on the range of wavelength of the light source, a spectrophotometer can be classified into two different types:

- The UV-Visible spectrophotometer which uses light over the ultraviolet range (200 - 400 nm) and the visible range (400 – 800 nm) of the electromagnetic spectrum
- Infrared Spectrophotomer, which uses light over the infrared range (700 – 15000 nm) of the electromagnetic spectrum.

A spectrophotometer can either be single beam, double beam, or simultaneous with these generic features seen in Figure 2.5: a light source (deuterium or tungsten lamp), wavelength selector, sample containers, detector and signal processor and read out.

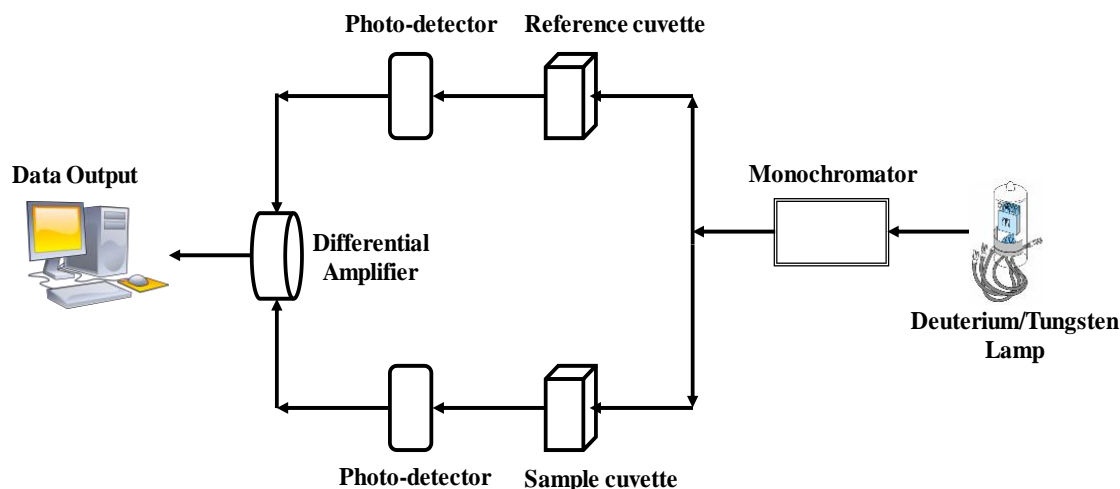


Figure 2.4: Schematic of a double beam UV-Visible Spectrophotometer.

UV- adsorption depends on the chemical bonds of the adsorbing species. There is a change in the electronic state of the molecules of a chemical compound when it absorbs light in the UV or visible region. The electron present in this sample absorbs energy from the light source and is promoted from any of its ground state orbital to an excited state orbital with higher energy levels or to an antibonding orbital (Shah et al., 2015). These ground state orbitals include the σ molecular orbital, the π molecular orbital and the n -atomic orbital, while the antibonding orbitals include: σ^* orbital and π^* orbital. As shown in Figure 2.5, the possible electron transition that can occur when ultraviolet and visible light is absorbed include σ to σ^* , n to σ^* , n to π^* , π to π^* .

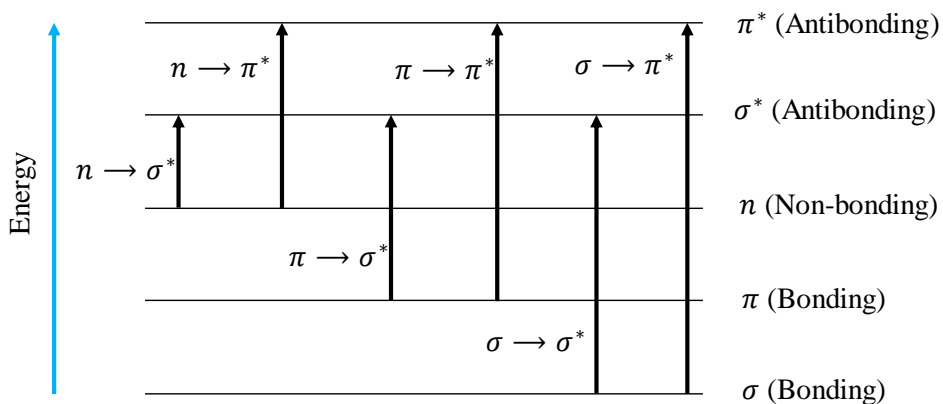


Figure 2.5: Possible electron transitions

Maximum absorption wavelength and the absorption intensity are usually determined by molecular structure. For instance, very high energy is required for transitions from σ to σ^* and n to σ^* , therefore it occurs in the far ultraviolet region. For this reason, saturated groups do not show strong absorption in the ordinary ultraviolet region, while molecules with unsaturated bonds require less amount of energy for their transitions from n to π^* , π to π^* .

2.7 Characterization Techniques

The theories and principles of some of the techniques used in this thesis for asphaltene characterization are explained here.

2.7.1 Thermogravimetric analysis (TGA) technique

The thermogravimetric analysis (TGA) technique is a thermal analysis technique that measures the changes in weight of a sample under a certain temperature-time program, working on a beam balance principle (Kutz, 2013). A TGA instrument has a thermobalance that has a capacity of about a few hundred milligrams and records sample weight with a sensitivity of about $1\mu\text{g}$. It also has a furnace that operates in the temperature range of about $50 - 1000\text{ }^\circ\text{C}$ with a heating ramp up to $100\text{ }^\circ\text{C} / \text{min}$ (Ratna, 2009). Under inert atmosphere, a TGA assay helps to estimate the thermal stability of the sample and evaluates changes in weight due to volatilization of moisture and decomposition of organic compounds (Kutz, 2013). In an inert or oxidative atmosphere, TGA may be used to study the thermal stability of a material, after which a TGA curve is obtained that helps understand the decomposition mechanism of the material. The TGA curve is affected by the heating rate and the sample size. The decomposition temperature of the sample increases as the rate of heating and sample size increases. The kinetics of the reaction can also be affected by the gas flow rate, the decomposition temperature, the particle size, the way it is packed, therefore, it is important to maintain an identical condition of variables if the thermal stability of two materials are to be compared (Ratna, 2009).

2.7.2 FTIR

Infrared (IR) spectroscopy is one of the vital analytical techniques widely used in the characterization of all of forms of materials based on the vibrations of the atoms of the molecules present in the material. IR spectroscopy generally provides two types of structural information about a sample. The first is the electronic structure using the valence and core electrons known to determine the samples chemical and physical properties. The second is the geometric structure that tells the location of the atoms in the molecules (Thomas et al., 2014a).

IR spectroscopy uses infrared radiation, which is typically passed through a sample that has a permanent or induced dipole moment to generate an infrared spectrum. The amount of incident radiation absorbed at a particular energy is recorded. The generated absorption spectrum has energy peaks that correspond to the vibrational frequency of a molecule, thereby making it possible to qualitatively identify the bond types in the sample. The energy of the electromagnetic radiation transmitted through the sample, which is a function of the wave number, or frequency is recorded by the IR spectrometer (Thomas et al., 2014a).

The FTIR spectrometer typically consists of the following components as shown in Figure 2.6: a source of infrared (usually a heated coil of wire), an interference modulator (Michelson interferometer), a sample cell and an infrared detector. The interferometer is an optical device that consists of a beam splitter, a fixed mirror and a moveable mirror that needs to be aligned correctly at all times, because the accurate performance of the FTIR is largely dependent on it (Battikha, 2007). FTIR functions by the creation of interference in a beam of light. A light beam from a source is spilt into two; a varying phase difference is introduced into one of the resultant beams. The two beams then recombine and an interferogram is recorded after measuring the interference signal (Crompton, 2008). The FTIR has the ability to produce good quality infrared spectra in a short time (Thomas et al., 2014a).

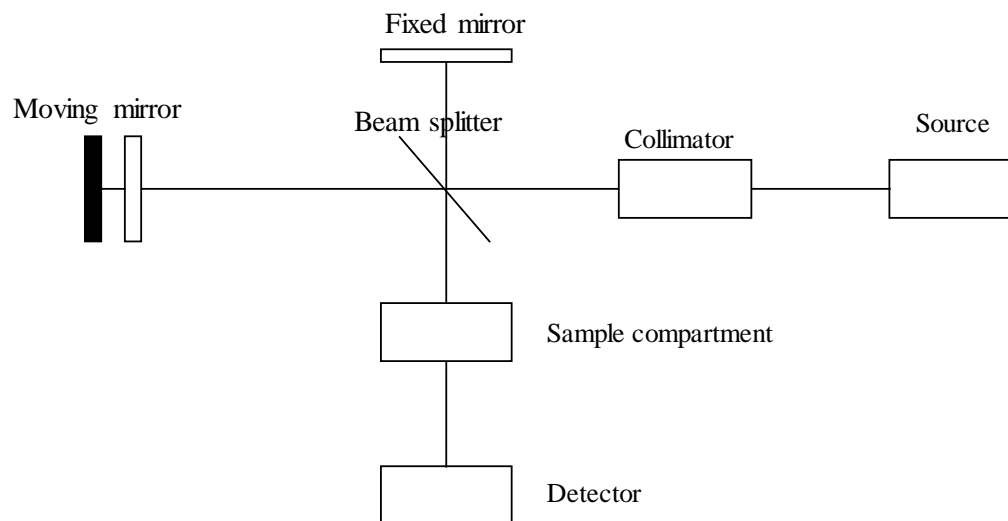


Figure 2.6: DRIFTS analyzer

2.7.3 Dynamic light scattering

The dynamic light scattering (DLS) technique is a very effective, convenient and non-destructive method used for the direct measurement of mean particle size distribution in various scientific studies such as colloidal science, particle aggregation, micellar systems, suspensions, polymers, NPs, emulsions and so on (Thomas, Chan, Pothen, Rajisha, & Maria, 2014b). Figure 2.7 shows a schematic of a DLS apparatus.

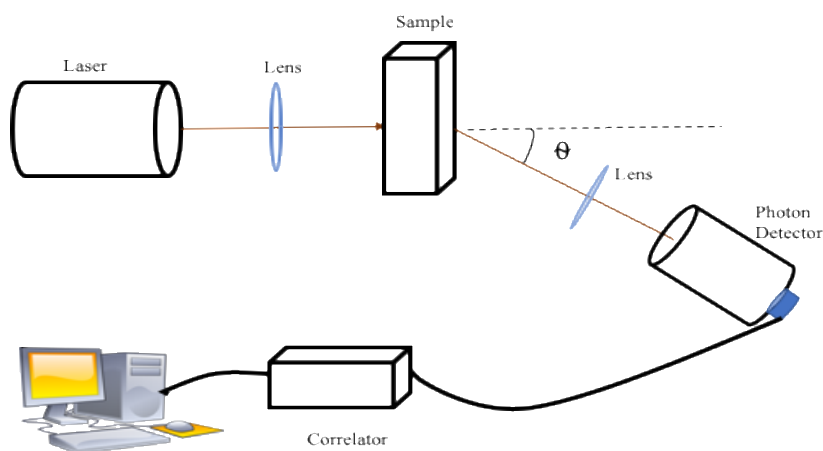


Figure 2.7: A basic schematic representation of a light scattering measurement

DLS also referred to as quasi-elastic light scattering or photon correlation spectroscopy relies on the random Brownian motion that particles undergo when suspended in a continuous medium (Ullmann, 2005). In the scattering of a photon of light by a moving particle, a small exchange of energy occurs between them, which results in the particle either gaining energy or losing energy to the photon and thus experiencing an energy shift (Cosgrove, 2010). A digital autocorrelator measures the time-dependent fluctuation in the light scattering intensity of these particles (Baalousha & Lead, 2015). These fluctuations, which are caused by the random Brownian motion, are directly related to the translational rate of diffusion of the particle through the solvent. Consequently, there is a relationship between the diffusion coefficient and the hydrodynamic radius of the particle through the Stokes-Einstein equation.

In the DLS technique, the scattering intensity observed is a function of the scattering angle, particle size and shape, the instrument optics, and the measurement duration (Baalousha & Lead, 2015). This technique makes it possible to characterize particles from the nanometer range to the micrometer range. However, small particles in the solution diffuse relatively faster, leading to a rapidly fluctuating intensity signal compared to the slower diffusion of larger particles (Banerjee & Tyagi, 2012).

2.7.4 XRD

X-ray diffraction (XRD) is a useful technique in the study of the crystal structure of solids. Diffraction techniques generally provide information on the actual locations of atoms within a solid by studying the intensities of diffracted beams (Davis, 1993b). The Bragg's diffraction law, shown in E 2.4, is the main principle on which XRD is based.

$$2d \sin \theta = n\lambda \quad (\text{E2. 4})$$

where d is the inter-planar spacing, θ is the diffraction angle, n is an integer and λ is the incident wavelength.

An X-ray diffractometer usually has the following components: a source of X-ray, a goniometer, a counter tube and counting electronics. A chart of peak intensity versus 2θ is typically used to

obtain XRD results. Bragg's law is then used to convert the angle to the spacing between crystallographic planes. At a given θ , the intensity of the diffracted beam is related to a number of structural and geometrical factors (Davis, 1993b). Figure 2.8 is a representation of the basic principle underlying XRD. It shows the incident beam, normal to the reflecting plane, and the scattered/diffracted beam are coplanar. In addition, the scattering angle, which is the angle between the incident and the scattered beam, is always 2θ (Bhattacharya, Kamal, & Gupta, 2008).

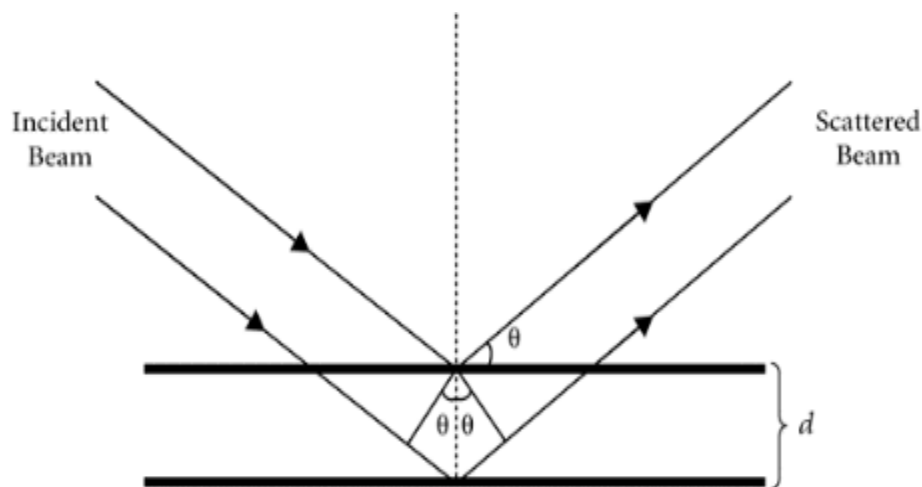


Figure 2.8: Representation of the XRD process (Bhattacharya et al., 2008).

2.7.5 Transmission electron microscopy

Transmission Electron Microscopy (TEM) is a powerful microscopy technique used mainly for thin film structure characterization (Davis, 1993a). This technique functions by transmitting a beam of electrons through an ultra-thin sample. The electrons then interact with the sample and an image is produced, which is magnified and focused onto an imaging device such as a fluorescent screen (Gianfrancesco, 2017). As shown in Figure 2.9, most transmission electron microscopes are composed of an electron source, a number of focusing and enlarging electromagnetic lenses and photographic systems, all contained in a high vacuum ($10^{-4} - 10^{-5}$ torr).

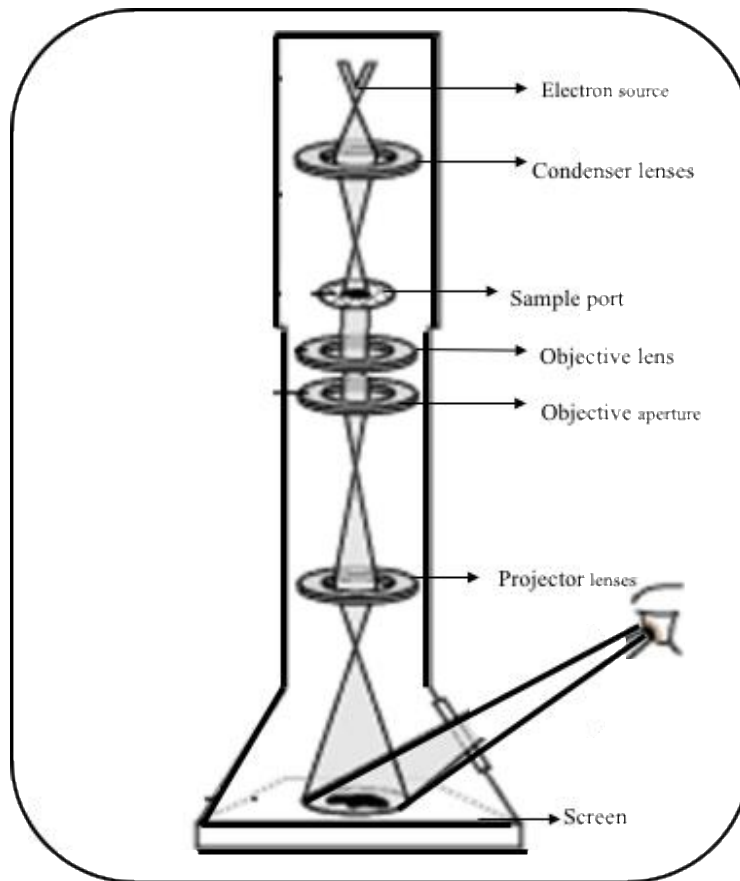


Figure 2.9: Schematic Diagram showing TEM

TEM allows the detailed study of much localized regions of a sample due to its very high magnifications and high resolution. TEM produces variations in lattice orientations, which makes it capable of detecting and analyzing various internal structural defects, such as lattice imperfections, very small precipitates, grain boundaries and interfaces, etc. (Davis, 1993a). It is very important that any sample for TEM testing is kept thin enough to allow the electron beam penetrate through to form images (Davis, 1993a).

Chapter 3: Experiment Methods

3.1 Materials and Methods

3.1.1 Materials

C7-asphaltenes were extracted from Athabasca vacuum residue by addition of *n*-heptane (99 % HPLC grade, Sigma Aldrich, ON) following a procedure detailed elsewhere (Nassar, Al-Jabari, & Husein, 2008). The dried asphaltenes were re-dissolved in toluene (99.5%, VWR, Canada) to prepare model solutions of different asphaltenes concentration. Commercial Fe_2O_3 (dp < 50 nm, Sigma-Aldrich, USA), Fe_3O_4 (20-30 nm, Nanostructured & Amorphous Materials, Inc., TX) and Al_2O_3 (<50 nm particle size, Sigma-Aldrich, USA) were used as adsorbents.

3.1.2 Methods

3.1.2.1 Characterization of the extracted C7-asphaltenes.

An elemental analyzer (2400 series II, Perkin Elmer Inc., AB, Canada) was used to determine the H: C ratio of the asphaltenes. X-ray diffraction (XRD) and DRIFTS on a Nicolet iS50 spectrophotometer (ThermoFischer, USA) with a diffuse reflection accessory (Praying Mantis, Harrick Scientific Products Inc., USA) were used to determine the functional groups and structures present in the asphaltenes molecules. FTIR-grade potassium bromide (KBr) (Sigma-Aldrich, Germany) was mixed with the C7-asphaltenes at a ratio of 40:1 of KBr powder to asphaltenes. The mixture was then placed on the diffuse reflection accessory and the sample was scanned 64 times at a wavelength interval of 400 cm^{-1} to $4,000\text{ cm}^{-1}$ with a resolution of 4 cm^{-1} . The X-ray pattern of the asphaltenes was collected on an ULTIMA III X-ray diffractometer (Rigaku Corporation, The Woodlands, TX, USA). The diffractometer uses a $\text{Cu K}\alpha$ radiation as the X-ray source. The scans were performed in the range of 3° to 90° of 2θ using a 0.02° step and a counting time of 2.0° per min, operating at 40 kV and 44 Ma.

DLS was performed on a Zetasizer Nano ZSP (Malvern instruments limited, Worchester, UK). The refractive index of asphaltenes in model solutions was measured using a RM 40 refractometer

(METTLER TOLEDO AG, Schwerzenbach, Switzerland) with a light-emitting diode (LED) at a reference temperature of 25°C and a wavelength of 589.3 nm. The asphaltenes solution was placed on the sapphire measuring prism and left for about 60 seconds to ensure temperature equilibration before the readings were taken. The measuring prism was cleaned thoroughly with water, followed by acetone, and then dried before the measurement of another sample.

3.1.2.2 Characterization of the NPs and the adsorbed asphaltenes.

The NPs were characterized using TriStar 2000 surface area analyzer, TEM, DRIFTS, and XRD. TriStar 2000 surface area analyzer (Micromeritics Instrument Corporation, USA) uses N₂ adsorption and desorption to provide an estimate of the surface area. Sample preparation involved degassing overnight under N₂ flow at 150°C. The Brunauer-Emmet-Teller (BET) equation was used to determine the surface area of the samples. Total pore volume was calculated by N₂ uptake at the relative pressure $P/P_0 = 0.99$ using Barrett-Joyner-Halenda (BJH) method.

TEM was used to determine the particle size distribution, hence providing another estimate of the surface area. TEM analysis was carried out on a Tecnai TF20 G2 FEG-TEM (FEI, Oregon, USA) with a FEI low background double tilt holder (PW6595/15). A small amount of the different NPs was dispersed in methanol using sonication. A thin layer of the dispersion was deposited onto a copper grid and allowed to dry. The copper grid was then introduced to the TEM and various bright field images were taken. X-ray pattern of the NPs were collected using the ULTIMA III X-ray diffractometer, as detailed earlier. The JADE program was used to compare the X-ray patterns and the database as well as literature. The DRIFTS technique was also used to identify the nature of adsorbed material onto the NPs, as detailed above. Control samples consisting of only asphaltenes or NPs were run for comparison.

3.1.2.3 Preparation of the heavy oil model solutions

Heavy oil model solutions were prepared by dissolving a certain mass of the C7-asphaltenes into toluene to give a 10,000 ppm stock solution. The stock solution was mixed for about 30 min at 200 rpm and was inspected for any visible agglomeration or precipitation. Different concentration

model solutions were obtained by diluting samples of the stock solution with a specified mass of toluene to initial asphaltenes. The final asphaltene concentrations ranged from 200 to 10,000 ppm.

3.1.2.4 Adsorption experiments

UV-Vis spectrophotometer (Nicolet evolution 100, Thermo instruments Inc., Canada) standards were prepared in-house at precise concentrations of 20 ppm, 50 ppm, 100 ppm and 120 ppm by diluting a 150 ppm asphaltene stock solution with toluene. The reference cell contained toluene. Three different calibration curves were established at 410 nm, 500 nm and 700 nm. These wavelengths were considered appropriate and within the instrument absorbance threshold as they provided sufficient sensitivity to measure asphaltenes concentrations (Alboudwarej et al., 2005) without exceeding the instrument detection limit. Straight lines going through the origin were established with slopes and coefficients of determination, R^2 , as summarized in Table 3.1. The different wavelength of light used for the measurements gave different slopes, this could be because the different asphaltene components interact differently at the various wavelengths. Also, the excited state the asphaltene components go to is dependent on the wavelength of light used. Figure 3.1 suggests that the Beer-Lambert relationship applied to the standards (Zhao & Shaw, 2007). Three replicates were provided and the 95% confidence intervals were small. Note that control samples of NP dispersions in toluene did not lead to detectable UV-Vis absorption peaks; therefore, interference from the NPs was deemed nil.

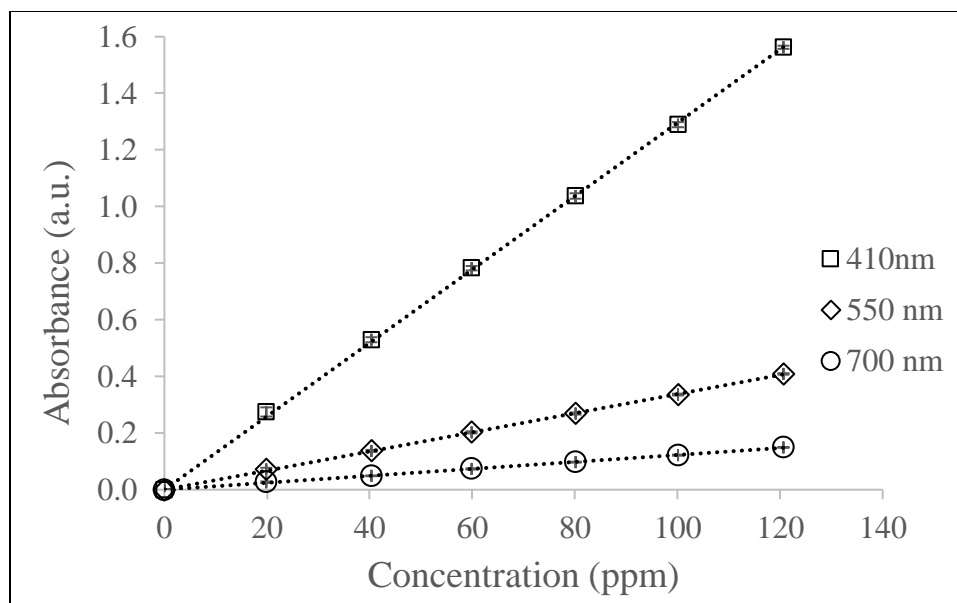


Figure 3.1: Calibration curves for asphaltenes in toluene. The error bars are too small to be seen.

Table 3.1: Slopes and coefficient of determination for the different UV-Vis calibration curve

Wavelength	410 nm	550 nm	700 nm
Slope	0.013	0.00338	0.00123
R ²	0.9998	0.9998	0.9996

Batch adsorption experiments commenced by adding 0.100 g of the NPs to 10.0 mL volume of the toluene model solutions of known initial concentration of asphaltenes. The tightly sealed vials were placed in an incubator shaker at 25 °C and were left to shake at 300 rpm for different time durations. Preliminary tests confirmed that equilibrium was achieved in less than 30 min, as shown in Figure 3.2.

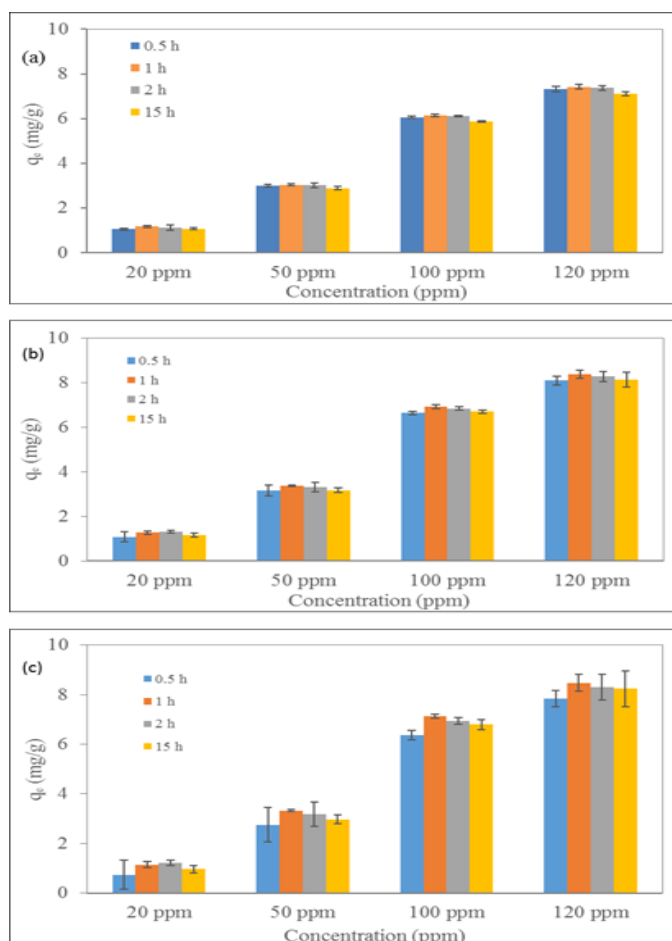


Figure 3.2: Asphaltenes uptake, q , for different concentrations of asphaltenes solution versus time at (a) 410 nm (b) 550 nm (c) 700 nm.

Hence, 60 min runs were chosen to establish equilibrium for the rest of the runs, while ensuring minimum evaporation of the solvent.

Following mixing, the vials were centrifuged at 8,000 rpm for 15 min in order to separate the particles and the corresponding adsorbed asphaltenes. Note that centrifugation alone did not impact the concentration of asphaltenes in any of the samples. The resulting supernatant was decanted and its concentration of asphaltenes was analyzed using the UV-Vis spectroscopy. In order to provide another measure for asphaltenes uptake, which is a core objective of the current study, the NPs together with the adsorbed asphaltenes were dried in an oven and further introduced to a simultaneous thermal analyzer, STA (STA 6000, Perkin Elmer Inc., USA). The sample was

subjected to a temperature increase from 30 °C to 800 °C with a temperature ramp of 10 °C/min under 30 mL/min of airflow. Mass loss due to NPs, obtained from control samples, was subtracted from the total loss to obtain the loss due to adsorbed asphaltenes. Mass balance was used to calculate the amount of asphaltenes adsorbed onto the NPs using the following formula:

$$q_e = \frac{M (C_o - C_e)}{m} \quad (\text{E3.1})$$

where q_e is the asphaltenes uptake (mg asphaltenes/g NP), M is the mass of the model solution (g), C_o is the initial concentration of asphaltenes in the model solution (ppm), C_e is the equilibrium concentration of asphaltenes in the supernatant (ppm) and m is the mass of the NPs (g). It should be noted that both C_o and C_e were measured for every sample using UV-Vis spectroscopy, while for STA measurements, C_e was back calculated using mass balance, i.e. knowing C_o , the mass of asphaltenes taken up by the NPs, and assuming constant mass of the oil phase.

The uptake based on surface area was calculated using E3.2 as follows.

$$q_e = \frac{M (C_o - C_e)}{A} \quad (\text{E3.2})$$

where A is the total surface area of the NPs (m²) estimated by TriStar using BET equation. BET is commonly used as the representative surface area of NPs in literature (Abu Tarboush & Husein, 2012a; Franco, Montoya, Nassar, Pereira-Almao, & Cortés, 2013). Uncertainties expressed as 95% confidence interval calculated from three replicates was provided for C_e and q_e and presented in the figures.

Chapter 4: Results and Discussion

4.1 Asphaltenes Characterization

The H:C mass ratio of the asphaltenes as obtained from elemental analysis was 0.12, whereas the mole ratio was 1.25. This ratio is in the range of other asphaltenes reported in the literature (Alboudwarej et al., 2005; Zhao & Shaw, 2007). Figure 4.1 depicts the XRD pattern of the asphaltenes extracted in this study, which displays the same features as those reported in the literature (Asaoka, Nakata, Shiroto, & Takeuchi, 1983; Hosseinpour et al., 2014). The pattern includes two superimposed peaks, a γ band at $2\theta = 19.71^\circ$ produced by the aliphatic portion and a graphene band at $2\theta = 25.06^\circ$ produced by the aromatic portion of the asphaltenes (Tanaka et al., 2004). A third diffraction peak also related to the aromatic sheets of the asphaltenes is observed at $2\theta = 43.01^\circ$ (Hosseinpour et al., 2014). A prominent γ band suggests a higher aliphatic portion compared with the aromatic portion of the crystalline material (Asaoka et al., 1983).

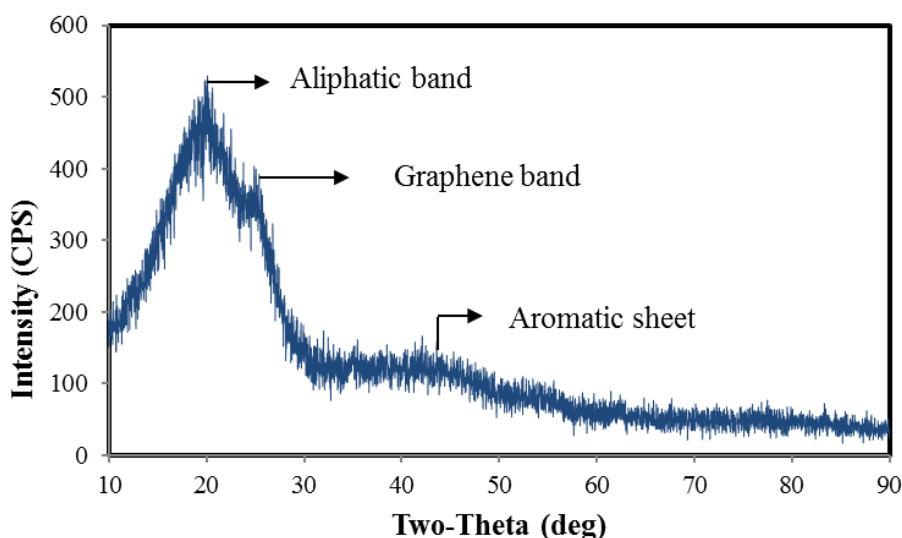


Figure 4.1: XRD pattern for virgin C7-asphaltenes extracted in this study.

The XRD pattern of the asphaltenes was analyzed in detail to provide a fundamental understanding of the asphaltenes structure. Even though the XRD peaks are not very sharp, other literature studies have used similar peaks to extract structural parameters of asphaltenes (Andersen, Jensen, & Speight, 2005; Schwager et al., 1983; Shirokoff, Siddiqui, & Ali, 1997). More importantly, the

results obtained in this study are in good agreement with other literature techniques such as NMR, SAXS, SANS (Eyssautier et al., 2011; Lisitza, Freed, Sen, & Song, 2009; Tanaka et al., 2004). Equation E4.1 was used to calculate the layer distance between the aromatic sheets from the maximum of the graphene band (d_m). Equations. E4.2 to E4.5 were used to calculate the distance between the saturated portions of the molecules represented by the γ -band (d_r), the average diameter of the aromatic sheets (L_a), the average height of the cluster of aromatic sheets perpendicular to the plane of the sheets (L_c) and the number of aromatic sheets in a stacked cluster (M_e), respectively (Andersen et al., 2005; Shirokoff et al., 1997; Yen, Erdman, & Pollack, 1961). The average number of aromatic rings in each aromatic sheet (R_a), the number of carbons per aromatic structural unit (C_{AU}), and the aromaticity index of asphaltenes (f_a) were calculated based on equations. E4.6 to E4.8, respectively.

$$d_m = \frac{\lambda}{2 \sin(\theta_{002})} \quad (\text{E4.1})$$

$$d_r = \frac{\lambda}{2 \sin(\theta_\lambda)} \quad (\text{E4.2})$$

$$L_a = \frac{1.84\lambda}{\omega \cos(\theta_{10})} = \frac{0.92}{B_{\frac{1}{2}}} \quad (\text{E 4.3})$$

$$L_c = \frac{0.9\lambda}{\omega \cos(\theta_{002})} = \frac{0.45}{B_{\frac{1}{2}}} \quad (\text{E4.4})$$

$$M_e = \frac{L_c}{d_m} \quad (\text{E4.5})$$

$$R_a = \frac{L_a}{2.667} \quad (\text{E4.6})$$

$$C_{AU} = \frac{L_a + 1.23}{0.65} \quad (\text{E4.7})$$

$$f_a = \frac{C_A}{C} = \frac{C_A}{C_A + C_S} = \frac{A_{\text{graphene}}}{A_{\text{graphene}} + A_{(\lambda)}} \quad (\text{E4.8})$$

where λ is the wavelength of Cu K α radiation and θ is the Bragg angle, ω is the full width of the peaks at half maximum. In addition, A is the area under the respective peak. C is the number of total carbon atoms per structural units, C_A and C_S show the number of aromatics and saturates per structural unit, respectively.

Table 4.1 reports the values for the parameters calculated from Equations E4.1 to E4.8 and provides a comparison with literature findings. Average values of the parameters in addition to other statistical parameters are used to compare current results. As can be seen in Table 4.1, the distance between the saturated portions of the asphaltenes nanocluster (d_r) is 4.5 Å, while the layer distance between the aromatic sheets (d_m) is 3.6 Å. The value of d_m for the asphaltenes nanoclusters is higher than that of the perfect graphite structure, which is 3.4 Å (Hosseinpour et al., 2013). This value confirms the steric hindrance produced by the circumferential substituents of the asphaltenes aromatic sheets in the stacked clusters (Hosseinpour et al., 2013). The average diameter of the aromatic sheets (L_a) was 18.0 Å and the average height of the cluster of the aromatic sheets perpendicular to the plane of the sheets (L_c) was 16.2 Å. The number of aromatic sheets in a stacked cluster (M_e) was 4.6 on average. It should be noted that sometimes M_e is calculated using $M_e = L_c/d_m + 1$ (Siddiqui, Ali, & Shirokoff, 2002), but for this work, $M_e = L_c/d_m$ was used for the number of aromatic sheets in a stacked cluster. The average number of aromatic rings in each aromatic sheet (R_a) and the number of carbons per aromatic structural unit (CAU) were 6.8 and 29.6, respectively. The aromaticity index, f_a , capturing the ratio of the carbon atoms present in the aromatic rings to the total carbon atoms in the asphaltenes was 0.35, which suggests a low proportion of aromatic structures.

The structural parameters of the asphaltenes extracted from this study were compared with parameters obtained from the literature for 45 asphaltenes (Andersen et al., 2005; Bouhadda, Bendedouch, Sheu, & Krallafa, 2000; Bouhadda, Bormann, Sheu, & Bendedouch, 2007; Eyssautier et al., 2011; Groenzin & Mullins, 2000, 2000; Hosseinpour et al., 2013; Liu & Li, 2015; Mang, Liu, & Liang, 1989; Sadeghi, Chilingarian, & Yen, 1986; Schwager et al., 1983; Shirokoff

et al., 1997; Siddiqui et al., 2002; Tanaka et al., 2003a; Teh Fu. Yen et al., 1961), as listed in Table 4.1. Eight parameters can be obtained from XRD analysis; however, in most of the existing literature only four or five parameters were reported. Therefore, the missing parameters were calculated in this study. Two formulas have been proposed to measure the number of aromatic sheets in a stacked cluster (M_e) (Siddiqui et al., 2002; Yen et al., 1961). Eq. E4.5 was used for all the asphaltenes to ensure consistency of the results. In addition, the average number of aromatic rings in each aromatic sheet (R_a) and the number of carbons per aromatic structural unit (C_{AU}) were not calculated in many studies. For this work, these two parameters were calculated/recalculated for all asphaltenes based on Eqs. E4.6 and E4.7, respectively. The aromaticity index (f_a) of 35 asphaltenes from the total 45 asphaltenes has been reported in literature. All of these structural parameters are included in Table 4.1. A detailed statistical analysis was conducted on the data and the mean, median, mode, standard deviation (SD), skewness, kurtosis, minimum and maximum were calculated, and their corresponding values were reported in Table 4.1. Equations 4.9 to 4.12 are expressions showing the mean, the standard deviation, the skewness and kurtosis calculations.

$$\text{Mean} = (\sum x_1/n) \quad (\text{E4.9})$$

$$\text{SD} = \sqrt{(\sum |x_1 - \bar{x}|^2/n-1)} \quad (\text{E4.10})$$

$$\text{Kurtosis} = \sum_{i=1}^n (x_1 - \bar{x})/n/s^4 \quad (\text{E4.11})$$

$$\text{Skewness} = \sum (x_1 - \bar{x})^3 / (n - 1)s^3 \quad (\text{E4.12})$$

where x_1 is the value of a given parameter, $n=45$ is the number of asphaltene samples, \bar{x} = mean of the data set and s is the standard deviation. Skewness and kurtosis help to understand how the data points are distributed between the maximum and the minimum of a data bank. As can be seen from Table 4.1, the structural parameters of the asphaltenes used in this study are within the range of the literature data. In addition, the layer distance between aromatic sheets of all the asphaltenes is close to 3.55 Å, while the distance between the saturated portions of the asphaltenes, d_r , is 4.82 Å. The literature values on the average diameter of the aromatic sheets, L_a , and the

average height of the cluster of aromatic sheets perpendicular to the plane of the sheets, L_c , cover a wide range from 7.00 Å to 18.10 Å and from 10.60 Å to 36.00 Å, respectively. In addition, literature values on M_e , R_a , C_{AU} , and f_a of different asphaltenes varied a lot. Another interesting point is that, the five asphaltenes extracted from coal have almost the same values for d_r and d_m compared to the other asphaltenes, while their L_c , L_a , M_e , R_a , and C_{AU} are lower than the asphaltenes extracted from oil (Schwager et al., 1983). These observations are in good agreement with those made by Groenzin and Mullins (Groenzin & Mullins, 2000) using fluorescence depolarization measurements. The average number of aromatic rings per aromatic sheet for the asphaltenes extracted in this work is 5.56, which is in good agreement with the literature, from 4 to 10 fused rings (Bouhadda et al., 2000).

In addition, literature NMR results also demonstrated that the average number of rings in a fused ring system is around 7 (Calemma, Iwanski, Nali, Scotti, & Montanari, 1995), which is close to the XRD results from this study. The average diameter of the asphaltenes polycyclic aromatic sheet, L_c , calculated in this work is in line with the results obtained by different techniques. Groenzin and Mullins (Tanaka et al., 2003b) obtained asphaltenes molecule size between 10.0 and 20.0 Å, which is close to the value obtained in this study. Also, Sato and Takanohashi (Tanaka et al., 2003b) found the size of asphaltenes to be about 25 Å using small-angle neutron scattering (SANS). The small angle neutron and X-ray scattering (SANS, SAXS) measurements revealed that the nanoclusters of asphaltenes are best described using a disk of total radius of 32 Å and a height of 6.7 Å with 30% polydispersity (Eyssautier et al., 2011).

In addition, the diffusion coefficient of asphaltenes in toluene has been determined by several techniques and values between 1×10^{-10} m²/s and 4×10^{-10} m²/s were reported (Abudu & Goual, 2009; Andreatta et al., 2005; Betancourt et al., 2009; Durand et al., 2009; Goual, 2009; Indo et al., 2009; Kawashima, Takanohashi, Iino, & Matsukawa, 2008; Lisitza et al., 2009; Mostowfi, Indo, Mullins, & McFarlane, 2009), which correspond to equivalent a hydrodynamic sphere radii between 10 and 36 Å (Eyssautier et al., 2011). All of the aforementioned results show that the results obtained by XRD analysis in this study are in good agreement with the literature results

using different techniques. Figure 4.2 is a schematic representation of a cross section of the asphaltene nanocluster with the relevant parameters.

Table 4.1: Aromaticity and crystalline parameters of C₇-asphaltenes nanoclusters extracted in this work based on XRD fingerprint in comparison with the literature

Ref.	Name	$d_{r, \text{Å}}$	$d_{m, \text{Å}}$	$L_c, \text{Å}$	$L_a, \text{Å}$	M_e^*	R_a^*	C_{AU}^*	f_a
This study	Athabasca vacuum residue	4.51	3.55	16.2	18	4.57	6.76	29.62	0.35
(Teh Fu. Yen et al., 1961)	Baxterville	4.7	3.57	19	10	5.32	3.75	17.28	0.53
(Teh Fu. Yen et al., 1961)	Lagunillas	4.7	3.57	17	10	4.76	3.75	17.28	0.41
(Teh Fu. Yen et al., 1961)	Burgan	4.6	3.55	19	12	5.35	4.50	20.35	0.38
(Teh Fu. Yen et al., 1961)	Wafra, No. A-1	4.6	3.57	18	12	5.04	4.50	20.35	0.37
(Teh Fu. Yen et al., 1961)	Mara	4.7	3.57	18	16	5.04	6.00	26.51	0.35
(Teh Fu. Yen et al., 1961)	Wafra. No. 17	4.8	3.57	19	14	5.32	5.25	23.43	0.35
(Teh Fu. Yen et al., 1961)	Raoudtain	4.6	3.60	18	13	5.00	4.87	21.89	0.32
(Teh Fu. Yen et al., 1961)	Ragusa	4.8	3.60	19	12	5.28	4.50	20.35	0.26
(Schwager et al., 1983)	Synthoil	5.4	3.7	12.2	10.3	3.30	3.86	17.74	-
(Schwager et al., 1983)	HRI H-Coal	4.4	3.6	13.6	8.2	3.78	3.07	14.51	-
(Schwager et al., 1983)	FMC-COED	4.9	3.6	10.6	8.0	2.94	3.00	14.20	-
(Schwager et al., 1983)	PAMCOSRC	5.1	3.6	12.1	10.0	3.36	3.75	17.28	-
(Schwager et al., 1983)	Cat. Inc. SRC	5.2	3.6	10.6	9.4	2.94	3.52	16.35	-
(Sadeghi et al., 1986)	-	4.55	3.57	16	-	4.48	-	-	0.52
(Mang et al., 1989)	Gudao	-	3.50	20	13.4	5.71	5.02	22.51	0.599
(Mang et al., 1989)	Shanjiasi	-	3.57	19.8	14.8	5.55	5.55	24.66	0.63
(Liu & Li, 2015)	ASP-H	4.31	3.57	21.8	12.2	6.11	4.57	20.66	-
(Liu & Li, 2015)	AP-M	4.43	3.54	22.2	17.8	6.27	6.67	29.28	-
(Liu & Li, 2015)	ASP-D	4.47	-	-	18.1	-	6.79	29.74	-
(Shirokoff et al., 1997)	Arab Heavy	4.4	3.6	24.7	12.3	6.86	4.61	20.82	0.19
(Shirokoff et al., 1997)	Arab Medium	4.5	3.6	23.2	11.9	6.44	4.46	20.20	0.16
(Shirokoff et al., 1997)	Arab Light	4.4	3.6	24.0	13.0	6.67	4.87	21.89	0.19
(Shirokoff et al., 1997)	Arab Berri	4.4	3.6	22.7	13.0	6.31	4.87	21.89	0.20
(Bouhadda et al., 2000)	Hassi Messaoud	-	3.56	16.5	9.5	4.63	3.56	16.51	0.40
(Siddiqui et al., 2002)	RT-F	6.2	3.7	14.3	9.9	3.86	3.71	17.12	0.16
(Siddiqui et al., 2002)	RT-R1	5.9	3.6	20.1	7.0	5.58	2.62	12.66	0.12
(Siddiqui et al., 2002)	RT-R4	4.5	3.5	20.8	9.1	5.94	3.41	15.89	0.14
(Siddiqui et al., 2002)	RT-P1	4.5	3.5	20.2	9.5	5.77	3.56	16.51	0.16

(Siddiqui et al., 2002)	RT-P2	4.5	3.5	20.3	8.2	5.80	3.07	14.51	0.13
(Siddiqui et al., 2002)	KW-F	5.6	3.5	25.2	11.0	7.20	4.12	18.82	0.18
(Siddiqui et al., 2002)	KW-R1	5.6	3.5	24	14.5	6.86	5.44	24.20	0.17
(Siddiqui et al., 2002)	KW-R4	5.7	3.5	23.1	12	6.60	4.50	20.35	0.14
(Siddiqui et al., 2002)	KW-P1	6.1	3.5	27.6	12.9	7.89	4.84	21.74	0.05
(Siddiqui et al., 2002)	KW-P4	5.9	3.6	22.4	13.7	6.22	5.14	22.97	0.09
(Andersen et al., 2005)	Asph 1 F	4.28	3.51	31	14	8.83	5.25	23.43	0.19
(Andersen et al., 2005)	Asph 2	4.87	3.48	16	12	4.60	4.50	20.35	0.29
(Andersen et al., 2005)	Asph 3	4.33	3.53	33	11	9.35	4.12	18.82	0.08
(Andersen et al., 2005)	Asph 4	4.31	3.49	36	11	10.32	4.12	18.82	0.23
(Bouhadda et al., 2007)	Hassi Messaoud	4.35	3.56	28.24	17.6	7.93	6.59	28.94	-
(Hosseinpour et al., 2013)	Iranian	-	3.5	29.4	12.9	8.40	4.84	21.74	-
(Liu & Li, 2015)	AR-F-ASP	4.39	3.81	26.29	13.04	6.90	4.89	21.95	-
(Liu & Li, 2015)	AR-P-ASP	4.53	3.56	19.51	10.43	5.48	3.91	17.94	-
(Liu & Li, 2015)	ARLCO-P-ASP	4.63	3.70	18.13	9.23	4.90	3.46	16.09	-
(Majid Mohammadi, Dadvar, & Dabir, 2017)	Asphaltene A	-	-	-	-	-	-	-	0.33
(Majid Mohammadi et al., 2017)	Asphaltene B	-	-	-	-	-	-	-	0.25
	Mean	4.82	3.57	20.67	12.04	5.80	4.52	20.42	0.27
	Median	4.60	3.57	20.00	12.00	5.58	4.50	20.35	0.23
	Mode	4.40	3.60	19.00	12.00	5.32	4.50	20.35	0.35
	SD	0.55	0.07	5.70	2.75	1.64	1.03	4.23	0.15
	Kurtosis	0.44	3.21	0.43	0.03	0.58	0.03	0.03	-0.01
	Skewness	1.29	1.39	0.55	0.56	0.59	0.56	0.56	0.80
	Minimum	4.28	3.48	10.60	7.00	2.94	2.62	12.66	0.05
	Maximum	6.20	3.81	36.00	18.10	10.32	6.79	29.74	0.63

*Recalculated/calculate based on the equations 4.5 to 4.7 above.

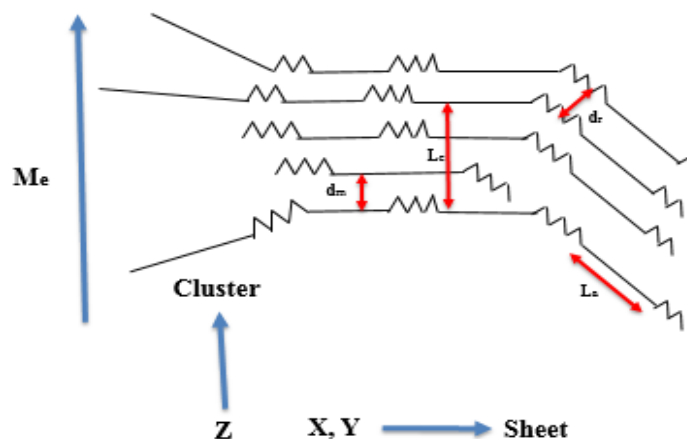




Figure 4.2: A schematic representation of a cross section of asphaltenes nanoclusters.

“” stands for alkyl chains or naphthenic rings, and “” stands for the flat sheets of aromatic rings.

Although XRD and elemental analysis are proper techniques for determining the composition and structure of asphaltenes, they do not provide information on the functional groups existing in asphaltenes. In order to identify major functional groups present in the C7-asphaltenes extracted in this study, FTIR was used. Figure 4.3 shows the FTIR spectrum of the asphaltenes, while Table 4.2 lists the observed peaks and the corresponding functional groups (Alhumaidan, Hauser, Rana, & Lababidi, 2016; Asemani & Rabbani, 2016; Dordević et al., 2012; Hosseinpour et al., 2014; Martinez, Miranda, & Juan, 1988; Masson, Pelletier, & Collins, 2001; Nivitha, Prasad, & Krishnan, 2016; Sánchez-Lemus et al., 2016; James G. Speight, 1972; Wilt, Welch, & Rankin, 1998b; Xu, Yu, Tesso, Dowell, & Wang, 2013; Zhang, Zheng, & Wang, 2016; Zhao & Shaw, 2007). The FTIR finger print is identical to that of other asphaltenes in literature (Buenrostro-Gonzalez, Andersen, Garcia-Martinez, & Lira-Galeana, 2002; Calemme et al., 1995; Christy, Dahl, & Kvalheim, 1989). The spectrum shows a sharp peak at 2923 cm^{-1} indicative of C-H stretching, with some portion of aromatic structure.

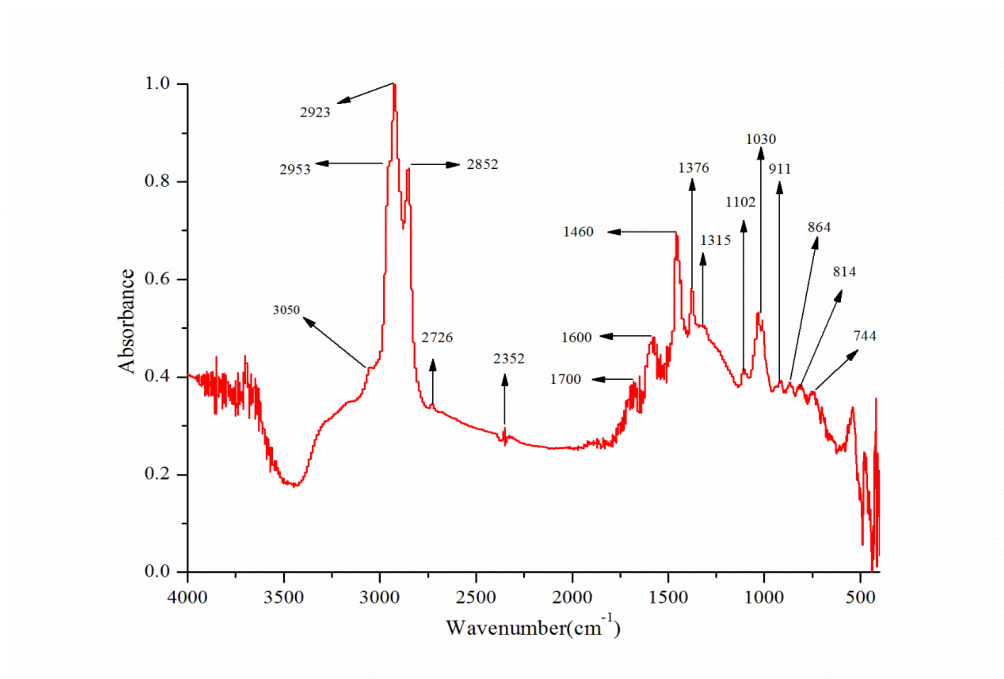


Figure 4.3: FTIR spectrum of virgin C7-asphaltenes extracted in this study.

Table 4.2: FTIR band assignment of virgin C7-asphaltenes extracted in this study

Wavenumber (cm ¹)	Functional group
3050	Aromatic C-H stretching vibration
2953	Asymmetrical stretching of C-H bond in CH ₃
2923	Asymmetrical stretching of C-H bond in CH ₂
2852	Asymmetrical stretching of C-H bond in CH ₂
2726	Stretching of C-H bond in aldehyde hydrogen
2352	CO ₂ species in atmosphere
1700	Stretching in aromatic double bond, C=O in aryl ketone
1600	Stretching of C=C bond in aromatic rings
1460	Symmetrical bending of C-H in CH ₂ , asymmetrical bending of C-H in CH ₃ , asymmetrical stretching of C=C bond in aromatic rings
1315	C-N Symmetric stretching vibration
1030	Stretching of S=O bond in sulfoxides
911	Out of plane wagging of C-H in terminal alkane
864, 814, 744 and 724	Out of plane bending of C-H bond in aromatic ring structure.

(Alhumaidan et al., 2016; Asemanni & Rabbani, 2016; Czarnecka & Gillott, 1980; Dordević et al., 2012; Hosseinpour et al., 2014; Martinez et al., 1988; Masson et al., 2001; Nivitha et al., 2016; Sánchez-Lemus et al., 2016; James G. Speight, 1972; Wilt et al., 1998b; Xu et al., 2013; Zhang et al., 2016; Zhao & Shaw, 2007)

4.2 Characterization of Asphaltenes in Model Solution

Figure 4.4 depicts the DLS estimation of the mean hydraulic diameter of the asphaltene aggregates in model solutions for a concentration range of 200 ppm to 10,000 ppm. The average aggregate size ranged from about 100 ± 60 nm to 210 ± 40 nm, with no correlation to concentration. These aggregate sizes differ from the average of 5-20 nm reported in previous studies (Mansur, De Melo, & Lucas, 2012; Yarranton et al., 2013). This could be as a result of the higher concentration range used in this study and the absence of nanofiltration. Literature also suggests that asphaltene aggregates are not known to increase in size, rather they flocculate as concentration becomes very high (≥ 8 wt %) (Durand et al., 2010; Sheu, 2006). The high error bars associated with the measurements should nevertheless be noted. DLS instrument averages about 22 readings collected over 10 min, which may suggest a wide size aggregate distribution. The refractive index (RI) measurements in Figure 4.5, on the other hand, show constant RI, which suggests that the asphaltenes are almost at same state of nanoaggregation, in-dependent of concentration (Evdokimov, Eliseev, & Akhmetov, 2003; Evdokimov & Losev, 2007).

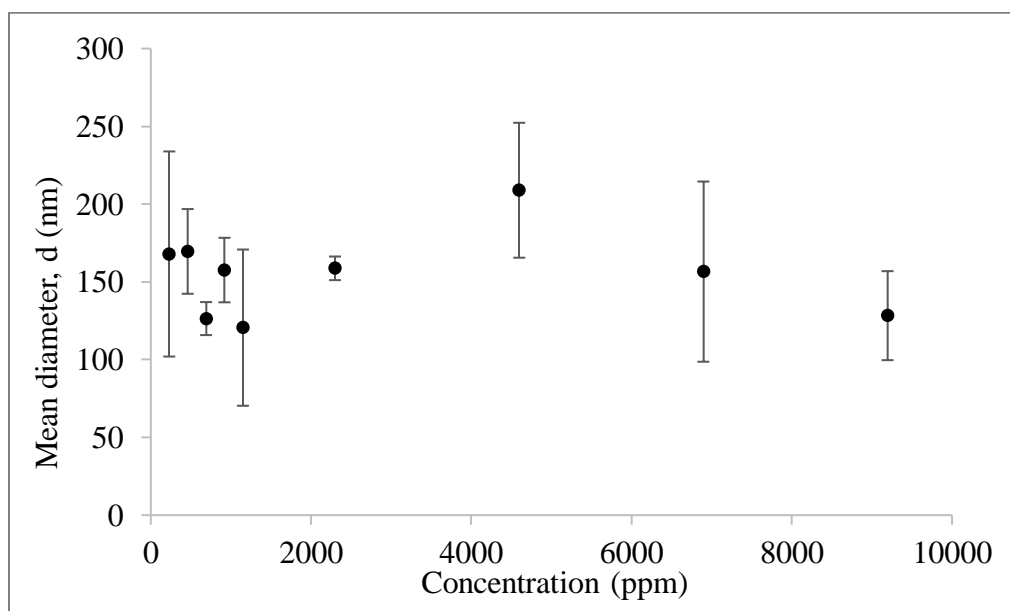


Figure 4.4: DLS mean diameter of asphaltene nanoaggregates in the toluene model solutions as a function of concentration.

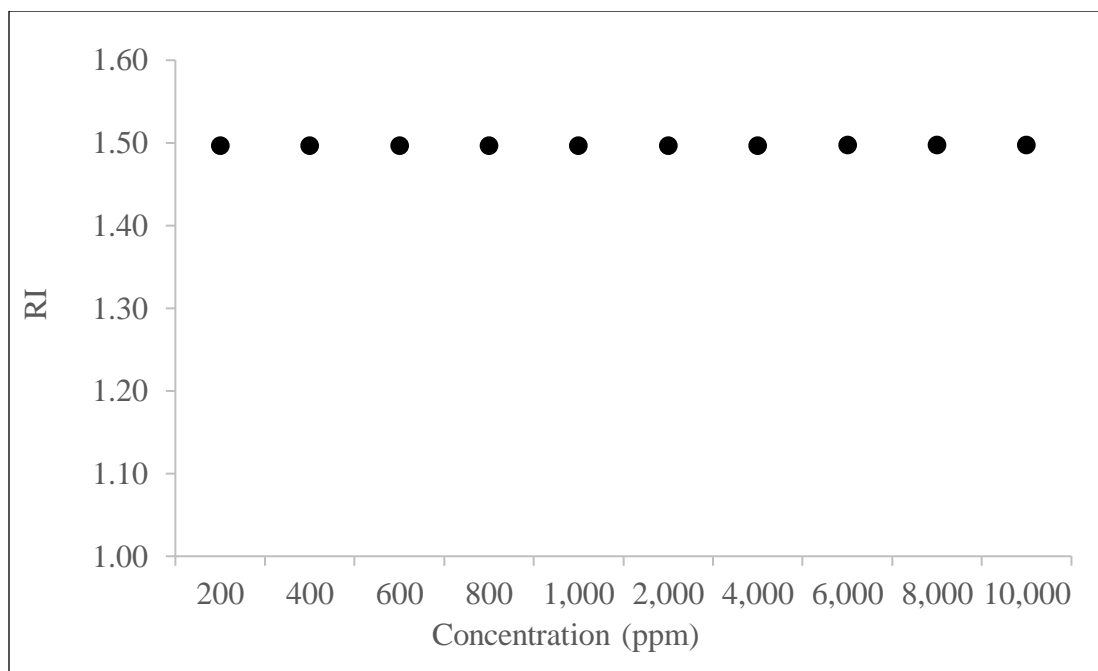


Figure 4.5: Refractive index measure of asphaltenes nanoaggregates in the toluene model solution.

4.3 NP characterization

Table 4.3 lists the average particle size estimated based on different instruments, and pore volume estimated by TriStar instrument. Per TriStar estimates, Al_2O_3 NPs showed the highest surface area and pore volume, followed by Fe_3O_4 and Fe_2O_3 . It is highly likely that pore volume arises from NP aggregates, rather than porous individual NPs, especially given the very low specific pore size compared with the specific surface area. Representative TEM photographs and XRD pattern of the as received NPs, following washing with toluene are shown in Figure 4.6. Al_2O_3 displayed rod-shaped particles with an average length of 27 ± 1 nm. On the other hand, Fe_2O_3 and Fe_3O_4 showed mainly spherically shaped particles with average diameters of 29 ± 4 nm and 21 ± 2 nm, respectively. The XRD pattern shows NPs with very small crystalline domain sizes as can be seen from the broadening of the peaks. Using Scherrer's equation (Monshi, Foroughi, & Monshi, 2012), average crystal sizes of 5 ± 2 nm, 30 ± 4 nm and 24 ± 1 nm were obtained for Al_2O_3 , Fe_2O_3 and Fe_3O_4 , respectively. The similarity between the mean particle size and crystal size for Fe_2O_3 and Fe_3O_4 suggests that these particles are in fact nanocrystals. The average particle size and crystal size obtained by TEM and XRD were taken as the average diameter of an equivalent sphere to

calculate the corresponding surface area using the bulk density of the particles. The surface areas obtained by XRD and TEM are in good agreement with those obtained by BET equation for Fe_2O_3 and Fe_3O_4 , whereas they differed for Al_2O_3 , due to its non-spherical morphology. When the surface area of Al_2O_3 was calculated from TEM images assuming a cylindrical shape with a diameter of 7 nm and a length of 27 nm, surface area was $163 \text{ m}^2/\text{g}$ which is in good agreement with BET results. Other small peaks were noted in the XRD pattern in Figure 4.6, however, this may have been as a result of impurities in the nanoparticles.

Table 4.3: TriStar pore volume and surface area estimates and average NP size obtained from XRD and TEM and the corresponding surface area.

NP	TriStar		XRD		TEM	
	Pore Volume, BJH estimate (cm^3/g)	Surface area, BET estimate (m^2/g)	Average crystal size* (nm)	Corresponding surface area (m^2/g)	Average particle size (nm)	Corresponding surface area (m^2/g)
Al_2O_3	1.01	156	5	330^{**}	27 ± 1	55^{**} 163^{***}
Fe_2O_3	0.12	37	30	38^{**}	29 ± 4	39^{**}
Fe_3O_4	0.26	43	24	48^{**}	21 ± 2	55^{**}

*Estimated from Scherrer equation (Monshi et al., 2012)

** Assuming spherical shape and bulk density

*** Assuming cylindrical shape and bulk density

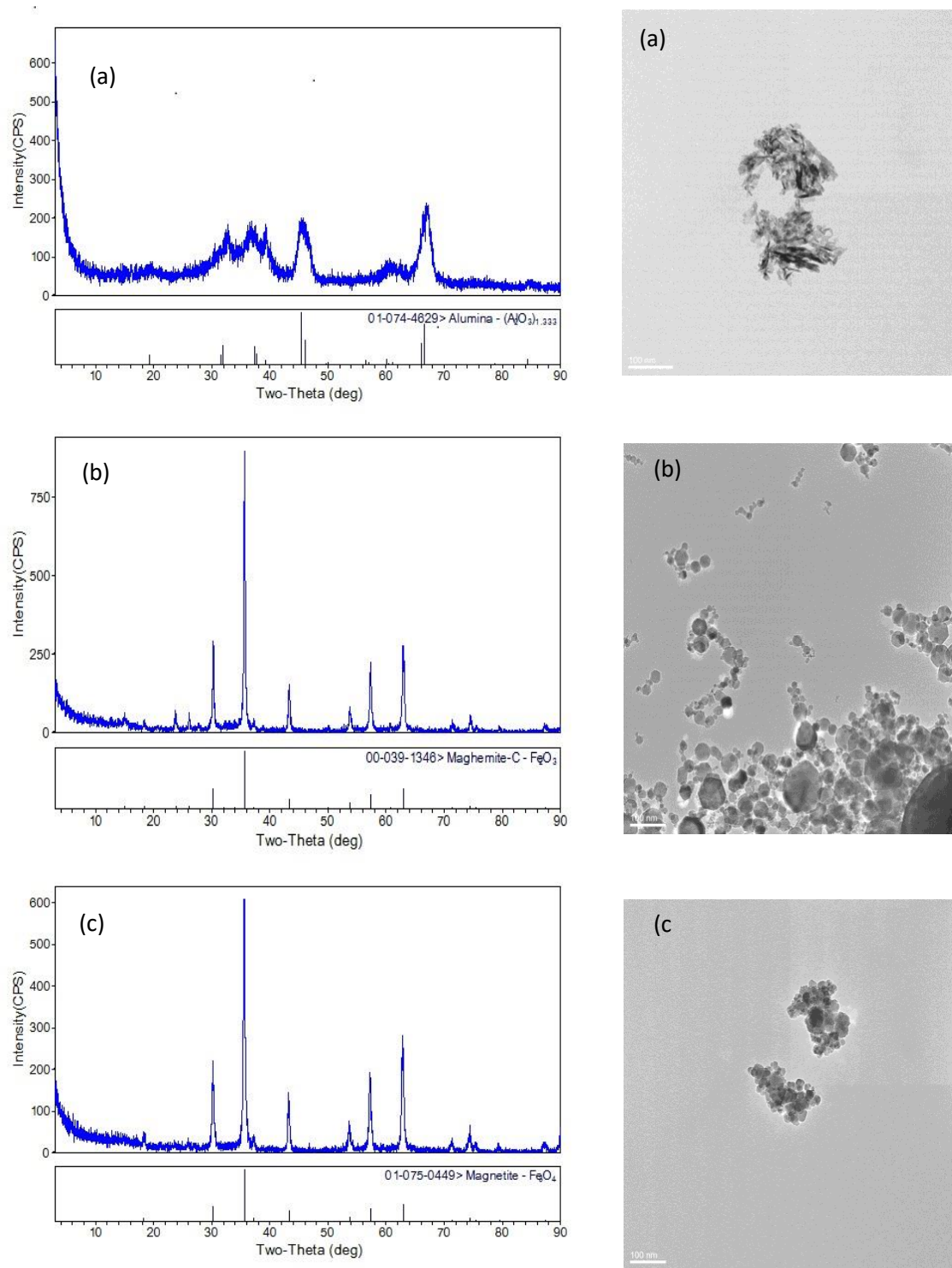


Figure 4.6: XRD and TEM images of the as received (a) Al_2O_3 (b) Fe_2O_3 (c) Fe_3O_4 following washing with toluene.

4.4 Adsorption Isotherms

Figure 4.7 and Figure 4.8 compare the experimental uptake results calculated from the different UV-Vis wavelengths and TGA results with Langmuir and Freundlich isotherm models, using Eqs. 2.1 and 2.2, respectively. The model parameters summarized in Table 4.4 were obtained by minimizing the average square deviations between the experimental data and the model. The mean squared error and the coefficient of determination, R^2 , suggests that the data are better fit by Langmuir model, which entails monolayer adsorption (Mohammadi, Khamehchi, & Sedighi, 2014; Mohammadi & Sedighi, 2013; Mohammadi, Sedighi, Hashemi Kiasari, & Hosseini, 2015b). It should be noted that values of the coefficient of determination, R^2 , are very low for the Freundlich isotherm fitting, as opposed to Langmuir fit, which was always high, > 0.96 . Accordingly, Langmuir isotherm was assumed.

Table 4.4: Langmuir and Freundlich parameters and the corresponding R^2 values obtained by fitting the models to UV-Vis and TGA-calculated uptake.

NP		Langmuir			Freundlich		
		q_{max} (mg/m ²)	K_L (kg/mg)	R^2	n	K_F (mg ^{1-(1/n)} kg ^{1/n} g ⁻¹)	R^2
Al ₂ O ₃	410 (nm)	1.4	0.0054	0.99	0.15	0.30	0.24
	550 (nm)	1.8	0.0060	1.0	0.19	0.29	0.46
	700 (nm)	2.4	0.0040	0.97	0.22	0.30	0.65
	TGA	1.7	0.0022	0.99	0.64	0.0052	0.91
Fe ₂ O ₃	410 (nm)	1.7	0.0223	0.99	0.12	0.56	0.45
	550 (nm)	2.1	0.0264	1.0	0.15	0.59	0.61
	700 (nm)	2.7	0.0066	0.99	0.17	0.58	0.70
	TGA	2.6	0.0061	1.0	0.12	0.75	0.68
Fe ₃ O ₄	410 (nm)	1.7	0.0032	1.0	0.11	0.50	0.40
	550 (nm)	2.2	0.0023	0.98	0.14	0.50	0.57
	700 (nm)	2.9	0.0017	0.963	0.17	0.47	0.66
	TGA	2.1	0.0056	1.0	0.08	0.94	0.96

Interestingly, the different wavelengths contributed to different Langmuir coefficients with an increasing value of q_{max} at higher wavelengths, whereas K_L varied independently. For the different NPs, the TGA measurements seem to correlate with a particular wavelength. For the Al₂O₃ particles, the TGA measurements were in line with the UV measurements at 410 nm for all the concentration ranges. However, Fe₂O₃ and Fe₃O₄ showed a different trend. At lower concentration, Fe₂O₃ TGA data fell along the 410 nm, while Fe₃O₄ TGA data was in line with 700 nm. As the

concentration increased, Fe₂O₃ TGA data fell within the 700 nm, while Fe₃O₄ TGA data were close to 550 nm data. This is probably due to orientation and selective adsorption of the different functional groups on different asphaltenes sub fractions at the different wavelengths.

At the different wavelengths, the NPs showed varying degrees of adsorption capacity (q_{max}) of the asphaltenes per unit surface area of the particles. At 410 nm, Fe₂O₃ showed the highest adsorption capacity (q_{max}) of 1.68 mg/m², followed by Fe₃O₄ and Al₂O₃. At 550 and 700 nm, Fe₃O₄ displayed highest adsorption capacities of 2.18 (mg/m²) and 2.91 (mg/m²), respectively, followed by Fe₂O₃. Al₂O₃ showed the least adsorption capacity with $q_{max} = 1.84$ mg/m² at 550 nm and $q_{max} = 2.43$ (mg/m²) at 700 nm. A different trend was observed for the adsorption capacity in mg/g. Al₂O₃ showed the highest adsorption capacity of 385 mg/g, followed by Fe₃O₄ and Fe₂O₃ (125 and 102 mg/g, respectively) at 700 nm. The experimental uptake results attained at different wavelengths with Langmuir and Freundlich isotherm models based on (mg/g) are plotted in Figure 4.9 and Figure 4.10. The high adsorption capacity of Al₂O₃ per g is attributed to the high surface area/g of this NP, which may make it more economical compared to the other NPs. For the Langmuir equilibrium adsorption constant (K_L), the following order was observed for all three wavelengths Fe₂O₃ > Al₂O₃ > Fe₃O₄, whereas for the TGA results, the order was Fe₂O₃ > Fe₃O₄ > Al₂O₃. The inset in Figure 4.7b shows a crossing of the adsorption isotherm. Per above discussion, this intersection should not to have physical significance.

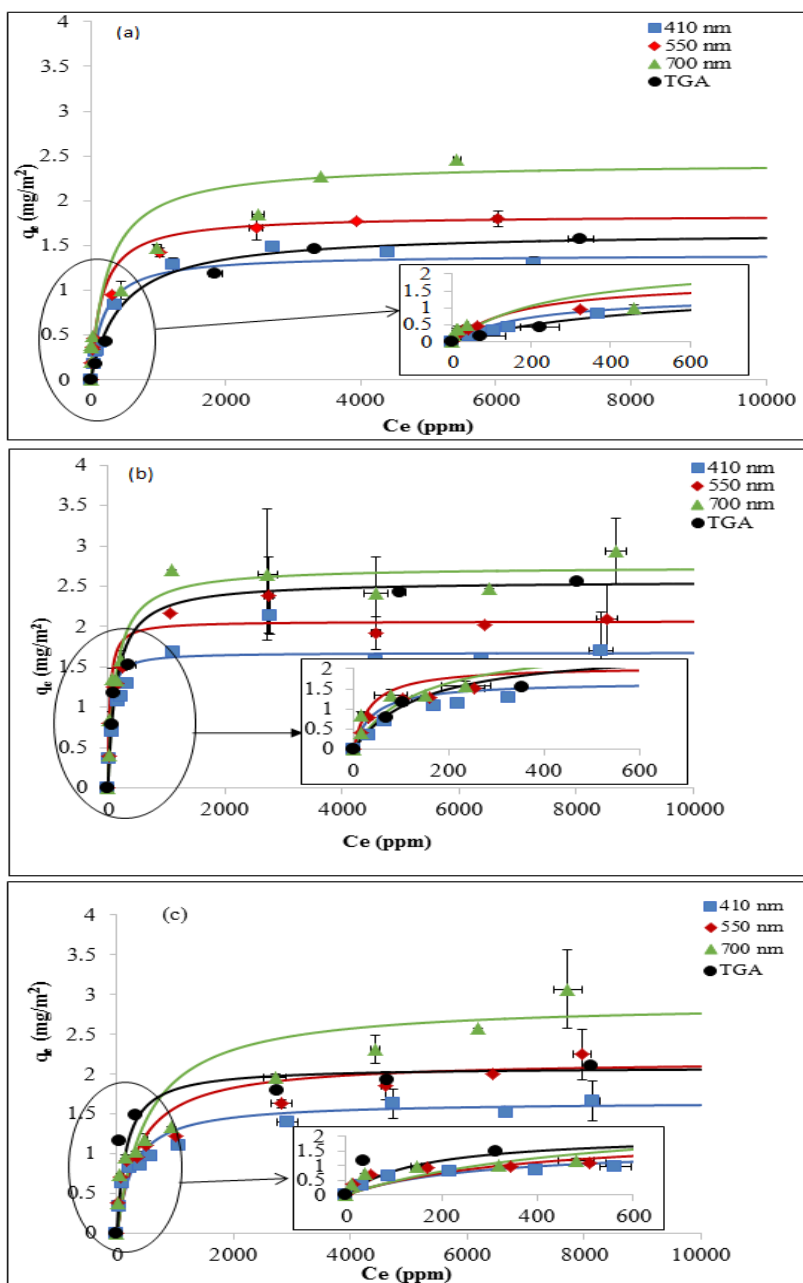


Figure 4.7: Adsorption isotherms of asphaltenes onto (a) Al_2O_3 (b) Fe_2O_3 (c) Fe_3O_4 . Points: experimental; Lines: Langmuir model fitted to UV-Vis measurements at 3 different wavelengths and TGA results.

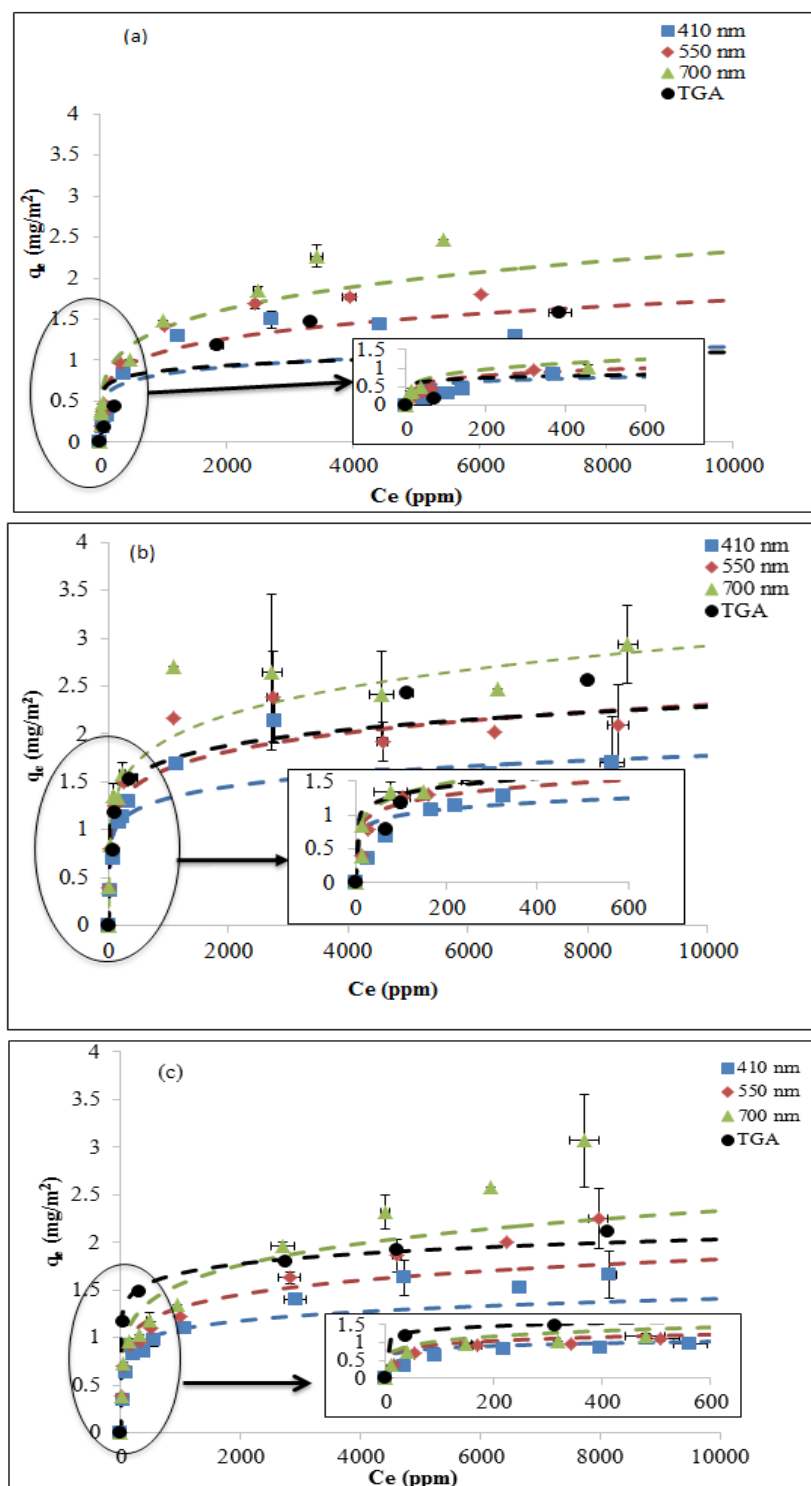


Figure 4.8: Adsorption isotherm of asphaltenes onto (a) Al_2O_3 (b) Fe_2O_3 (c) Fe_3O_4 showing the Freundlich model with q_e in mg/m^2 . The symbols are UV-Vis experimental data and TGA result in mg/m^2 .

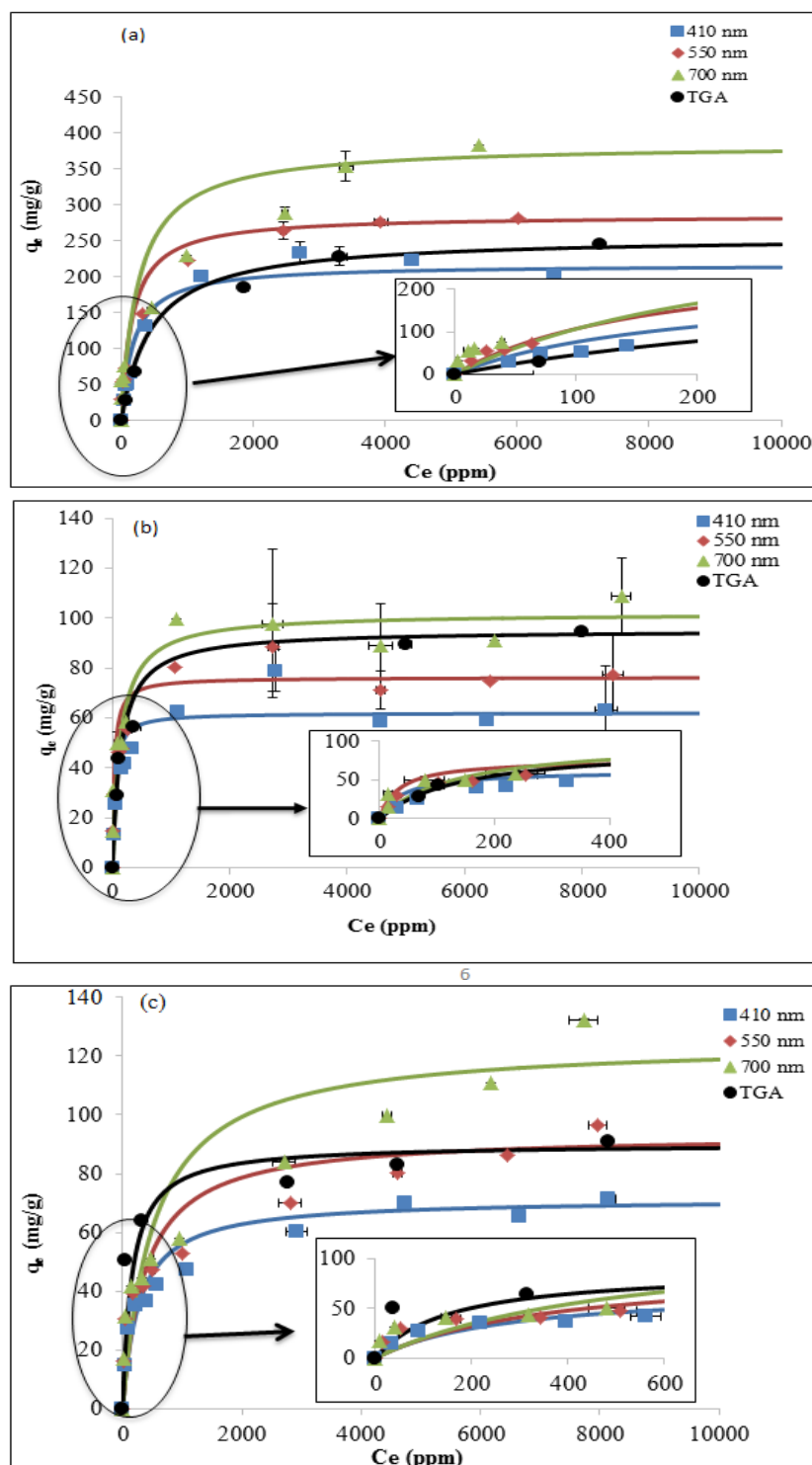


Figure 4.9: Adsorption isotherm of asphaltenes onto (a) Al_2O_3 (b) Fe_2O_3 (c) Fe_3O_4 showing the Langmuir model (E2.1), with q_e in mg/g. The symbols are UV-Vis experimental data and TGA result in mg/g., the solid lines are the best fit of the Langmuir model.

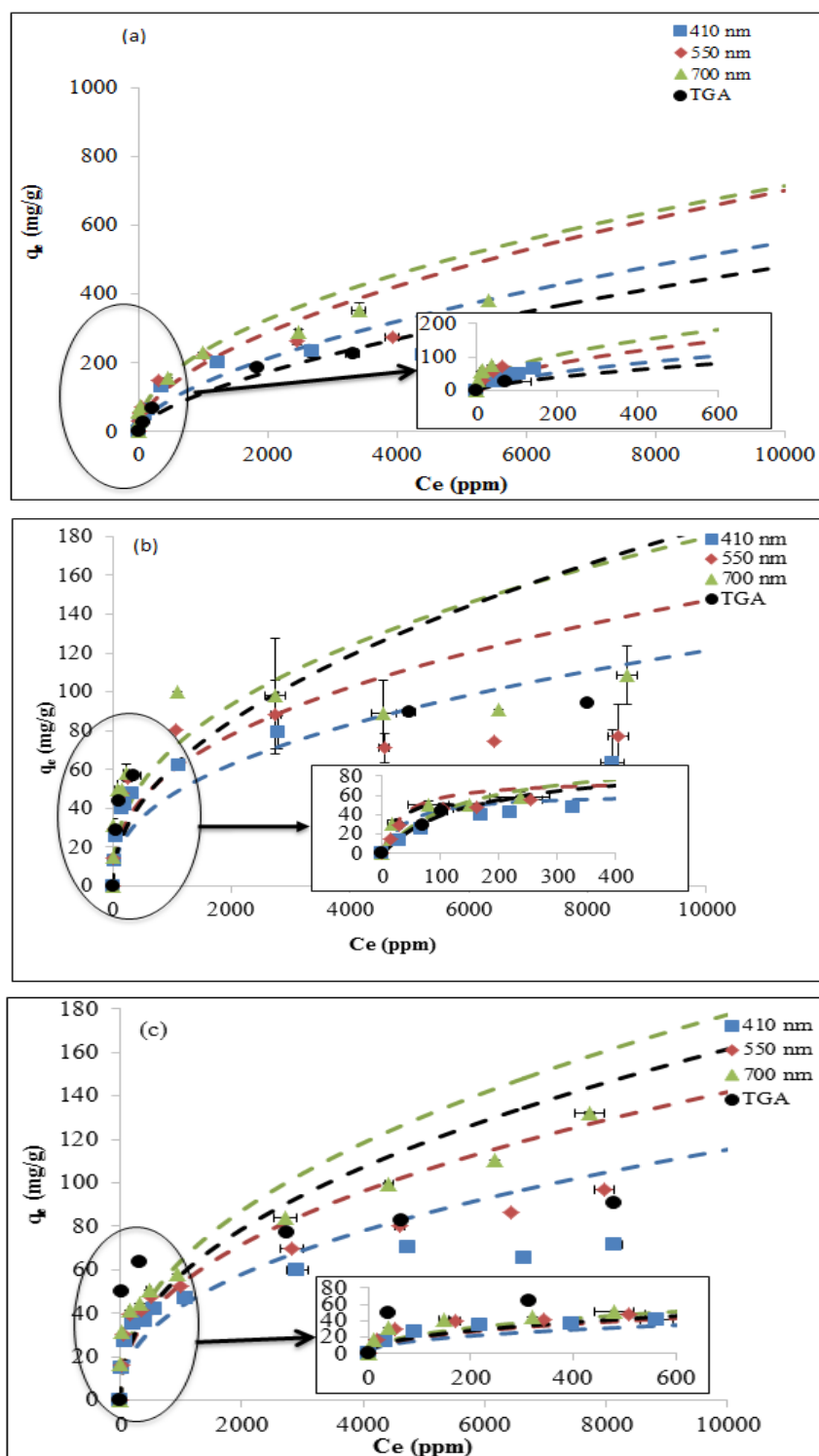


Figure 4.10: Adsorption isotherm of asphaltenes onto (a) Al_2O_3 (b) Fe_2O_3 (c) Fe_3O_4 showing the Freundlich model (E2.2), with q_e in mg/g. The symbols are UV-Vis experimental data and TGA result in mg/g.

Asphaltenes adsorb onto solid surfaces in the form of colloidal aggregates, micelles, dimers or monomers (Hosseinpour et al., 2013). According to the DLS measurements of Figure 4.4, asphaltenes exist as nanoaggregates having average hydraulic diameters of 150 ± 50 nm independent of asphaltenes concentration. If the adsorption equilibrium were established between nanoaggregates in the solution and nanoaggregates adsorbed to the surface of the NPs, this would have led to much higher uptake values; in the order of 1000 mg/g assuming equal exposure to the surface and asphaltenes density of 1.2 g/mL (David Ting, Hirasaki, & Chapman, 2003; Park, Kittelson, Zachariah, & McMurry, 2004). The fact that the values of q_{max} were much less and the Langmuir model provided a better fit, suggests that equilibrium of asphaltenes monomers, dimers and/or trimers among three pseudo phases: the bulk toluene, the surface of the NPs and the asphaltenes aggregates was most likely established.

Even though many literature investigations reported Langmuir-type adsorption of C7-asphaltenes from toluene model solutions onto metal oxide NPs, q_{max} varied appreciably between literature reports (Hosseinpour et al., 2013; Nassar, 2010; Nassar, Hassan, & Pereira-Almao, 2011b; Shayan & Mirzayi, 2015a). This variation in part arises from the different origin, chemical structure, etc. of the asphaltenes and the chemical nature of the metal oxide NPs and their aggregation state. In addition, in light of the current investigation, this variation may arise from the different detection techniques employed; including different UV-Vis wavelength adopted. Moreover, the variation in q_{max} may have resulted from the limited range of initial, and hence equilibrium, asphaltenes concentration used in different studies (Hosseinpour et al., 2013; Nassar, 2010; Nassar, Hassan, & Pereira-Almao, 2011b; Shayan & Mirzayi, 2015a). To test this hypothesis, we fitted the Langmuir model to equilibrium concentration $< 1,000$ ppm. Figure 4.11 and Figure 4.12 show a good fit to the Langmuir model with R^2 values in the range of 0.8 to 1.0 as shown in Table 4.5, which suggests monolayer adsorption. However, q_{max} and K_L for the fits with $C_e < 1,000$ ppm are far different from those obtained based on the wider range of up to 10,000 ppm.

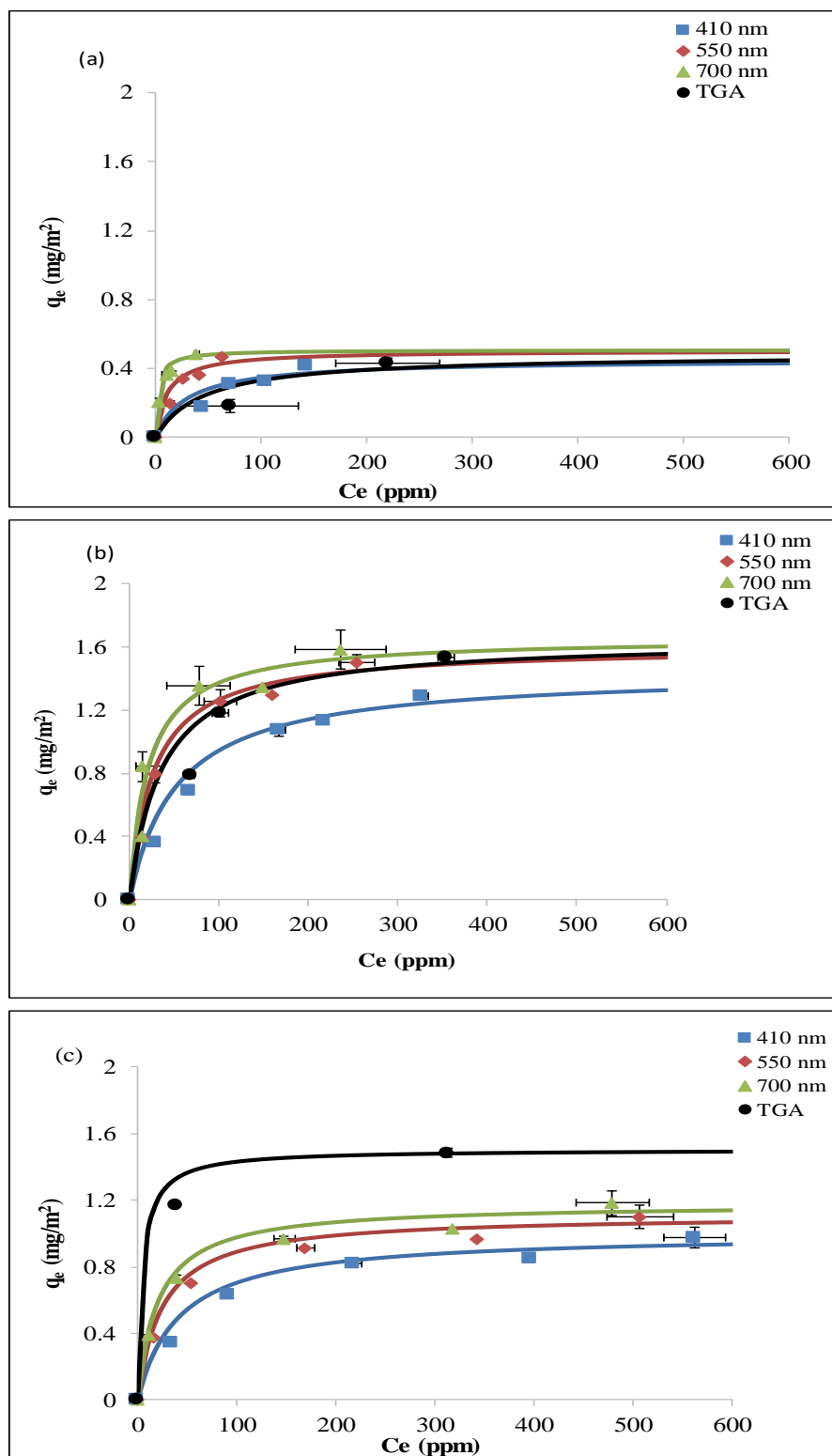


Figure 4.11: Adsorption isotherm of asphaltenes onto (a) Al_2O_3 (b) Fe_2O_3 (c) Fe_3O_4 showing the Langmuir model (E2.1), with q_e in mg/m² for the low concentrations < 1,000 ppm.

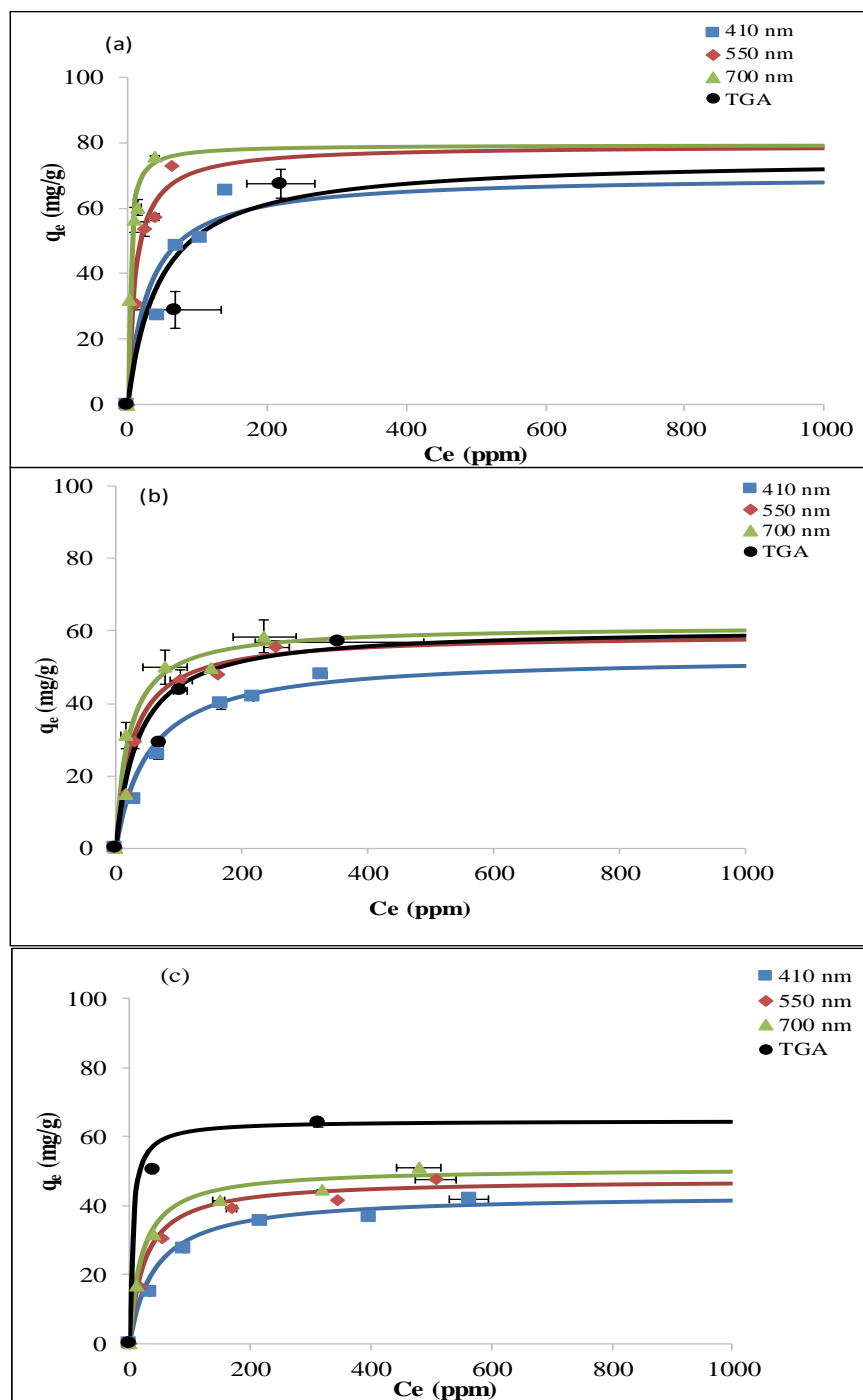


Figure 4.12: Adsorption isotherm of asphaltenes onto (a) Al_2O_3 (b) Fe_2O_3 (c) Fe_3O_4 showing the Langmuir model (E2.1), with q_e in mg/g for the low concentrations < 1,000 ppm.

Table 4.5: Langmuir parameters and the corresponding R^2 values obtained by fitting the models to UV-Vis and STA results, with q_e in mg/m^2 and mg/g for the low concentrations $< 1,000$ ppm.

NP		Langmuir			
		q_{max} (mg/m^2)	q_{max} (mg/g)	KL (kg/mg)	R^2
Al_2O_3	410 (nm)	0.45	69.93	0.033	0.80
	550 (nm)	0.51	79.37	0.09	0.89
	700 (nm)	0.51	79.37	0.35	0.98
	TGA	0.48	75.19	0.022	0.78
Fe_2O_3	410 (nm)	1.44	53.19	0.019	0.94
	550 (nm)	1.60	59.17	0.038	0.97
	700 (nm)	1.66	61.35	0.048	0.97
	TGA	1.65	60.98	0.028	0.96
Fe_3O_4	410 (nm)	1.0	43.10	0.024	0.98
	550 (nm)	1.11	47.62	0.040	0.99
	700 (nm)	1.18	50.76	0.048	0.99
	TGA	1.5	64.52	0.195	1.0

4.4.1 Characterization of the adsorbed asphaltenes

The asphaltenes adsorbed onto the NPs were characterized using FTIR in an attempt to identify functional groups attached to the surface (Abu Tarboush & Husein, 2012a) (Lante Carbognani, 2000). Figure 4.13 displays the FTIR spectra of asphaltenes adsorbed from different concentration model solutions. The FTIR spectra for bare particles are included for comparison. The spectra for adsorbed asphaltenes onto Al_2O_3 , Fe_2O_3 and Fe_3O_4 showed peaks at the following wave lengths 3541, 2956, 2929, 1662, 1556, 1376, 799, 667, 2954, 2928, 1130, 1386, 701, 641 and 562 cm^{-1} . The bands around 3541 and 2956, 2929 cm^{-1} are attributed to $-\text{OH}$, CH_3 and CH_2 stretching vibration (Belkov et al., 2012; Sides, Yarwood, & Fox, 1988; Viana, da Silva, & Pimentel, 2012) respectively, while the $\text{C}=\text{O}$ stretching and the H-N-N bending modes are observed at 1662, 1556 cm^{-1} , respectively (Hastings, Bandaranayake, & Carrion, 2008). At 1376 cm^{-1} , the symmetric CH_3 deformation is observed (Coward, 2010). The peaks between $600 - 800\text{ cm}^{-1}$ are assigned to the vibrations of Al-O bond (Yang, Liu, and Ouyang 2010; Gunasekaran et al. 2009; Saikia, Parthasarathy, and Sarmah 2009; Nikolic et al. 2014), as confirmed by a quick comparison between the control asphaltenes and Al_2O_3 NP spectra. Similarly, the band peak below 700 cm^{-1} is assigned

to Fe-O stretching mode (Farahmandjou & Soflaee, 2015; Umar et al., 2011). Lastly, the peak at 2352 cm^{-1} corresponds to atmospheric CO_2 .

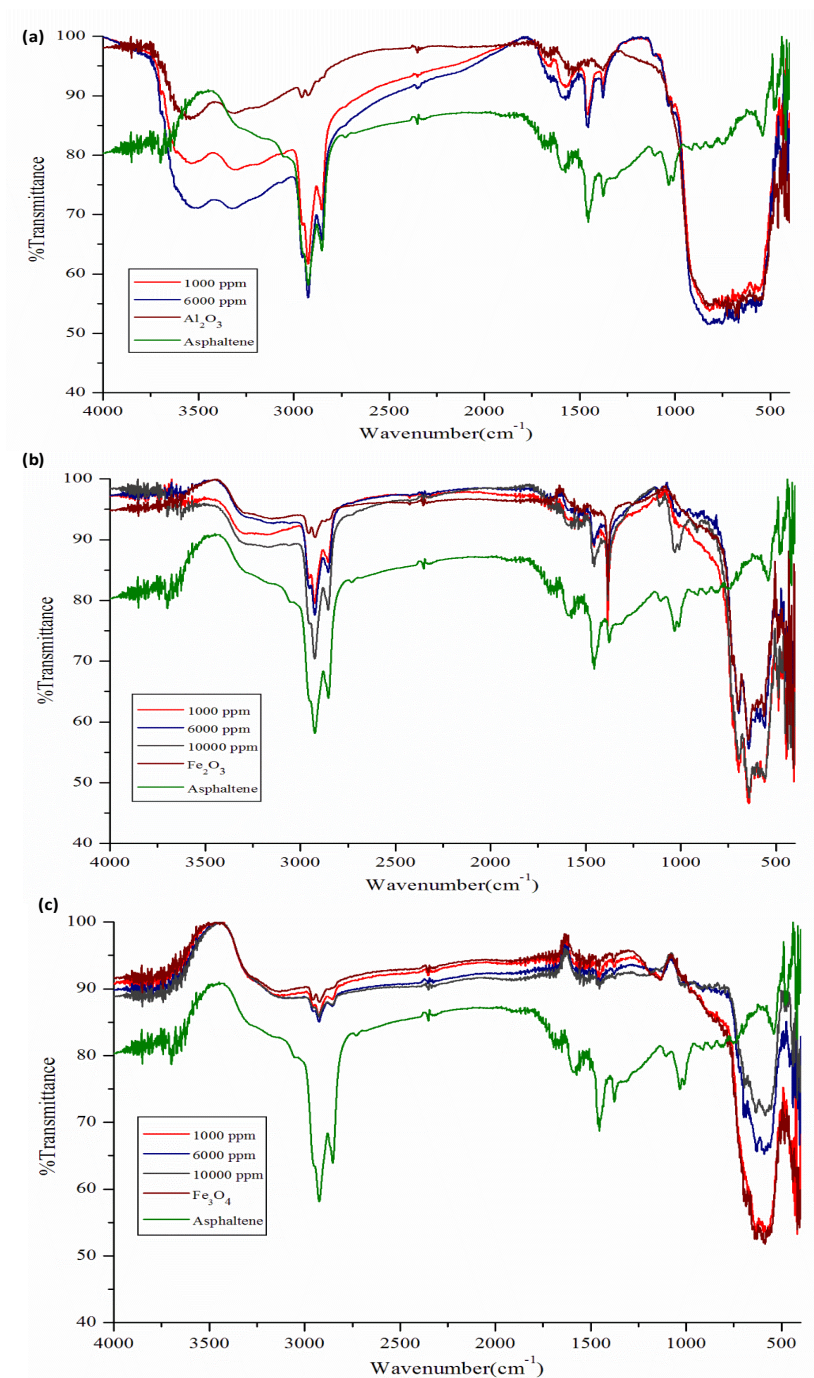


Figure 4.13: FTIR spectra of virgin and adsorbed asphaltenes onto (a) Al_2O_3 ; (b) Fe_2O_3 ; (c) Fe_3O_4 NPs. FTIR spectra for the NPs are provided for comparison.

FTIR spectra did not vary much as a function of the initial concentration of asphaltenes. It should be noted that the bands around 3000 cm^{-1} for the control NP samples might be attributed to some impurities in samples because of contaminations during sample preparation or FTIR measurement. In summary, for all of the adsorbed asphaltenes, some peaks belong to NPs, while some others belong to asphaltenes, which confirms the adsorption of asphaltene onto the metal oxide NPs. No major shift of peaks between virgin and adsorbed asphaltenes could be observed, which suggests physisorption of the asphaltenes (Sartape et al., 2017).

4.4.2 Oxidation of adsorbed asphaltenes

The thermo-oxidative profiles from TGA analysis were used to provide an insight on the role of the different NPs in promoting asphaltenes oxidation (Abu Tarboush & Husein, 2012b). The fractional conversion, α , was calculated using E4.9 (Abu Tarboush & Husein, 2012b, 2015).

$$\alpha = \frac{m_0 - m_i}{m_0 - m_\infty} \quad (\text{E4.9})$$

where, m_0 is the initial mass of the adsorbed asphaltenes and NP sample, m_∞ is the final mass of the adsorbed asphaltene and NP sample and m_i is the mass of the adsorbed asphaltenes and NP sample at any time. In principle, fractional conversion, α , should provide an intensive variable, i.e. initial mass-independent variable in a similar fashion to concentration, for the evaluation of condensed phase reaction kinetic parameters (Flynn, 1983).

Figure 4.14 shows a plot of α versus temperature for the three NPs for different values of asphaltenes uptake. Figure 4.15 shows the % mass loss versus temperature associated with the NPs and adsorbed asphaltenes. Bare Al_2O_3 , Fe_2O_3 and Fe_3O_4 displayed a mass loss of 7%, 1% and 2%, respectively probably as result of sorbed moisture and/or other impurities. Figure 4.14 shows a major shift to lower temperatures between virgin and adsorbed asphaltenes, which is attributed to a role of the NPs in promoting asphaltenes oxidation, as suggested by the literature (Abu Tarboush & Husein, 2012a, 2012b; Nassar, Hassan, & Pereira-Almao, 2011b). Figure 4.14 on the other hand, shows that the oxidation of the adsorbed asphaltenes is mass-dependent, for all the NPs.

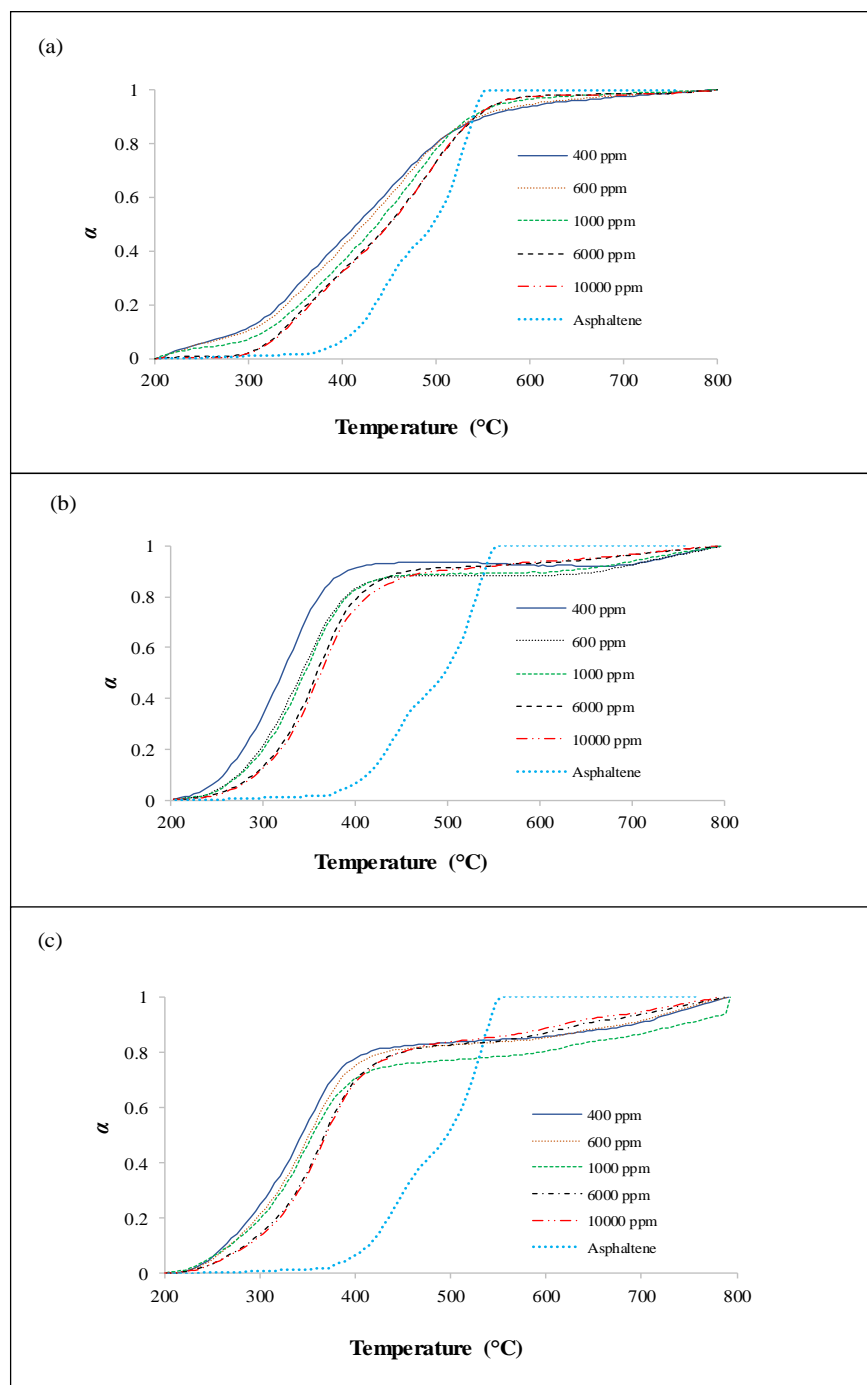


Figure 4.14: Fractional conversion, α , versus temperature for adsorbed asphaltenes onto (a) Al_2O_3 ; (b) Fe_2O_3 ; (c) Fe_3O_4 NPs

As the initial concentration of asphaltenes in the model solution increased, which corresponds to a higher uptake until q_{max} is reached, the role of the NPs in promoting the oxidation appears to

have retreated. While longer reaction times (corresponding to higher temperatures for non-isothermal TGA analysis) are expected with increased mass of reactant, even when a catalyst is used, fractional conversion, α , does not appear to capture the advantage of the initial mass-independent variable offered by concentration in solution-based reactions. Accordingly, α does not qualify as a universal parameter to obtain reaction kinetics in condensed phases, even when the iso-conversional method is used (Flynn, 1983). The use of α as a tool for comparing condensed phase reaction kinetics should therefore be limited to cases where the same initial and final masses are attained. As proposed by Abu Tarboush and Husein, reaction kinetics for adsorbed species in condensed phases is best evaluated based on mass reacted per unit area (Abu Tarboush & Husein, 2012b).

Given the fact that the thermo-oxidative profiles of adsorbed asphaltenes were mass dependent and NPs with different chemical nature displayed similar α versus temperature trends at the same mg/g uptake (e.g. Fe_2O_3 and Fe_3O_4 at their q_{max}), it is concluded that NPs promote asphaltenes oxidation through surface exposure rather than catalytic effect (Abu Tarboush & Husein, 2012b, 2015). The effectiveness of NPs toward the oxidation of adsorbed asphaltenes displayed the reverse trend to their q_{max} in mg/g ($\text{Al}_2\text{O}_3 > \text{Fe}_3\text{O}_4 \approx \text{Fe}_2\text{O}_3$). The higher the adsorption of asphaltene, the lower their exposure to the air stream and, subsequently, the lesser the rate of their oxidation.

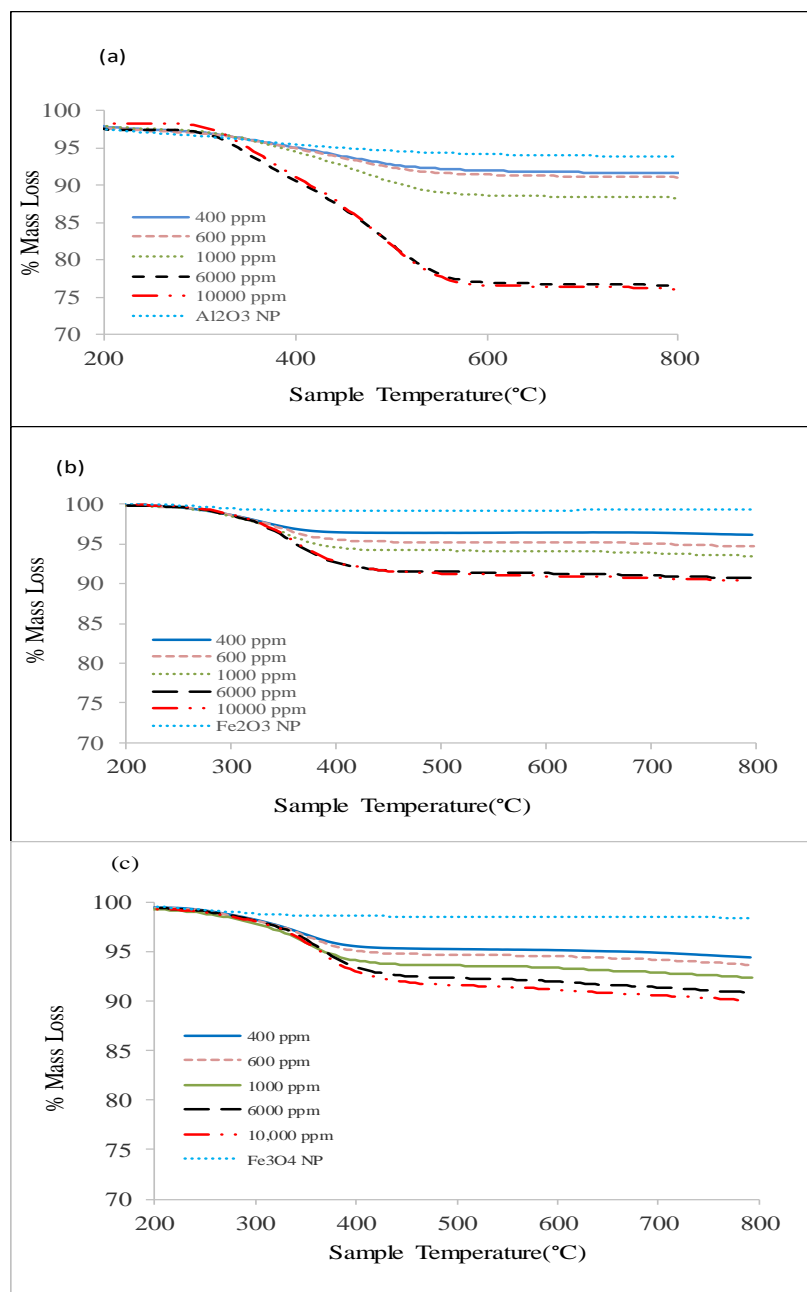


Figure 4.15: % Mass loss vs. temperature curves of asphaltene solutions onto (a) Al_2O_3 (b) Fe_2O_3 (c) Fe_3O_4 .

Chapter 5: Conclusions, Contributions and Recommendations

5.1 Conclusions

In this study, asphaltene adsorption onto Fe_2O_3 , Fe_3O_4 and Al_2O_3 NPs was investigated and isotherms based on three UV-Vis wavelengths and TGA were established and compared. The NPs were characterized using surface area analyzer, TEM, DRIFTS, and XRD. The asphaltenes were analyzed in the solid phase using DRIFTS, elemental analyzer and XRD and in the model solution using DLS and RI. The structural parameters of the asphaltenes extracted in this study fall within the range of 45 different asphaltenes studied in the literature.

While capturing the type of adsorption isotherm, UV-Vis spectroscopy did not provide reliable isotherm parameters. TGA results, on the other hand, produced more reliable uptake values, given that complete account of mass loss due to the NPs and complete oxidation of the adsorbed material is ensured. Most likely, the UV-Vis spectroscopy measurements were impacted by the association state of the asphaltenes and the selective adsorption of asphaltenes sub fractions. For all the NPs, Langmuir model fitted best to the experimental data, suggesting monolayer adsorption. The amount of adsorbed asphaltenes per NP supports the monolayer adsorption model and suggests asphaltene monomer, dimer and/or trimer equilibrium among three pseudophases: the bulk organic, the nanoaggregates and the surface of the NPs.

The NPs promoted the oxidation of adsorbed asphaltenes in a reverse trend to their uptake in (mg/g). NPs having similar q_{max} (in mg/g) displayed same fractional conversion, α , profiles versus temperature. Given the different chemical nature of the NPs, it is concluded that NPs promote oxidation of adsorbed asphaltenes through surface exposure, rather than catalytic effect. Accordingly, interpretations of α versus temperature curves may lead to false conclusions, unless same initial and final masses are used. Given the dependency of α on the initial mass, α does not qualify as universal intensive parameter to estimate reaction kinetics for condensed states.

5.2 Contributions

This thesis has contributed the following to knowledge:

- The study of the adsorption of asphaltenes with UV-Vis may not be as reliable as originally thought. The many results reported in the literature for asphaltenes adsorption on many surfaces should be re-checked employing other techniques; including TGA.
- Fractional conversion, α , is mass dependent, therefore does not qualify as a universal parameter to obtain reaction kinetics. It is amazing how many literature contributions used α as a basis to extract kinetic parameters of different reactions, e.g. oxidation, combustion, pyrolysis and gasification, without really questioning the validity of α and whether it provides a reliable parameter for extracting kinetic parameters.
- The role of nanoparticles in thermo-oxidative reactions is limited to improving the exposure of the adsorbed material to the oxidizing stream. Such a role may not be limited to oxidation reaction. It could, for example, also impact heat transfer driven reactions such as pyrolysis.

5.3 Recommendations for Future Work

- Further investigate the surface exposure role of the nanoparticles in promoting asphaltenes oxidation. This could be implemented by comparing adsorbed versus virgin asphaltenes mixed with the nanoparticles.
- Explore the role of nanoparticles on promoting other types of reactions, e.g. pyrolysis and gasification, to identify whether this role is catalysis-based or mass transfer-based.
- Explore the possibility of carrying out same adsorption tests at stimulated reservoir conditions
- Compare in situ prepared nanoparticles with the commercial ones even within model solutions.

References

- Abu Tarboush, B. J. (2014). *Adsorption and Oxidation of Asphaltenes onto in situ Prepared and Commercial Nanoparticles*. University of Calgary.
- Abu Tarboush, B. J., & Husein, M. M. (2012a). Adsorption of asphaltenes from heavy oil onto in situ prepared NiO nanoparticles. *Journal of Colloid and Interface Science*, 378(1), 64–69. <https://doi.org/10.1016/j.jcis.2012.04.016>
- Abu Tarboush, B. J., & Husein, M. M. (2012b). Oxidation of asphaltenes adsorbed onto NiO nanoparticles. *Applied Catalysis A: General*, 445–446, 166–171. <https://doi.org/10.1016/j.apcata.2012.08.019>
- Abu Tarboush, B. J., & Husein, M. M. (2015). Dispersed Fe₂O₃ nanoparticles preparation in heavy oil and their uptake of asphaltenes. *Fuel Processing Technology*, 133, 120–127. <https://doi.org/10.1016/j.fuproc.2014.12.049>
- Abudu, A., & Goual, L. (2009). Adsorption of Crude Oil on Surfaces Using Quartz Crystal Microbalance with Dissipation (QCM-D) under Flow Conditions †. *Energy & Fuels*, 23(3), 1237–1248. <https://doi.org/10.1021/ef800616x>
- Acevedo, S., Ranaudo, M. A., Escobar, G., Gutiérrez, L., & Ortega, P. (1995). Adsorption of asphaltenes and resins on organic and inorganic substrates and their correlation with precipitation problems in production well tubing. *Fuel*, 74(4), 595–598. [https://doi.org/10.1016/0016-2361\(95\)98363-J](https://doi.org/10.1016/0016-2361(95)98363-J)
- Acevedo, S., Ranaudo, M. A., García, C., Castillo, J., Fernández, A., Caetano, M., & Goncalvez, S. (2000). Importance of asphaltene aggregation in solution in determining the adsorption of this sample on mineral surfaces. *Colloids and Surfaces A: Physicochemical and Engineering Aspects*, 166(1–3), 145–152. [https://doi.org/10.1016/S0927-7757\(99\)00502-6](https://doi.org/10.1016/S0927-7757(99)00502-6)
- Adams, J. J. (2014). Asphaltene Adsorption, a Literature Review. *Energy and Fuels*, 28(5), 2831–2856. <https://doi.org/10.1021/ef500282p>

- Akhlaq, M. S., Götze, P., Kessel, D., & Dornow, W. (1997). Adsorption of crude oil colloids on glass plates: Measurements of contact angles and the factors influencing glass surface properties. *Colloids and Surfaces A: Physicochemical and Engineering Aspects*, 126(1), 25–32. [https://doi.org/10.1016/S0927-7757\(96\)03947-7](https://doi.org/10.1016/S0927-7757(96)03947-7)
- Alboudwarej, H., Pole, D., Svrcek, W. Y., & Yarranton, H. W. (2005). Adsorption of asphaltenes on metals. *Industrial and Engineering Chemistry Research*, 44(15), 5585–5592. <https://doi.org/10.1021/ie048948f>
- Alhumaidan, F. S., Hauser, A., Rana, M. S., & Lababidi, H. M. S. (2016). Impact of Thermal Treatment on Asphaltene Functional Groups. *Energy and Fuels*, 30(4), 2892–2903. <https://doi.org/10.1021/acs.energyfuels.6b00261>
- Andersen, S. I., Jensen, J. O., & Speight, J. G. (2005). X-ray diffraction of subfractions of petroleum asphaltenes. *Energy and Fuels*, 19(6), 2371–2377. <https://doi.org/10.1021/ef050039v>
- Andersen, S. I., Keul, A., & Stenby, E. (1997). *Variation in Composition of Subfractions of Petroleum Asphaltenes*. *Petroleum Science and Technology* (Vol. 15). Taylor & Francis Group. <https://doi.org/10.1080/10916469708949678>
- Andreatta, G., Bostrom, N., & Mullins, O. C. (2005). High-Q ultrasonic determination of the critical nanoaggregate concentration of asphaltenes and the critical micelle concentration of standard surfactants. *Langmuir*, 21(7), 2728–2736. <https://doi.org/10.1021/la048640t>
- Asaoka, S., Nakata, S., Shiroto, Y., & Takeuchi, C. (1983). Asphaltene Cracking in Catalytic Hydrotreating of Heavy Oils. 2. Study of Changes in Asphaltene Structure during Catalytic Hydroprocessing. *Industrial and Engineering Chemistry Process Design and Development*, 22(2), 242–248. <https://doi.org/10.1021/i200021a013>
- Asemani, M., & Rabbani, A. R. (2016). Oil-oil correlation by FTIR spectroscopy of asphaltene samples. *Geosciences Journal*, 20(2), 273–283. <https://doi.org/10.1007/s12303-015-0042-1>

- Baalousha, M., & Lead, J. R. (2015). 2.2.3.2 Static Light Scattering. In *Frontiers of Nanoscience, Volume 8 - Characterization of Nanomaterials in Complex Environmental and Biological Media*. Elsevier.
- Banda-Cruz, E., Padrón-Ortega, S., Gallardo-Rivas, N., Páramo-García, U., Díaz-Zavala, N., & Melo-Banda, A. (2017). Physicochemical Characterization of Heavy Oil and the Precipitated Asphaltenes Fraction using UV Spectroscopy and Dynamic Light Scattering. *Journal of Engineering Technology*, 6(1), 49–58.
- Banerjee, S., & Tyagi, A. K. (2012). 1.6.1.3 Dynamic Light Scattering. In *Functional Materials - Preparation, Processing and Applications*. Elsevier.
- Bantignies, J. L., Cartier Dit Moulin, C., & Dexpert, H. (1998). Asphaltene adsorption on kaolinite characterized by infrared and X-ray absorption spectroscopies. *Journal of Petroleum Science and Engineering*, 20(3–4), 233–237. [https://doi.org/10.1016/S0920-4105\(98\)00025-4](https://doi.org/10.1016/S0920-4105(98)00025-4)
- Battikha, N. E. (2007). 3.2.8 Fourier Transform Infrared (FTIR). In *Condensed Handbook of Measurement and Control (3rd Edition)*. ISA.
- Belkov, M. V., Brinkevich, S. D., Samovich, S. N., Skornyakov, I. V., Tolstorozhev, G. B., & Shadyro, O. I. (2012). Infrared spectra and structure of molecular complexes of aromatic acids. *Journal of Applied Spectroscopy*, 78(6), 794–801. <https://doi.org/10.1007/s10812-012-9535-0>
- Betancourt, S. S., Ventura, G. T., Pomerantz, A. E., Vilorio, O., Dubost, F. X., Zuo, J., ... Mullins, O. C. (2009). Nanoaggregates of asphaltenes in a reservoir crude oil and reservoir connectivity. In *Energy and Fuels* (Vol. 23, pp. 1178–1188). American Chemical Society. <https://doi.org/10.1021/ef800598a>
- Bhattacharya, S. N., Kamal, M. R., & Gupta, R. K. (2008). 6.2.1 X-ray Scattering Fundamentals. In *Polymeric Nanocomposites - Theory and Practice*. Hanser Publishers.
- Boduszynski, M. M. (1988). Composition of Heavy Petroleums. 2. Molecular Characterization.

- Energy and Fuels*, 2(5), 597–613. <https://doi.org/10.1021/ef00011a001>
- Borton, D., Pinkston, D., Hurt, M., Tan, X., & Azyat, K. (2010). Molecular structures of asphaltenes based on the dissociation reactions of their ions in mass spectrometry. *Energy & Fuels*, 24(10), 5548–5559.
- Bouhadda, Y., Bendedouch, D., Sheu, E., & Krallafa, A. (2000). Some preliminary results on a physico-chemical characterization of a Hassi Messaoud petroleum asphaltene. *Energy & Fuels*, 14(4), 845–853. <https://doi.org/10.1021/EF9902092>
- Bouhadda, Y., Bormann, D., Sheu, E., & Bendedouch, D. (2007). Characterization of Algerian Hassi-Messaoud asphaltene structure using Raman spectrometry and X-ray diffraction. *Fuel*, 86(12–13), 1855–1864. <https://doi.org/10.1016/j.fuel.2006.12.006>
- Buenrostro-Gonzalez, E., Andersen, S. I., Garcia-Martinez, J. A., & Lira-Galeana, C. (2002). Solubility/molecular structure relationships of asphaltenes in polar and nonpolar media. *Energy and Fuels*, 16(3), 732–741. <https://doi.org/10.1021/ef0102317>
- Calemma, V., Iwanski, P., Nali, M., Scotti, R., & Montanari, L. (1995). Structural Characterization of Asphaltenes of Different Origins. *Energy and Fuels*, 9(2), 225–230. <https://doi.org/10.1021/ef00050a004>
- Canadian Association of Petroleum Producers. (2018). The World Needs Energy. Retrieved March 3, 2018, from <https://www.capp.ca/canadian-oil-and-natural-gas/why-we-need-energy>
- Carbognani, L. (2000). Effects of Iron Compounds on the Retention of Oil Polar Hydrocarbons Over Solid Sorbents. *Pet. Sci. Technol.*, 18(3–4), 335–360. <https://doi.org/10.1080/10916460008949850>
- Carbognani, L., Espidel, J., & Izquierdo, A. (2000). Chapter 13 Characterization of Asphaltenic Deposits from Oil Production and Transportation Operations. *Developments in Petroleum Science*, 40(PART B), 335–362. [https://doi.org/10.1016/S0376-7361\(09\)70284-5](https://doi.org/10.1016/S0376-7361(09)70284-5)

- Carnahan, N. F. (2000). Chapter 12 Precipitation of Asphaltenes in Heavy Oil and Tar Sands. *Developments in Petroleum Science*, 40(PART B), 319–333. [https://doi.org/10.1016/S0376-7361\(09\)70283-3](https://doi.org/10.1016/S0376-7361(09)70283-3)
- Castillo, J., Fernández, A., Ranaudo, M. A., & Acevedo, S. (2001). New techniques and methods for the study of aggregation, adsorption, and solubility of asphaltenes. Impact of these properties on colloidal structure and flocculation. *Petroleum Science and Technology*, 19(1–2), 75–106. <https://doi.org/10.1081/LFT-100001227>
- Castro, M., de la Cruz, J. L. M., Buenrostro-Gonzalez, E., López-Ramírez, S., & Gil-Villegas, A. (2009). Predicting adsorption isotherms of asphaltenes in porous materials. *Fluid Phase Equilibria*, 286(2), 113–119. <https://doi.org/10.1016/j.fluid.2009.08.009>
- Christy, A. A., Dahl, B., & Kvalheim, O. M. (1989). Structural features of resins, asphaltenes and kerogen studied by diffuse reflectance infrared spectroscopy. *Fuel*, 68(4), 430–435. [https://doi.org/10.1016/0016-2361\(89\)90263-9](https://doi.org/10.1016/0016-2361(89)90263-9)
- Clementz, D. M. (1976). Interaction of petroleum heavy ends with montmorillonite. *Clays and Clay Minerals*, 24(6), 312–319. <https://doi.org/10.1346/CCMN.1976.0240607>
- Cosgrove, T. (2010). 13.8 Small Angle Scattering Apparatus. In *Colloid Science - Principles, Methods and Applications (2nd Edition)*. John Wiley & Sons.
- Coward, J. L. (2010). FTIR spectroscopy of synthesized racemic nonacosan-10-ol: a model compound for plant epicuticular waxes. *Journal of Biological Physics*, 36(4), 405–425. <https://doi.org/10.1007/s10867-010-9192-6>
- Crompton, T. R. (2008). 5.2.1 Instrumentation. In *Characterisation of Polymers, Volume 1* (pp. 290–291). Smithers Rapra Technology.
- Czarnecka, E., & Gillott, J. E. (1980). Formation and characterization of clay complexes with bitumen from Athabasca oil sand. *Clays and Clay Minerals*. <https://doi.org/10.1346/CCMN.1980.0280305>

- David Ting, P., Hirasaki, G. J., & Chapman, W. G. (2003). Modeling of Asphaltene Phase Behavior with the SAFT Equation of State. *Petroleum Science and Technology*, 21(June 2014), 647–661. <https://doi.org/10.1081/LFT-120018544>
- Davis, R. F. (1993a). 4.1 Transmission Electron Microscopy. In *Diamond Films and Coatings*. William Andrew Publishing/Noyes.
- Davis, R. F. (1993b). 5.1 X-Ray Diffraction. In *Diamond Films and Coatings*. William Andrew Publishing/Noyes.
- Desta, M. B. (2013). Batch sorption experiments: Langmuir and freundlich isotherm studies for the adsorption of textile metal ions onto teff straw (eragrostis tef) agricultural waste. *Journal of Thermodynamics*, 1(1), 1–6. <https://doi.org/10.1155/2013/375830>
- Dordević, D. M., Stanković, M. N., Dordević, M. G., Krstić, N. S., Pavlović, M. A., Radivojević, A. R., & Filipović, I. M. (2012). Ftir spectroscopic characterization of bituminous limestone: Maganik mountain (Montenegro). *Studia Universitatis Babes-Bolyai Chemia*, 4(4), 39–54.
- Douda, J., Llanos, M. E., Alvarez, R., & Bolaños, J. N. (2004). Structure of Maya asphaltene-resin complexes through the analysis of soxhlet extracted fractions. *Energy and Fuels*, 18(3), 736–742. <https://doi.org/10.1021/ef034057t>
- Dudášová, D., Silset, A., & Sjöblom, J. (2008). Quartz crystal microbalance monitoring of asphaltene adsorption/ deposition. *Journal of Dispersion Science and Technology*, 29(1), 139–146. <https://doi.org/10.1080/01932690701688904>
- Dudášová, D., Simon, S., Hemmingsen, P. V., & Sjöblom, J. (2008). Study of asphaltenes adsorption onto different minerals and clays. Part 1. Experimental adsorption with UV depletion detection. *Colloids and Surfaces A: Physicochemical and Engineering Aspects*, 317(1–3), 1–9. <https://doi.org/10.1016/j.colsurfa.2007.09.023>
- Dulski, T. R. (1996). 13.1 UV/Visible Molecular Absorption. In *A Manual for the Chemical Analysis of Metals: (MNL 25)*. ASTM International.

- Durand, E., Clemancey, M., Lancelin, J. M., Verstraete, J., Espinat, D., & Quoineaud, A. A. (2009). Aggregation states of asphaltenes: Evidence of two chemical behaviors by ^1H diffusion-ordered spectroscopy nuclear magnetic resonance. *Journal of Physical Chemistry C*, 113(36), 16266–16276. <https://doi.org/10.1021/jp901954b>
- Durand, E., Clemancey, M., Lancelin, J. M., Verstraete, J., Espinat, D., & Quoineaud, A. A. (2010). Effect of chemical composition on asphaltenes aggregation. *Energy and Fuels*, 24(2), 1051–1062. <https://doi.org/10.1021/ef900599v>
- Dutta Majumdar, R., Gerken, M., Mikula, R., & Hazendonk, P. (2013). Validation of the Yen-Mullins model of athabasca oil-sands asphaltenes using solution-state ^1H NMR relaxation and 2D HSQC spectroscopy. *Energy and Fuels*, 27(11), 6528–6537. <https://doi.org/10.1021/ef401412w>
- Ekholm, P., Blomberg, E., Claesson, P., Auflem, I. H., Sjöblom, J., & Kornfeldt, A. (2002). A Quartz Crystal Microbalance Study of the Adsorption of Asphaltenes and Resins onto a Hydrophilic Surface. *Journal of Colloid and Interface Science*, 247(2), 342–350. <https://doi.org/10.1006/jcis.2002.8122>
- Evdokimov, I. N., Eliseev, N. Y., & Akhmetov, B. R. (2003). Initial stages of asphaltene aggregation in dilute crude oil solutions: Studies of viscosity and NMR relaxation. *Fuel*, 82(7), 817–823. [https://doi.org/10.1016/S0016-2361\(02\)00336-8](https://doi.org/10.1016/S0016-2361(02)00336-8)
- Evdokimov, I. N., Fesan, A. A., & Losev, A. P. (2017). Asphaltenes: Absorbers and Scatterers at Near-Ultraviolet-Visible-Near-Infrared Wavelengths. *Energy and Fuels*, 31(4), 3878–3884. <https://doi.org/10.1021/acs.energyfuels.7b00114>
- Evdokimov, I. N., & Losev, A. P. (2007). Effects of molecular de-aggregation on refractive indices of petroleum-based fluids. *Fuel*, 86(15), 2439–2445. <https://doi.org/10.1016/j.fuel.2007.01.017>
- Evdokimov, I. N., & Losev, A. P. (2007). On the nature of UV/Vis absorption spectra of

- asphaltenes. *Petroleum Science and Technology*, 25(1–2), 55–66.
<https://doi.org/10.1080/10916460601186420>
- Eyssautier, J., Levitz, P., Espinat, D., Jestin, J., Gummel, J., Grillo, I., & Barré, L. (2011). Insight into asphaltene nanoaggregate structure inferred by small angle neutron and X-ray scattering. *Journal of Physical Chemistry B*, 115(21), 6827–6837. <https://doi.org/10.1021/jp111468d>
- Ezeonyeka, N. L., Hemmati-Sarapardeh, A., & Husein, M. M. (2018). Asphaltenes Adsorption onto Metal Oxide Nanoparticles: A Critical Evaluation of Measurement Techniques. *Energy & Fuels*, 32(2), 2213–2223. <https://doi.org/10.1021/acs.energyfuels.7b03693>
- Farahmandjou, M., & Soflaee, F. (2015). Synthesis and Characterization of α -Fe₂O₃ Nanoparticles by Simple Co-Precipitation Method. *Physical Chemistry Research*, 3(3), 191–196. <https://doi.org/10.22036/pcr.2015.9193>
- Flynn, J. H. (1983). The isoconversional method for determination of energy of activation at constant heating rates - Corrections for the Doyle approximation. *Journal of Thermal Analysis*, 27(1), 95–102. <https://doi.org/10.1007/BF01907325>
- Foo, K. Y., & Hameed, B. H. (2010). Insights into the modeling of adsorption isotherm systems. *Chemical Engineering Journal*. <https://doi.org/10.1016/j.cej.2009.09.013>
- Franco, C. A., Montoya, T., Nassar, N. N., Pereira-Almao, P., & Cortés, F. B. (2013). Adsorption and subsequent oxidation of colombian asphaltenes onto nickel and/or palladium oxide supported on fumed silica nanoparticles. *Energy and Fuels*, 27(12), 7336–7347. <https://doi.org/10.1021/ef4018543>
- Gaboriau, H., & Saada, A. (2001). Influence of heavy organic pollutants of anthropic origin on PAH retention by kaolinite. *Chemosphere*, 44(7), 1633–1639. [https://doi.org/10.1016/S0045-6535\(00\)00527-0](https://doi.org/10.1016/S0045-6535(00)00527-0)
- Gianfrancesco, A. Di. (2017). 8.1.4.7 Transmission electron microscopy (TEM). In *Materials for Ultra-Supercritical and Advanced Ultra-Supercritical Power Plants*. Elsevier.

- Giraldo, L., Erto, A., & Moreno-Piraján, J. C. (2013). Magnetite nanoparticles for removal of heavy metals from aqueous solutions: synthesis and characterization. *Adsorption*, 19(2–4), 465–474. <https://doi.org/10.1007/s10450-012-9468-1>
- Goncalves, S., Castillo, J., Fernández, A., & Hung, J. (2004). Absorbance and fluorescence spectroscopy on the aggregation behavior of asphaltene-toluene solutions. *Fuel*, 83(13), 1823–1828. <https://doi.org/10.1016/j.fuel.2004.03.009>
- González, G., & Middea, A. (1987). Asphaltenes adsorption by quartz and feldspar. *Journal of Dispersion Science and Technology*, 8(5–6), 525–548. <https://doi.org/10.1080/01932698708943621>
- Gonzalez, V., & Taylor, S. E. (2016). Asphaltene adsorption on quartz sand in the presence of pre-adsorbed water. *Journal of Colloid and Interface Science*, 480, 137–145. <https://doi.org/10.1016/j.jcis.2016.07.014>
- Goual, L. (2009). Impedance spectroscopy of petroleum fluids at low frequency. *Energy and Fuels*, 23(4), 2090–2094. <https://doi.org/10.1021/ef800860x>
- Goual, L., Horváth-Szabó, G., Masliyah, J. H., & Xu, Z. (2005). Adsorption of bituminous components at oil/water interfaces investigated by quartz crystal microbalance: Implications to the stability of water-in-oil emulsions. *Langmuir*, 21(18), 8278–8289. <https://doi.org/10.1021/la050333f>
- Gray, M. R., Tykwinski, R. R., Stryker, J. M., & Tan, X. (2011). Supramolecular assembly model for aggregation of petroleum asphaltenes. In *Energy and Fuels* (Vol. 25, pp. 3125–3134). American Chemical Society. <https://doi.org/10.1021/ef200654p>
- Groenzin, H., & Mullins, O. C. (1999). Petroleum Asphaltene Molecular Size and Structure. *ACS Division of Fuel Chemistry, Preprints*, 44(4), 728–732. <https://doi.org/10.1021/jp992609w>
- Groenzin, H., & Mullins, O. C. (2000). Molecular Size and Structure of Asphaltenes from Various Sources. *Energy & Fuels*, 14(3), 677–684. <https://doi.org/10.1021/ef990225z>

- Gudmundsson, J. S. (2017). *Flow Assurance Solids in Oil and Gas Production* (1st ed.). Milton, United Kingdom: CRC Press.
- Gunasekaran, S., Sailatha, E., Seshadri, S., & Kumaresan, S. (2009). FTIR, FT Raman spectra and molecular structural confirmation of isoniazid. *Indian Journal of Pure and Applied Physics*, 47(1), 12–18.
- Harvey W. Yarranton, Hussein Alboudwarej, A., Jakher, R., Yarranton, H., & Alboudwarej, H. (2000). Investigation of Asphaltene Association with Vapor Pressure Osmometry and Interfacial Tension Measurements. *Industrial & Engineering Chemistry Research*, 39, 2916–2924. <https://doi.org/10.1021/IE000073R>
- Hastings, G., Bandaranayake, K. M. P., & Carrion, E. (2008). Time-resolved FTIR difference spectroscopy in combination with specific isotope labeling for the study of A1, the secondary electron acceptor in photosystem 1. *Biophysical Journal*, 94(11), 4383–4392. <https://doi.org/10.1529/biophysj.107.113191>
- He, L., Lin, F., Li, X., Sui, H., & Xu, Z. (2015). Interfacial sciences in unconventional petroleum production: from fundamentals to applications. *Chem. Soc. Rev.*, 44(15), 5446–5494. <https://doi.org/10.1039/C5CS00102A>
- Hemmati-Sarapardeh, A., Alipour-Yeganeh-Marand, R., Naseri, A., Safiabadi, A., Gharagheizi, F., Ilani-Kashkouli, P., & Mohammadi, A. H. (2013). Asphaltene precipitation due to natural depletion of reservoir: Determination using a SARA fraction based intelligent model. *Fluid Phase Equilibria*, 354, 177–184. <https://doi.org/10.1016/j.fluid.2013.06.005>
- Hlady, V., Lyklema, J., & Fleer, G. J. (1982). Effect of polydispersity on the adsorption of dextran on silver iodide. *Journal of Colloid And Interface Science*, 87(2), 395–406. [https://doi.org/10.1016/0021-9797\(82\)90336-8](https://doi.org/10.1016/0021-9797(82)90336-8)
- Hortal, A. R., Hurtado, P., Martnez-haya, B., Mullins, O. C., & Martı, B. (2007). Molecular-Weight Distributions of Coal and Petroleum Asphaltenes from Laser Desorption / Ionization

- Experiments Molecular-Weight Distributions of Coal and Petroleum Asphaltenes from Laser Desorption / Ionization Experiments. *Energy & Fuels*, (15), 2863–2868. <https://doi.org/10.1021/ef700225s>
- Hosseinpour, N., Khodadadi, A. A., Bahramian, A., & Mortazavi, Y. (2013). Asphaltene adsorption onto acidic/basic metal oxide nanoparticles toward in situ upgrading of reservoir oils by nanotechnology. *Langmuir*, 29(46), 14135–14146. <https://doi.org/10.1021/la402979h>
- Hosseinpour, N., Mortazavi, Y., Bahramian, A., Khodatars, L., & Khodadadi, A. A. (2014). Enhanced pyrolysis and oxidation of asphaltenes adsorbed onto transition metal oxides nanoparticles towards advanced in-situ combustion EOR processes by nanotechnology. *Applied Catalysis A: General*, 477, 159–171. <https://doi.org/10.1016/j.apcata.2014.03.017>
- Husein, M. M., & Alkhaldi, S. J. (2014). In situ preparation of alumina nanoparticles in heavy oil and their thermal cracking performance. *Energy and Fuels*, 28(10), 6563–6569. <https://doi.org/10.1021/ef5012963>
- Indo, K., Ratulowski, J., Dindoruk, B., Gao, J., Zuo, J., & Mullins, O. C. (2009). Asphaltene nanoaggregates measured in a live crude oil by centrifugation. *Energy and Fuels*, 23(9), 4460–4469. <https://doi.org/10.1021/ef900369r>
- Jean-Pierre Wauquier. (1995). Composition of Crude Oil and Petroleum Products. In Technip (Ed.), *Petroleum Refining: Crude oil, petroleum products, process flowsheets Vol.1* (Technip).
- Kamari, A., Safiri, A., & Mohammadi, A. H. (2015). Compositional Model for Estimating Asphaltene Precipitation Conditions in Live Reservoir Oil Systems. *Journal of Dispersion Science and Technology*, 36(3), 301–309. <https://doi.org/10.1080/01932691.2014.896220>
- Karan, K., Hammami, A., Flannery, M., & Artur Stankiewicz, B. (2003). Evaluation of Asphaltene Instability and a Chemical Control During Production of Live Oils. *Petroleum Science and Technology*, 21(3–4), 629–645. <https://doi.org/10.1081/LFT-120018543>

- Kawashima, H., Takanohashi, T., Iino, M., & Matsukawa, S. (2008). Determining asphaltene aggregation in solution from diffusion coefficients as determined by pulsed-field gradient spin-echo ^1H NMR. *Energy and Fuels*, 22(6), 3989–3993. <https://doi.org/10.1021/ef800455g>
- Kokal, S., Tang, T., Schramm, L., & Sayegh, S. (1995). Electrokinetic and adsorption properties of asphaltenes. *Colloids and Surfaces A: Physicochemical and Engineering Aspects*, 94(2–3), 253–265. [https://doi.org/10.1016/0927-7757\(94\)03007-3](https://doi.org/10.1016/0927-7757(94)03007-3)
- Kutz, M. (2013). 44.3.5 Modulated TGA (MTGA). In *Handbook of Measurement in Science and Engineering, Volume 2*. John Wiley & Sons.
- Langevin, D., & Argillier, J. F. (2016, July 1). Interfacial behavior of asphaltenes. *Advances in Colloid and Interface Science*. Elsevier. <https://doi.org/10.1016/j.cis.2015.10.005>
- Larsen, J. W., & Li, S. (1995). Determination of Bitumen Molecular Weight Distributions Using ^{252}Cf Plasma Desorption Mass Spectrometry. *Energy and Fuels*, 9(5), 760–764. <https://doi.org/10.1021/ef00053a005>
- León, O., Contreras, E., Rogel, E., Dambakli, G., Acevedo, S., Carbognani, L., & Espidel, J. (2002). Adsorption of native resins on asphaltene particles: A correlation between adsorption and activity. *Langmuir*, 18(13), 5106–5112. <https://doi.org/10.1021/la011394q>
- León, O., Rogel, E., Espidel, J., & Torres, G. (2000). Asphaltenes: Structural characterization, self-association, and stability behavior. *Energy and Fuels*, 14(1), 6–10. <https://doi.org/10.1021/ef9901037>
- Lian, H., Lin, J. R., & Yen, T. F. (1994). Peptization studies of asphaltene and solubility parameter spectra. *Fuel*, 73(3), 423–428. [https://doi.org/10.1016/0016-2361\(94\)90097-3](https://doi.org/10.1016/0016-2361(94)90097-3)
- Lisitza, N. V., Freed, D. E., Sen, P. N., & Song, Y. Q. (2009). Study of asphaltene nanoaggregation by nuclear magnetic resonance (NMR). In *Energy and Fuels* (Vol. 23, pp. 1189–1193). American Chemical Society. <https://doi.org/10.1021/ef800631a>

- Liu, Y.-J., & Li, Z.-F. (2015). Structural Characterisation of Asphaltenes during Residue Hydrotreatment with Light Cycle Oil as an Additive. *Journal of Chemistry*, 2015, 1–8. <https://doi.org/10.1155/2015/580950>
- Luo, P., & Gu, Y. (2007). Effects of asphaltene content on the heavy oil viscosity at different temperatures. *Fuel*, 86(7–8), 1069–1078. <https://doi.org/10.1016/j.fuel.2006.10.017>
- Maher, A.-J., & Husien, M. M. (2007). Review of Adsorption of Asphaltenes onto Surfaces and its Application in Heavy Oil Recovery / Upgrading and Environmental Protection. In *Proceedings of 3rd ICCE*. Kuwait.
- Maher, A.-J., Nassar, N. N., & Husien, M. M. (2007). Separation of Asphaltenes from Heavy Oil Model-Solutions by Adsorption on Colloidal Magnetite Nanoparticles. In *Proceedings of 3rd ICCE*. Kuwait.
- Mang, Y., Liu, C., & Liang, W. (1989). Study of Asphaltenes in two Chinese Asphalts by X-Ray Diffraction. *Fuel Science and Technology International*, 7(7), 919–929. <https://doi.org/10.1080/08843758908962274>
- Mansur, C. R. E., De Melo, A. R., & Lucas, E. F. (2012). Determination of asphaltene particle size: Influence of flocculant, additive, and temperature. *Energy and Fuels*, 26(8), 4988–4994. <https://doi.org/10.1021/ef300365x>
- Marczewski, A. A. W., & Szymula, M. (2002). Adsorption of asphaltenes from toluene on mineral surface. *Colloids and Surfaces A: Physicochemical*, 208(1), 259–266. [https://doi.org/10.1016/S0927-7757\(02\)00152-8](https://doi.org/10.1016/S0927-7757(02)00152-8)
- Marlow, B. J., Sresty, G. C., Hughes, R. D., & Mahajan, O. P. (1987). Colloidal stabilization of clays by asphaltenes in hydrocarbon media. *Colloids and Surfaces*, 24(4), 283–297. [https://doi.org/10.1016/0166-6622\(87\)80235-4](https://doi.org/10.1016/0166-6622(87)80235-4)
- Martinez, M. T., Miranda, J. L., & Juan, R. (1988). Catalytic hydrotreating of coal liquids. *Fuel*, 67(9), 1197–1200. [https://doi.org/10.1016/0016-2361\(88\)90036-1](https://doi.org/10.1016/0016-2361(88)90036-1)

- Masson, J. F., Pelletier, L., & Collins, P. (2001). Rapid FTIR method for quantification of styrene-butadiene type copolymers in bitumen. *Journal of Applied Polymer Science*, 79(6), 1034–1041. [https://doi.org/10.1002/1097-4628\(20010207\)79:6<1034::AID-APP60>3.0.CO;2-4](https://doi.org/10.1002/1097-4628(20010207)79:6<1034::AID-APP60>3.0.CO;2-4)
- Mendoza de la Cruz, J. L., Castellanos-Ramírez, I. V., Ortiz-Tapia, A., Buenrostro-González, E., Durán-Valencia, C. de los A., & López-Ramírez, S. (2009). Study of monolayer to multilayer adsorption of asphaltenes on reservoir rock minerals. *Colloids and Surfaces A: Physicochemical and Engineering Aspects*, 340(1–3), 149–154. <https://doi.org/10.1016/j.colsurfa.2009.03.021>
- Merino-Garcia, D., Murgich, J., & Andersen, S. I. (2004). Asphaltene self-association: Modeling and effect of fractionation with a polar solvent. In *Petroleum Science and Technology* (Vol. 22, pp. 735–758). Taylor & Francis Group. <https://doi.org/10.1081/LFT-120038710>
- Meyer, R. (2003). Heavy Oil and Natural Bitumen. In *The Petroleum System- Status of Research and Methods, 1990*.
- Mohammadi, A. H., & Richon, D. (2007). A monodisperse thermodynamic model for estimating asphaltene precipitation. *AIChE Journal*, 53(11), 2940–2947. <https://doi.org/10.1002/aic.11304>
- Mohammadi, M., Dadvar, M., & Dabir, B. (2017). TiO₂/SiO₂ nanofluids as novel inhibitors for the stability of asphaltene particles in crude oil: Mechanistic understanding, screening, modeling, and optimization. *Journal of Molecular Liquids*, 238, 326–340. <https://doi.org/10.1016/j.molliq.2017.05.014>
- Mohammadi, M., Khomehchi, E., & Sedighi, M. (2014). The prediction of asphaltene adsorption isotherm constants on mineral surfaces. *Petroleum Science and Technology*, 32(7), 870–877. <https://doi.org/10.1080/10916466.2011.605091>
- Mohammadi, M., & Sedighi, M. (2013). Modification of Langmuir isotherm for the adsorption of asphaltene or resin onto calcite mineral surface: Comparison of linear and non-linear

- methods. *Protection of Metals and Physical Chemistry of Surfaces*, 49(4), 460–470. <https://doi.org/10.1134/S2070205113040205>
- Mohammadi, M., Sedighi, M., Hashemi Kiasari, H., & Hosseini, S. M. T. (2015a). Genetic Algorithm Development for Prediction of Modified Langmuir Isotherm Parameters of Asphaltene Adsorption onto Metal Surfaces: Using Novel Quartz Crystal Nanobalance. *Journal of Dispersion Science and Technology*, 36(3), 384–392. <https://doi.org/10.1080/01932691.2014.903806>
- Mohammadi, M., Sedighi, M., Hashemi Kiasari, H., & Hosseini, S. M. T. (2015b). Genetic Algorithm Development for Prediction of Modified Langmuir Isotherm Parameters of Asphaltene Adsorption onto Metal Surfaces: Using Novel Quartz Crystal Nanobalance. *Journal of Dispersion Science and Technology*, 36(3), 384–392. <https://doi.org/10.1080/01932691.2014.903806>
- Monshi, A., Foroughi, M. R., & Monshi, M. R. (2012). Modified Scherrer Equation to Estimate More Accurately Nano-Crystallite Size Using XRD. *World Journal of Nano Science and Engineering*, 2(3), 154–160. <https://doi.org/10.4236/wjnse.2012.23020>
- Mostowfi, F., Indo, K., Mullins, O. C., & McFarlane, R. (2009). Asphaltene nanoaggregates studied by centrifugation. In *Energy and Fuels* (Vol. 23, pp. 1194–1200). American Chemical Society. <https://doi.org/10.1021/ef8006273>
- Mullins, O. C. (2007). Petroleomics and Structure–Function Relations of Crude Oils and Asphaltenes. *Asphaltenes, Heavy Oils, and Petroleomics*, 1–16. https://doi.org/10.1007/0-387-68903-6_1
- Mullins, O. C. (2010). The Modified Yen Model [†]. *Energy & Fuels*, 24(4), 2179–2207. <https://doi.org/10.1021/ef900975e>
- Murgich, J., Rodríguez, & Aray, Y. (1996). Molecular Recognition and Molecular Mechanics of Micelles of Some Model Asphaltenes and Resins. *Energy & Fuels*, 10(1), 68–76.

<https://doi.org/10.1021/ef950112p>

N.Nassar;A. Hassan;P. Pereira-Almao. (2011). Comparative oxidation of adsorbed asphaltenes onto transition metal oxide nanoparticles. *Colloids and Surfaces A: Physicochemical and Engineering Aspects*, 384(1–3), 145–149.
<https://doi.org/10.1016/J.COLSURFA.2011.03.049>

Nalwaya, V., Tantayakom, V., Piumsomboon, P., & Fogler, S. (1999). Studies on Asphaltenes through Analysis of Polar Fractions. *Industrial & Engineering Chemistry Research*, 38(3), 964–972. <https://doi.org/10.1021/ie9804428>

Nassar, N. N. (2010). Asphaltene Adsorption onto Alumina Nanoparticles: Kinetics and Thermodynamic Studies. *Energy & Fuels*, 24(8), 4116–4122.
<https://doi.org/10.1021/ef100458g>

Nassar, N. N., Al-Jabari, M. E., & Husein, M. M. (2008). Removal of Asphaltenes from Heavy Oil by Nickel Nano and Micro Particle Adsorbents. In *Proceeding of the International Association of Science and Technology Development Conference on Nanotechnology and Applications (NANA 2008)* (pp. 171–175). Crete, Greece: ACTA Press.

Nassar, N. N., Hassan, A., & Pereira-almao, P. (2011). Effect of surface acidity and basicity of aluminas on asphaltene adsorption and oxidation. *Journal of Colloid And Interface Science*, 360(1), 233–238. <https://doi.org/10.1016/j.jcis.2011.04.056>

Nassar, N. N., Hassan, A., & Pereira-Almao, P. (2011a). Effect of the particle size on asphaltene adsorption and catalytic oxidation onto alumina particles. *Energy and Fuels*, 25(9), 3961–3965. <https://doi.org/10.1021/ef2008387>

Nassar, N. N., Hassan, A., & Pereira-Almao, P. (2011b). Metal Oxide Nanoparticles for Asphaltene Adsorption and Oxidation. *Energy & Fuels*, 25(3), 1017–1023.
<https://doi.org/10.1021/ef101230g>

Nassar, N. N., Hassan, A., & Vitale, G. (2014). Comparing kinetics and mechanism of adsorption

- and thermo-oxidative decomposition of Athabasca asphaltenes onto TiO₂, ZrO₂, and CeO₂ nanoparticles. *Applied Catalysis A: General*, 484, 161–171. <https://doi.org/10.1016/j.apcata.2014.07.017>
- Nikolic, V., Ilic, D., Nikolic, L., Stanojevic, L., Cakic, M., Tacic, A., & Ilic-Stojanovic, S. (2014). The synthesis and characterization of iron(II): Gluconate. *Savremene Tehnologije*, 3(2), 16–24. <https://doi.org/10.5937/savteh1402016N>
- Nivitha, M. R., Prasad, E., & Krishnan, J. M. (2016). Ageing in modified bitumen using FTIR spectroscopy. *International Journal of Pavement Engineering*, 17(7), 565–577. <https://doi.org/10.1080/10298436.2015.1007230>
- Orbulescu, J., Mullins, O. C., & Leblanc, R. M. (2010). Surface Chemistry and Spectroscopy of UG8 Asphaltene Langmuir Film, Part 1. *Langmuir*, 26(19), 15257–15264. <https://doi.org/10.1021/la101763b>
- Park, K., Kittelson, D. B., Zachariah, M. R., & McMurry, P. H. (2004). Measurement of inherent material density of nanoparticle agglomerates. *Journal of Nanoparticle Research*, 6(2–3), 267–272. <https://doi.org/10.1023/B:NANO.0000034657.71309.e6>
- Pernyeszi, T., & Dékány, I. (2001). Sorption and elution of asphaltenes from porous silica surfaces. *Colloids and Surfaces A: Physicochemical and*, 194, 25–39.
- Pernyeszi, T., Patzkó, Á., Berkesi, O., & Dékány, I. (1998). Asphaltene adsorption on clays and crude oil reservoir rocks. *Colloids and Surfaces A: Physicochemical and Engineering Aspects*, 137(1–3), 373–384. [https://doi.org/10.1016/S0927-7757\(98\)00214-3](https://doi.org/10.1016/S0927-7757(98)00214-3)
- Proceedings on International Conference on Recent Advances in Applied ... - ICRAAS 2016 - Google Books. (n.d.). Retrieved July 6, 2017, from https://books.google.ca/books?id=7JaNDQAAQBAJ&pg=PA316&lpg=PA316&dq=PROCEEDINGS+ON+INTERNATIONAL+CONFERENCE+ON+RECENT+ADVANCES+IN++APPLIED+SCIENCE&source=bl&ots=IFY8V0WsxS&sig=6EiB9eHF5uQ2xtgXq0Sn_fB

1Jqo&hl=en&sa=X&ved=0ahUKEwig46_JiPfUAhXJzIMKHUvcDhsQ6AE

- Ramirez-Corredores, M. M. (2017a). 2.4.1 Physical Properties. In *Science and Technology of Unconventional Oils- Finding Refining Opportunities* (p. 51). Elsevier.
- Ramirez-Corredores, M. M. (2017b). 2.4.4.3 Molecular Structures and Models. In *Science and Technology of Unconventional Oils - Finding Refining Opportunities* (p. 102). Elsevier.
- Rastgoo, A., & Kharrat, R. (2017). Investigation of Asphaltene Deposition and Precipitation in Production Tubing. *International Journal of Clean Coal and Energy*, 6(1), 14–29. <https://doi.org/10.4236/ijcce.2017.61002>
- Ratna, D. (2009). 1.10.7 Rheological Characterisation. In *Handbook of Thermoset Resins*. Smithers Rapra Technology.
- Riazi, M. R. (2013). Characteristics of Heavy Fractions for Design and Operation of Upgrading Related Processes. In *Proceedings of the 2013 AlchE Annual Meeting*. San Francisco, CA.
- Rudrake, A., Karan, K., & Horton, J. H. (2009). A combined QCM and XPS investigation of asphaltene adsorption on metal surfaces. *Journal of Colloid and Interface Science*, 332(1), 22–31. <https://doi.org/10.1016/j.jcis.2008.12.052>
- Rudyk, S., & Spirov, P. (2014). Upgrading and extraction of bitumen from Nigerian tar sand by supercritical carbon dioxide. *Applied Energy*, 113, 1397–1404. <https://doi.org/10.1016/j.apenergy.2013.08.076>
- Sabbah, H., Morrow, A. L., Pomerantz, A. E., & Zare, R. N. (2011). Evidence for island structures as the dominant architecture of asphaltenes. *Energy and Fuels*, 25(4), 1597–1604. <https://doi.org/10.1021/ef101522w>
- Sadeghi, M. A., Chilingarian, G. V., & Yen, T. F. (1986). X-ray diffraction of asphaltenes. *Energy Sources*, 8(2–3), 99–123. <https://doi.org/10.1080/00908318608946045>
- Saikia, B. J., Parthasarathy, G., & Sarmah, N. C. (2009). Fourier Transform Infrared Spectroscopic

- Characterization of Dergaon H5 Chondrite: Evidence of Aliphatic Organic Compound. *Nature and Science*, 7(5), 45–51.
- Sánchez-Lemus, M. C., Schoeggl, F. F., Taylor, S. D., Andersen, S. I., Mapolelo, M. M., Mahavadi, S. C., & Yarranton, H. W. (2016). Characterization of Heavy Distillation Cuts Using Fourier Transform Infrared Spectrometry: Proof of Concept. *Energy & Fuels*, 30(12), 10187–10199. <https://doi.org/10.1021/acs.energyfuels.6b01912>
- Sanda, F. M., Victor, M. E., Monica, T. A., & Alina, C. (2012). Spectrophotometric Measurements Techniques Fermentation Process (Part One): Base Theory for Uv-Vis Spectrophotometric Measurements. *Hungary-Romania Cross-Border Co-Operation Programme*, 16.
- Sartape, A. S., Mandhare, A. M., Jadhav, V. V., Raut, P. D., Anuse, M. A., & Kolekar, S. S. (2017). Removal of malachite green dye from aqueous solution with adsorption technique using Limonia acidissima (wood apple) shell as low cost adsorbent. *Arabian Journal of Chemistry*, 10, S3229–S3238. <https://doi.org/10.1016/j.arabjc.2013.12.019>
- Schneider, M. H., Andrews, A. B., Mitra-Kirtley, S., & Mullins, O. C. (2007). Asphaltene molecular size by fluorescence correlation spectroscopy. *Energy and Fuels*, 21(5), 2875–2882. <https://doi.org/10.1021/ef700216r>
- Schwager, I., Farmanian, P. A., Kwan, J. T., Weinberg, V. A., Yen, T. F., Farmanian, P. A., & Kwan, J. T. (1983). Characterization of the Microstructure and Macrostructure of Coal-Derived Asphaltenes by Nuclear Magnetic Resonance Spectrometry and X-ray Diffraction. *Journal of Analytical Chemistry*, 55(1), 42–45. <https://doi.org/10.1021/ac00252a014>
- Semple, K. M., Cyr, N., Fedorak, P. M., Westlake, D. W. S., Fedorak A N D Donald W S Westlake, P. M., Fedorak, P. M., & S Westlake, D. W. (1990). Characterization of asphaltenes from Cold Lake heavy oil: variations in chemical structure and composition with molecular size. *Canadian Journal of Chemistry*, 68(7), 1092–1099. <https://doi.org/10.1139/v90-169>
- Setoodeh, N., Darvishi, P., & Lashanizadegan, A. (2017). Enhancing of asphaltene adsorption onto

- Fe₃O₄ nanoparticles coated with metal-organic framework Mil-101 (Cr) for the inhibition of asphaltene precipitation. *Journal of Dispersion Science and Technology*, pp. 1–8. <https://doi.org/10.1080/01932691.2017.1326310>
- Shah, R. S., Shah, R. R., Pawar, R. B., & Gayakar, P. P. (2015). International Journal of Institutional Pharmacy and Life Sciences. *International Journal of Institutional Pharmacy and Life Sciences*, 5(October), 490–505.
- Shayan, N. N., & Mirzayi, B. (2015a). Adsorption and removal of asphaltene using synthesized maghemite and hematite nanoparticles. *Energy and Fuels*, 29(3), 1397–1406. <https://doi.org/10.1021/ef502494d>
- Shayan, N. N., & Mirzayi, B. (2015b). Adsorption and Removal of Asphaltene Using Synthesized Maghemite and Hematite Nanoparticles. *Energy & Fuels*, 29(3), 1397–1406. <https://doi.org/10.1021/ef502494d>
- Shen, Y., Tang, J., Nie, Z., Wang, Y., Ren, Y., & Zuo, L. (2009). Preparation and application of magnetic Fe₃O₄ nanoparticles for wastewater purification. *Separation and Purification Technology*, 68(3), 312–319.
- Sheremata, J. M., Gray, M. R., Dettman, H. D., & McCaffrey, W. C. (2004). Quantitative molecular representation and sequential optimization of Athabasca asphaltenes. *Energy and Fuels*, 18(5), 1377–1384. <https://doi.org/10.1021/ef049936+>
- Sheu, E. Y. (1996). Physics of asphaltene micelles and microemulsions - theory and experiment. *Journal of Physics: Condensed Matter*, 8(25A), A125–A141. <https://doi.org/10.1088/0953-8984/8/25A/009>
- Sheu, E. Y. (2006). Small angle scattering and asphaltenes. *Journal of Physics Condensed Matter*, 18(36). <https://doi.org/10.1088/0953-8984/18/36/S19>
- Shirokoff, J. W., Siddiqui, M. N., & Ali, M. F. (1997). Characterization of the Structure of Saudi Crude Asphaltenes by X-ray Diffraction. *Energy & Fuels*, 11(3), 561–565.

<https://doi.org/10.1021/ef960025c>

Siddiqui, M. N., Ali, M. F., & Shirokoff, J. (2002). Use of X-ray diffraction in assessing the aging pattern of asphalt fractions. *Fuel*, 81(1), 51–58. [https://doi.org/10.1016/S0016-2361\(01\)00116-8](https://doi.org/10.1016/S0016-2361(01)00116-8)

Sides, R., Yarwood, J., & Fox, K. (1988). An FTIR study of the adsorption of surfactants on silica. *Mikrochimica Acta*, 95(1–6), 93–96. <https://doi.org/10.1007/BF01349728>

Simanzhenkov, V., & Idem, R. (2003). *Crude Oil Chemistry*. CRC Press.

Simon, S., Jestin, J., Palermo, T., & Barre, L. (2009). Relation between solution and interfacial properties of asphaltene aggregates. *Energy and Fuels*, 23(1), 306–313. <https://doi.org/10.1021/ef800548b>

Speight, J. G. (1972). The Application of Spectroscopic Techniques to the Structural Analysis of Coal and Petroleum. *Applied Spectroscopy Reviews*, 5(1), 211–263. <https://doi.org/10.1080/05704927208081701>

Speight, J. G. (1994). Chemical and Physical Studies of Petroleum Asphaltenes. *Developments in Petroleum Science*, 40(PA), 7–65. [https://doi.org/10.1016/S0376-7361\(09\)70249-3](https://doi.org/10.1016/S0376-7361(09)70249-3)

Speight, J. G. (2004a). Petroleum Asphaltenes Part 1 Asphaltenes, Resins and the Structure of Petroleum. *Oil & Gas Science and Technology – Rev. IFP*, 59(5), 467–477.

Speight, J. G. (2004b). Petroleum Asphaltenes Part 1 Asphaltenes, Resins and the Structure of Petroleum. *Oil & Gas Science and Technology – Rev. IFP*, 59(5), 467–477. <https://doi.org/10.1080/05704927208081701>

Speight, J. G. (2014). *The Chemistry and Technology of Petroleum* (Fifth edit). CRC Press, Taylor and Francis.

Speight, J. G., Wernick, D. L., Gould, K. A., Overfield, R. E., Rao, B. M. L., & Savage, D. W. (1985). Molecular Weight and Association of Asphaltenes: A Critical Review. *Revue Inst.*

- Franc. Petr.*, 40(1), 51–61. <https://doi.org/10.2516/ogst:1985004>
- Spiecker, P. M., Gawrys, K. L., Trail, C. B., & Kilpatrick, P. K. (2003). Effects of petroleum resins on asphaltene aggregation and water-in-oil emulsion formation. *Colloids and Surfaces A: Physicochemical and Engineering Aspects*, 220(1–3), 9–27. [https://doi.org/10.1016/S0927-7757\(03\)00079-7](https://doi.org/10.1016/S0927-7757(03)00079-7)
- Strausz, O. P., Mojelsky, T. W., & Lown, E. M. (1992). The molecular structure of asphaltene: an unfolding story. *Fuel*, 71(12), 1355–1363. [https://doi.org/10.1016/0016-2361\(92\)90206-4](https://doi.org/10.1016/0016-2361(92)90206-4)
- Strausz, O. P., Mojelsky, T. W., Lown, E. M., Kowalewski, I., & Behar, F. (1999). Structural features of Boscan and Duri asphaltenes. *Energy and Fuels*, 13(2), 228–247. <https://doi.org/10.1021/ef9802451>
- Svalova, A., Parker, N. G., Povey, M. J. W., & Abbott, G. D. (2017). Determination of Asphaltene Critical Nanoaggregate Concentration Region Using Ultrasound Velocity Measurements. *Scientific Reports*, 7(1). <https://doi.org/10.1038/s41598-017-16294-5>
- Tanaka, R., Hunt, J. E., Winans, R. E., Thiagarajan, P., Sato, S., & Takanohashi, T. (2003a). Aggregates Structure Analysis of Petroleum Asphaltenes with Small-Angle Neutron Scattering. *Energy & Fuels*, 17(1), 127–134. <https://doi.org/10.1021/ef020019i>
- Tanaka, R., Hunt, J. E., Winans, R. E., Thiagarajan, P., Sato, S., & Takanohashi, T. (2003b). Aggregates Structure Analysis of Petroleum Asphaltenes with Small-Angle Neutron Scattering. *Energy & Fuels*, 17(1), 127–134. <https://doi.org/10.1021/ef020019i>
- Tanaka, R., Sato, E., Hunt, J. E., Winans, R. E., Sato, S., & Takanohashi, T. (2004). Characterization of asphaltene aggregates using X-ray diffraction and small-angle X-ray scattering. *Energy and Fuels*, 18(4), 1118–1125. <https://doi.org/10.1021/ef034082z>
- Thomas, S., Chan, C. H., Pothen, L. A., Rajisha, K. R., & Maria, H. J. (2014a). 19.3.1 Introduction to FTIR. In *Natural Rubber Materials, Volume 1 - Blends and IPNs* (p. 445). Royal Society of Chemistry.

- Thomas, S., Chan, C. H., Pothen, L. A., Rajisha, K. R., & Maria, H. J. (2014b). 22.3.2 Static Light Scattering or Classic Light Scattering. In *Natural Rubber Materials, Volume 2 - Composites and Nanocomposites*. Royal Society of Chemistry.
- Ullmann, F. (2005). 14.6.1.3 Dynamic Light Scattering. In *Ullmann's Chemical Engineering and Plant Design, Volumes 1-2*. John Wiley & Sons.
- Umar, A., Abaker, M., Faisal, M., Hwang, S. W., Baskoutas, S., & Al-Sayari, S. A. (2011). High-Yield Synthesis of Well-Crystalline α -Fe₂O₃ Nanoparticles: Structural, Optical and Photocatalytic Properties. *Journal of Nanoscience and Nanotechnology*, 11(4), 3474–3480. <https://doi.org/10.1166/jnn.2011.4148>
- Viana, R. B., da Silva, A. B. F., & Pimentel, A. S. (2012). Infrared Spectroscopy of Anionic, Cationic, and Zwitterionic Surfactants. *Advances in Physical Chemistry*, 2012, 1–14. <https://doi.org/10.1155/2012/903272>
- Wang, S., Liu, Q., Tan, X., Xu, C., & Gray, M. R. (2016). Adsorption of asphaltenes on kaolinite as an irreversible process. *Colloids and Surfaces A: Physicochemical and Engineering Aspects*, 504, 280–286. <https://doi.org/10.1016/j.colsurfa.2016.05.086>
- Wilt, B. K., Welch, W. T., & Rankin, J. G. (1998a). Determination of Asphaltenes in Petroleum Crude Oils by Fourier Transform Infrared Spectroscopy. *Energy & Fuels*, 12(5), 1008–1012. <https://doi.org/10.1021/ef980078p>
- Wilt, B. K., Welch, W. T., & Rankin, J. G. (1998b). Determination of Asphaltenes in Petroleum Crude Oils by Fourier Transform Infrared Spectroscopy. *Energy & Fuels*, 12(5), 1008–1012. <https://doi.org/10.1021/ef980078p>
- Xu, F., Yu, J., Tesso, T., Dowell, F., & Wang, D. (2013). Qualitative and quantitative analysis of lignocellulosic biomass using infrared techniques: A mini-review. *Applied Energy*, 104, 801–809. <https://doi.org/10.1016/j.apenergy.2012.12.019>
- Yang, H., Liu, M., & Ouyang, J. (2010). ovel synthesis and characterization of nanosized ??-

- Al₂O₃ from kaolin. *Applied Clay Science*, 47(3–4), 438–443. <https://doi.org/10.1016/j.clay.2009.12.021>
- Yarranton, H. W. (2005). Asphaltene Self-Association. *Journal of Dispersion Science and Technology*, 26(1), 5–8. <https://doi.org/10.1081/DIS-200040234>
- Yarranton, H. W., Hussein, H., & Masliyah, J. H. (2000). Water-in-hydrocarbon emulsions stabilized by asphaltenes at low concentrations. *Journal of Colloid and Interface Science*, 228(1), 52–63. <https://doi.org/10.1006/jcis.2000.6938>
- Yarranton, H. W., & Masliyah, J. H. (1996). Molar mass distribution and solubility modeling of asphaltenes. *AIChE Journal*, 42(12), 3533–3543. <https://doi.org/10.1002/aic.690421222>
- Yarranton, H. W., Ortiz, D. P., Barrera, D. M., Baydak, E. N., Barré, L., Frot, D., ... Oake, J. (2013). On the size distribution of self-associated asphaltenes. *Energy and Fuels*, 27(9), 5083–5106. <https://doi.org/10.1021/ef400729w>
- Yen, T. F. (1974). Structure of petroleum asphaltene and its significance. *Energy Sources*, 1(4), 447–463. <https://doi.org/10.1080/00908317408945937>
- Yen, T. F., & Chilingarian, G. V. (1994). *Asphaltenes and Asphalts 1. Developments in Petroleum Science 40A*. Elsevier.
- Yen, T. F., Erdman, J. G., & Pollack, S. S. (1961). Investigation of the structure of petroleum asphaltenes by X-ray diffraction. *Analytical Chemistry*.
- Young, D. W., & Stacey, M. J. (1978). Petroleum fuel additives: A case for recognition. *Applied Energy*, 4(1), 51–73. [https://doi.org/10.1016/0306-2619\(78\)90019-3](https://doi.org/10.1016/0306-2619(78)90019-3)
- Zhang, J., Zheng, N., & Wang, J. (2016). Two-stage hydrogasification of different rank coals with a focus on relationships between yields of products and coal properties or structures. *Applied Energy*, 173, 438–447. <https://doi.org/10.1016/j.apenergy.2016.04.034>

- Zhao, B., & Shaw, J. M. (2007). Composition and size distribution of coherent nanostructures in Athabasca bitumen and Maya crude oil. *Energy and Fuels*, 21(5), 2795–2804.
<https://doi.org/10.1021/ef070119u>
- Zou, C. (2017). *Unconventional Petroleum Geology*. Elsevier , 2nd ed., 4-5 .

Appendix A: Supplementary Material (Elsevier License)

Rightslink® by Copyright Clearance Center



RightsLink®

Home

Create Account

Help



Title: Asphaltenes Adsorption onto Metal Oxide Nanoparticles: A Critical Evaluation of Measurement Techniques
Author: Nkiru L. Ezeonyeka, Abdolhossein Hemmati-Sarapardeh, Maen M. Husein
Publication: Energy & Fuels
Publisher: American Chemical Society
Date: Feb 1, 2018
Copyright © 2018, American Chemical Society

LOGIN

If you're a **copyright.com** user, you can login to RightsLink using your copyright.com credentials.

Already a **RightsLink** user or want to [learn more?](#)

PERMISSION/LICENSE IS GRANTED FOR YOUR ORDER AT NO CHARGE

This type of permission/license, instead of the standard Terms & Conditions, is sent to you because no fee is being charged for your order. Please note the following:

- Permission is granted for your request in both print and electronic formats, and translations.
- If figures and/or fs were requested, they may be adapted or used in part.
- Please print this page for your records and send a copy of it to your publisher/graduate school.
- Appropriate credit for the requested material should be given as follows: "Reprinted (adapted) with permission from (COMPLETE REFERENCE CITATION). Copyright (YEAR) American Chemical Society." Insert appropriate information in place of the capitalized words.
- One-time permission is granted only for the use specified in your request. No additional uses are granted (such as derivative works or other editions). For any other uses, please submit a new request.

BACK

CLOSE WINDOW

Copyright © 2018 [Copyright Clearance Center, Inc.](#) All Rights Reserved. [Privacy statement](#). [Terms and Conditions](#). Comments? We would like to hear from you. E-mail us at customercare@copyright.com

<https://s100.copyright.com/AppDispatchServlet>

3/12/2018